

*Optimization of a photoelectrochemical water splitting  
cell using bioinspired polydopamine films sensitized  
by II-VI semiconductors*

---

**MASTER THESIS**

FOR OBTAINING THE ACADEMIC DEGREE MASTER OF SCIENCE IN CHEMISTRY  
SUBMITTED TO THE FACULTY 09 – CHEMISTRY, PHARMACEUTICAL SCIENCE, GEOGRAPHY AND  
GEOSCIENCES OF THE JOHANNES GUTENBERG-UNIVERSITY MAINZ

Prepared by

**Matay Kaplan**

born on the 9<sup>th</sup> May 1995 in Wiesbaden

at the

Max-Planck-Institute for Polymer Research  
in the research group of Professor Tanja Weil

Under Instructions of Dr. Christopher Synatschke,  
Tilmann Herberger and Sean Harvey

Mainz, 30<sup>th</sup> November 2020

## **Eigenständigkeitserklärung**

**Masterarbeit im Studiengang Chemie oder Biomedizinische Chemie an der  
Johannes Gutenberg – Universität Mainz**

---

Ich, Matay Kaplan, Matrikelnummer 2714735

versichere, dass ich meine Masterarbeit selbstständig verfasst und keine anderen als die angegebenen schriftlichen und elektronischen Quellen sowie andere Hilfsmittel benutzt habe. Alle Ausführungen, die anderen Schriften wörtlich oder sinngemäß entnommen wurden, habe ich kenntlich gemacht.

Wiesbaden, 30.11.20  
(Ort, Datum)

M. Kaplan  
(Unterschrift)

## Acknowledgements

First, I would like to thank *Prof. Dr. Tanja Weil* for the opportunity to write my thesis in her group at the Max-Planck-Institute for Polymer Research.

My sincere thanks go to *Dr. Christopher Synatschke* as the subgroup leader, *Dr. Sean Harvey* and *Tilmann Herberger*, as my advisors and also to *Tommaso Marchesi* and *Marcel Boecker*, for the valuable support and guidance during my work. Your expertise and our countless discussions during my time in the group, either in the group meeting or in the lab, helped me deepen my knowledge and pursue further with my research. Additionally, the content of this thesis will be part of the PhD thesis of Tilmann Herberger.

I am also thanking all the technicians at the institute, who either trained me for several devices or measured countless samples for me, i.a. *Gunnar Glasser* for SEM measurements, *Katrin Kirchhoff* for TEM measurements, *Leon Prädell* for ITO sputtering and spin coating training, *Uwe Rietzler* for argon plasma training, again *Dr. Sean Harvey* for AFM measurements and *Prof. Dr. Doris Vollmer* and her group for the contact angle and oxygen plasma training.

My thanks go also to our collaboration partners, who are working on the CataLight project. I am thanking especially *Dr. Maria Wächtler* and *Dr. Matthias Micheel* from the Leibniz Institute of Photonic Technology for the synthesis of the core-shell nanorods as a fundamental part of my thesis and for the performed transient absorption spectroscopy measurements.

Special thanks also go to my family and friends. Especially to my parents, *Serpil* and *Serdal Kaplan*, my brother and his wife, *Gabriel* and *Nancy Kaplan*, and of course to our treasure *Jonah Kaplan*, for their encouragement and support that goes beyond this work.

---

## Table of Content

|              |                                                                    |           |
|--------------|--------------------------------------------------------------------|-----------|
| <b>I.</b>    | <b>LIST OF ABBREVIATIONS</b>                                       | <b>1</b>  |
| <b>II.</b>   | <b>ZUSAMMENFASSUNG</b>                                             | <b>2</b>  |
| <b>III.</b>  | <b>ABSTRACT</b>                                                    | <b>3</b>  |
| <b>IV.</b>   | <b>MOTIVATION</b>                                                  | <b>4</b>  |
| <b>V.</b>    | <b>INTRODUCTION</b>                                                | <b>6</b>  |
| V.1.         | Current research in photoelectrochemical water splitting           | 6         |
| V.2.         | Photosynthesis inspired solar system                               | 10        |
| V.3.         | Photoelectrochemistry at semiconductors                            | 13        |
|              | V.3.1. Photocurrent in semiconductors                              | 13        |
|              | V.3.2. Nanocrystals as compound semiconductors (CdSe@CdS)          | 13        |
| V.4.         | Polydopamine                                                       | 16        |
| <b>VI.</b>   | <b>THEORETICAL BASICS</b>                                          | <b>19</b> |
| VI.1.        | Basics of Electrochemistry                                         | 19        |
| VI.2.        | Cyclic Voltammetry                                                 | 22        |
| <b>VII.</b>  | <b>RESULTS AND DISCUSSION</b>                                      | <b>25</b> |
| VII.1.       | Polydopamine film characteristics                                  | 25        |
|              | VII.1.1. Nitrogen vs. regular atmosphere                           | 25        |
|              | VII.1.2. Redox behavior: Controllability of catechol/quinone ratio | 26        |
| VII.2.       | New experimental set up and design                                 | 33        |
| VII.3.       | Photocurrent optimization                                          | 35        |
|              | VII.3.1. Sweeping potential measurement (SPM)                      | 35        |
|              | VII.3.2. Constant potential measurement (CPM)                      | 41        |
| VII.4.       | Ultra-smooth ITO                                                   | 58        |
|              | VII.4.1. General procedure and results                             | 58        |
|              | VII.4.2. Polymerization of PDA                                     | 61        |
| <b>VIII.</b> | <b>CONCLUSION/OUTLOOK</b>                                          | <b>63</b> |
| <b>IX.</b>   | <b>EXPERIMENTAL PART</b>                                           | <b>65</b> |
| IX.1.        | Methods and Materials                                              | 65        |
| IX.2.        | Experimental Implementation                                        | 67        |
| <b>X.</b>    | <b>APPENDIX</b>                                                    | <b>69</b> |
| <b>XI.</b>   | <b>TABLE OF FIGURES</b>                                            | <b>88</b> |
| <b>XII.</b>  | <b>TABLE OF TABLES</b>                                             | <b>95</b> |
| <b>XIII.</b> | <b>REFERENCES</b>                                                  | <b>96</b> |



## I. List of Abbreviations

|                                          |                                                     |
|------------------------------------------|-----------------------------------------------------|
| <b>DA</b>                                | Dopamine, 4-(2-Aminoethyl)benzol-1,2-diol           |
| <b>PDA</b>                               | Polydopamine, Poly(4-(2-Aminoethyl)benzol-1,2-diol) |
| <b>NAD<sup>+</sup></b>                   | Nicotinsäureamid-Adenin-Dinukleotid oxidized        |
| <b>NADH</b>                              | Nicotinsäureamid-Adenin-Dinukleotid reduced         |
| <b>DAQ</b>                               | Dopaminequinone                                     |
| <b>LDAC</b>                              | Leucodopaminechrome                                 |
| <b>DAC</b>                               | Dopaminechrome                                      |
| <b>NMR</b>                               | Nuclear magnetic resonance                          |
| <b>GPC</b>                               | Gel permeation chromatography                       |
| <b>CV</b>                                | Cyclic voltammetry                                  |
| <b>EPR</b>                               | Electron paramagnetic resonance                     |
| <b>XRD</b>                               | X-ray diffraction                                   |
| <b>FT-IR</b>                             | Fourier-transform infrared spectroscopy             |
| <b>DOPA</b>                              | 3,4-Dihydroxyphenylalanin                           |
| <b>HOMO</b>                              | Highest occupied Molecular Orbital                  |
| <b>LUMO</b>                              | Lowest Unoccupied Molecular Orbital                 |
| <b>WE</b>                                | Working electrode                                   |
| <b>CE</b>                                | Counter electrode                                   |
| <b>RE</b>                                | Reference electrode                                 |
| <b>OCP</b>                               | Open circuit potential                              |
| <b>[NBu<sub>4</sub>][PF<sub>6</sub>]</b> | Tetrabutylammoniumhexafluorophosphat                |
| <b>CH<sub>3</sub>CN</b>                  | Acetonitrile                                        |
| <b>Redox</b>                             | Reduction-oxidation                                 |
| <b>RE</b>                                | Regular atmosphere                                  |
| <b>at%</b>                               | Atomic percentage                                   |
| <b>DSSC</b>                              | Dye sensitized solar cell                           |
| <b>PSC</b>                               | Perovskit solar cell                                |
| <b>ALD</b>                               | Atomic layer deposition                             |
| <b>PE</b>                                | Polyelectrolyte                                     |
| <b>NR</b>                                | CdSe@CdS core-shell nanorods                        |

## II. Zusammenfassung

In Zeiten des Klimawandels ziehen umweltfreundliche Technologien zur Erzeugung von sauberer und nachhaltiger Energie mehr Aufmerksamkeit auf sich als je zuvor. Eine der besonders intensiv erforschten Technologien ist die Brennstoffzelle, wodurch elementarer Wasserstoff zu einem wertvollen Ausgangsmaterial wird. Durch den hohen Energiebedarf, der jedoch bei einer elektrochemischen Wasserspaltung anfällt, bleibt die Dampfreformierung aus fossilen Brennstoffen weiterhin die kostengünstigste Methode, um Wasserstoff großtechnisch herzustellen.

Inspiziert von der Photosynthese, um Sonnenlicht in nutzbare Energieformen umzuwandeln, entwickelten die Arbeitskreise von Dr. Maria Wächtler (Leibnitz-Institute für photonische Technologien) und Prof. Dr. Tanja Weil (Max-Planck-Institut für Polymerforschung) unter dem Projekt *Catalight* eine photoelektrochemische Zelle für die photokatalytische Wasserspaltung. Vor diesem Hintergrund konzentriert sich diese Arbeit auf die Optimierung der dafür vorgesehenen Zelle, welche zusammengesetzt ist aus einem redox- und photoaktiven Polydopaminfilm (PDA) in Synergie mit halbleitenden *CdSe@CdS core-shell nanorods* (NR). Die NR, als Photosensibilisatoren, liefern die benötigten Elektronen für die Photolyse von Wasser. Die dabei entstehenden Elektronenlöcher werden von PDA ausgeglichen, wodurch die Lebensdauer der NR erhöht wird.

Anstelle von zeit- und arbeitsaufwendigen quantitativen Wasserstoffmessungen wurde der photoelektrochemisch induzierte Strom (Photostrom) als Maßstab für die Fähigkeit des Systems Elektronen zu erzeugen herangezogen und ermöglicht die Durchführung quantitativer Messungen in kürzester Zeit. Die Effizienz der Zelle wird anhand des Einflusses bestimmter Parameter auf den Photostrom bemessen und dementsprechend angepasst, um die katalytische Effizienz zu optimieren. Diese Arbeit befasst sich daher mit der Entwicklung eines standardisierten Zellaufbaus, um die elektrochemische PDA-Abscheidung mittels Cyclo Voltammetrie (CV) zu optimieren und um mit einer Reihe von Photostrommessungen die Beziehung zwischen PDA und den in PDA eingebetteten NR zu untersuchen. Anhand der bewiesenen Photostabilität-Photostrom Relation kann somit eine optimierte Filmzusammensetzung ermittelt werden. Dabei scheinen die Länge und Konzentration der NR, die Dicke des PDA-Films, das angelegte Potential und der Einfluss eines zusätzlichen Elektronendonors einen entscheidenden Einfluss auf die Art und Größe des Photostroms zu haben. Sowohl anodische als auch kathodische Photoströme konnten kontrolliert erzeugt werden, die wiederum eine Reduktion oder Oxidation an der bestrahlten Oberfläche verursachen können. Zusätzlich wurden die Filme mittels CV charakterisiert, um zum einen den Einfluss von unterschiedlichen pH-Werten auf das intrinsische Catechol/Chinon-Verhältnis in PDA zu untersuchen und zum anderen um eine optimierte Polymerisationsatmosphäre im Hinblick auf die Homogenität und Kontrollierbarkeit des abgeschiedenen PDAs zu ermitteln. Rasterelektronenmikroskopie (SEM) und (hochauflösende) Transmissionselektronenmikroskopie (TEM) sind nützliche Methoden zur Untersuchung von Oberflächen und wurden zur Charakterisierung der NR und ihres Abbauverhaltens herangezogen. Kurzzeit-Spektroskopie (TAS) lieferte zudem wertvolle Informationen über die Dynamik der Elektronenpopulation im Leitungsband der halbleitenden NR.

Abschließend wurde ein neues Verfahren zur Herstellung von ultra-glatten ITO-Oberflächen durch ITO-Kathodenzerstäubung auf präfunktionalisierten Silizium-Wafer entwickelt, um die Charakterisierung der PDA/NR-Filme zusätzlich mit Hilfe von Rasterelektronenmikroskopietechniken wie Rasterkraftmikroskopie (AFM) oder Rastertunnelmikroskopie (STM) zu untersuchen.

### III. Abstract

Nowadays climate change draws more attention than ever, giving rise to an increased focus on generating new materials and innovative technologies to produce clean and sustainable energy on industrial scale. Hydrogen fuel cells are the front runner and one of the most established and researched technology in this field, making molecular hydrogen a valuable material. Although research in electrochemical reduction of water is highly promising for different catalysts on lab-scale, steam reforming from fossil fuels is still the cheapest way to produce hydrogen on large-scale due to the high energy input required for electrochemical reduction.

Inspired by the photosynthesis in plants, for converting and retaining energy from the sun as an endless energy source, the Weil (MPI-P) and Wächtler (Leibniz-IPHT) groups developed a photoelectrochemical cell to transform photons into electrons in order to reduce water and generate hydrogen. Therefore, this work is focused on the optimization of the desired cell. The system is composed of a bioinspired, redox-mediative, photoactive but at the same time photoprotective polydopamine (PDA) film in synergy with well-established semiconducting CdSe@CdS core-shell nanorods (NR). In the envisaged cell, the NR act as photosensitizers and provide electrons for the photolysis of water. PDA acts as a hole scavenger, which is proven by the extended lifetime of the nanorods via photocurrent measurements and transient absorption spectroscopy (TAS). Instead of time and labor-intensive quantitative hydrogen measurements, the initiated photoelectrochemical current (photocurrent) was used successfully as a benchmark for the capability of the system to generate electrons, which in turn could produce hydrogen. This approach provides the opportunity to obtain multiple quantitative results in the shortest time frame. With respect to the cell performance, the influence of decisive parameters on the photocurrent need to be understood and implemented, to optimize and improve the intrinsic catalytic efficiency of the system. This includes the establishment of a standardized cell set-up, the optimization of electrochemically deposited PDA via cyclic voltammetry on semiconducting indium tin oxide electrodes and most importantly a series of photocurrent measurements to investigate the photostability-photocurrent relationship in order to find the most efficient film composition. Investigation of parameters such as the nanorods length and concentration, the PDA film thickness, the applied potential and additional hole scavengers turned out to have to have crucial influence on the nature and magnitude of the photocurrent. Controllable anodic as well as cathodic photocurrents are successfully produced, which in turn cause reduction or oxidation, respectively, on the irradiated surface. Beside photocurrent measurements, the produced films were also characterized via cyclic voltammetry (CV) in order examine the response of the intrinsic catechol/quinone ratio in PDA to different pH or to investigate the influence of different polymerization atmospheres (regular vs. N<sub>2</sub> atmosphere) on the homogeneity and controllability of the deposited PDA. Scanning electron microscopy (SEM), transmission electron microscopy (TEM) and high resolution TEM (HR-TEM) are powerful tools to probe surfaces and were used to characterize the nanorods and their degradation under irradiation. TAS on PDA coated and bare NR revealed valuable information about the electron population dynamics in the conduction band of the semiconductor and proved efficient bleach recovery (hole quenching) by PDA coatings. Finally, in addition, a new method for ultra-smooth ITO surfaces via ITO sputtering on pre-functionalized silicon wafer was developed to enhance characterization of the PDA/NR-films via scanning microscopy techniques, such as atomic force microscopy (AFM) or scanning tunneling microscopy (STM).

## IV. Motivation

For decades scientists have tried to understand natural phenomena, such as photosynthesis, which can lead to interesting discoveries and motivate scientists to develop advanced materials and bring progress into the scientific world. Climate change, as a global issue, gave rise to an increased focus on generating new materials and innovative technologies to produce clean and sustainable energy on industrial scale, based on solar fuel cell technologies and hydrogen as energy source. Nevertheless, climate-neutral production of hydrogen is challenging and the perfect system remains elusive.

Inspired by photosynthesis in plants, the Weil (MPI-P) and Wächtler (Leibniz-IPHT) groups proposed a system that can efficiently generate hydrogen through photocatalytic water splitting. The device envisioned in Figure 1 meets the requirements for a photocatalytic system since it incorporates a catalyst, a photosensitizer and a redox mediating matrix to transmit charges in order to modulate hydrogen production. In the envisaged system n-type semiconducting CdSe@CdS core-shell nanorods (NR) are used as photosensitizers. Despite their high efficiency for hydrogen production, photodegradation of the NR remains a problem due to the residual photogenerated electron holes, which cause degradation.<sup>[1]</sup> Embedding the nanorods in a photoprotective<sup>[2]</sup> and redox-mediative<sup>[3][4]</sup> (hole quenching) polydopamine matrix (PDA) might be the solution to counteract photooxidation of the NR, increase long-term stability and additionally modulate hydrogen production. A broad absorbance in the visible spectrum<sup>[5]</sup>, manageable costs and controllable deposition via cyclic voltammetry<sup>[6]</sup> suggest a promising application in the photolysis of water in combination with a suitable catalyst for proton reduction.<sup>[7]</sup> Based on the band structure of the sensitizing nanorods, photoexcited electrons are delocalized over the whole nanorod (CdSe@CdS), while the holes are energetically favored to move to the core (CdSe). This spatial separation of the electron-hole pair prevents recombination and leaves the electron available for proton reduction.<sup>[1][8]</sup> The destabilized electron hole diffuses after a certain time to the surface of the NR and would lead to degradation under irradiation ( $\text{CdS}_{(s)} + 2 \text{O}_2 \rightarrow \text{Cd}^{2+}_{(aq)} + \text{SO}_4^{2-}_{(aq)}$ ).<sup>[9]</sup> The Catechol moieties in PDA act as hole scavengers (catechol  $\rightarrow$  quinone) and extend the spatial charge separation throughout the whole system, whereby photooxidation of the NR is suppressed. The quinone moieties intercept electrons and recover the photolytic activity by self-regulation (quinone  $\rightarrow$  catechol). The proposed mechanism for self-recovery/hydrogen production (at different pH) in the envisaged device is illustrated in Figure 2. Under the premise of modulating hydrogen production and self-recovery of the system, the response of the intrinsic catechol/quinone ratio in PDA to different pH is decisive and was further investigated in this work. The first part of the thesis deals with the issue regarding to stability and reversibility of the catechol/quinone groups in PDA at different pH or by an applied potential, which induces reduction/oxidation to a favored species.

So far, the alignment of the nanorods has not been achieved. Nevertheless, important aspects of the system can be already investigated with unaligned nanorods embedded in PDA (Figure 1B). First and foremost, the establishment of a standardized set-up is crucial to obtain reproducible and thus comparable results. Hence, the second part of the thesis was to develop a general set-up for polymerization and especially for photocurrent measurements at combined PDA/NR films for a proper internal assessment. The photocurrent is a powerful parameter since it is a measure for released electrons in the system, which in turn can be used to reduce protons at the surface.

The main goal is to extend the lifetime of irradiated NR that are embedded in PDA while producing high photocurrents. Long-term stability and photocurrent studies hence require the development of an experimental method, which provides meaningful parameters to quantify the longevity of the system regarding the photocurrent. Hence, the PDA/NR ratio is a critical parameter and is optimized, e.g. through optimizing NR concentration and PDA film thickness, with regards to their optoelectronic properties. Additionally, the photocurrent and NR stability should benefit from electron donors, such as PDA (catechol moieties) in acidic environment. The effectivity of PDA as a hole scavenger can be examined in relation to the effect of additional hole scavengers on the photocurrent and by transient absorption spectroscopy (bleach recovery) performed by the Wächtler group and is an essential issue discussed hereinafter.

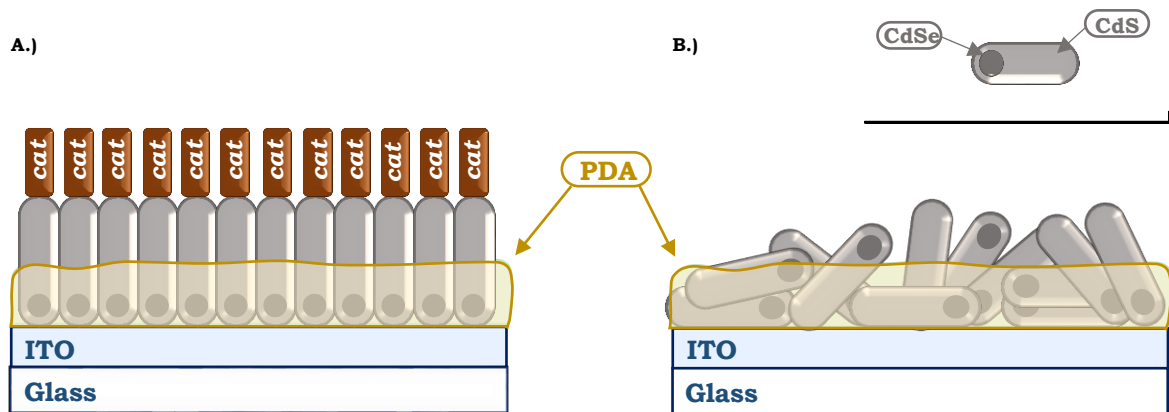


**Figure 1.** Schematic representation of **A.)** the desired system for hydrogen production, consisting of CdSe@CdS core-shell nanorod aligned perpendicular to an indium tin oxide (ITO) electrode supported by a thick glass layer. The nanorods are coated partially in polydopamine (PDA) and a catalyst is attached at the exposed tip. **B.)** In the current system the spin coated nanorods are distributed randomly and are therefore differently coated with PDA.

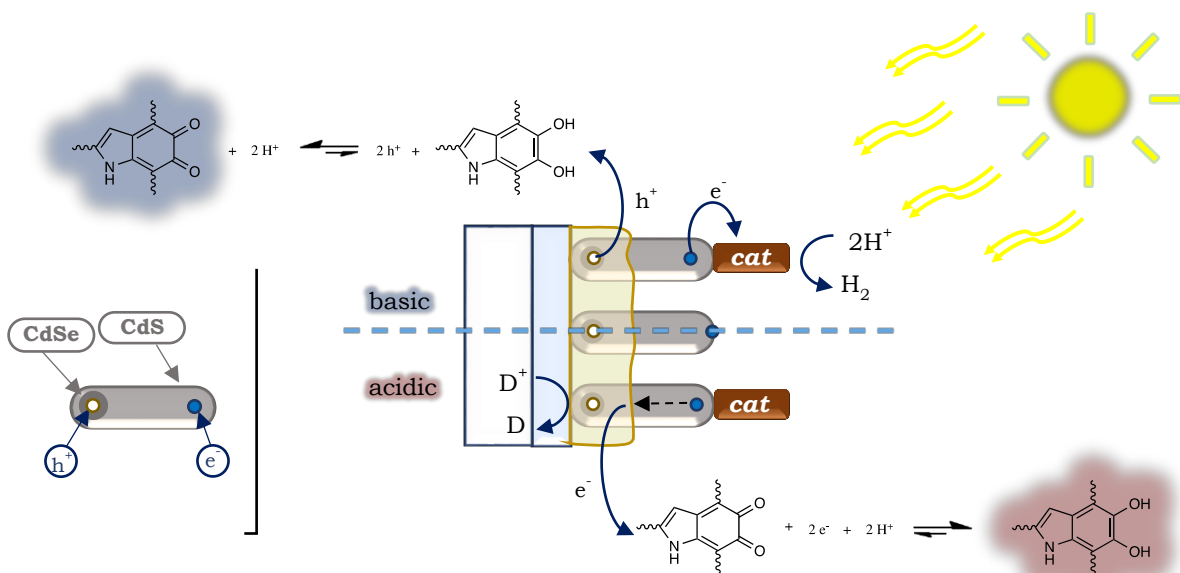


**Figure 2.** Schematical representation of the proposed mechanism for hydrogen production in the envisaged device. Spatially separated excitons, induced by light irradiation in the CdSe@CdS core-shell nanorods, can be used for proton reduction. H<sub>2</sub> production can be modulated by the supporting PDA film via pH regulations in order to quench electron holes and favor H<sub>2</sub> production (basic environment) or to self-recover and turn of H<sub>2</sub> production (acidic environment).

## V. Introduction

### V.1. Current research in photoelectrochemical water splitting

There are several approaches to produce hydrogen either from non-renewable or renewable sources (see Figure 3). Non-renewable carbon-based fuels such as coal, natural gas or oil make up to 94 % of the worldwide hydrogen production, whereas only 4 % are made from electrochemical water splitting. Electrolysis of water can be performed conventionally by alkaline water electrolysis (AWE) or by proton exchange membranes (PEM) in acidic environment. Due to the high energy input in conventional electrolysis, current research is focusing more on implementing photoelectrochemical (sun light energy) or thermoelectric (sun heat energy) devices into the electrolysis process or to couple solar cells, such as dye sensitized solar cells (DSSC) or perovskite based solar cells (PSC), to provide the required current for electrochemical water splitting.<sup>[10][11]</sup>

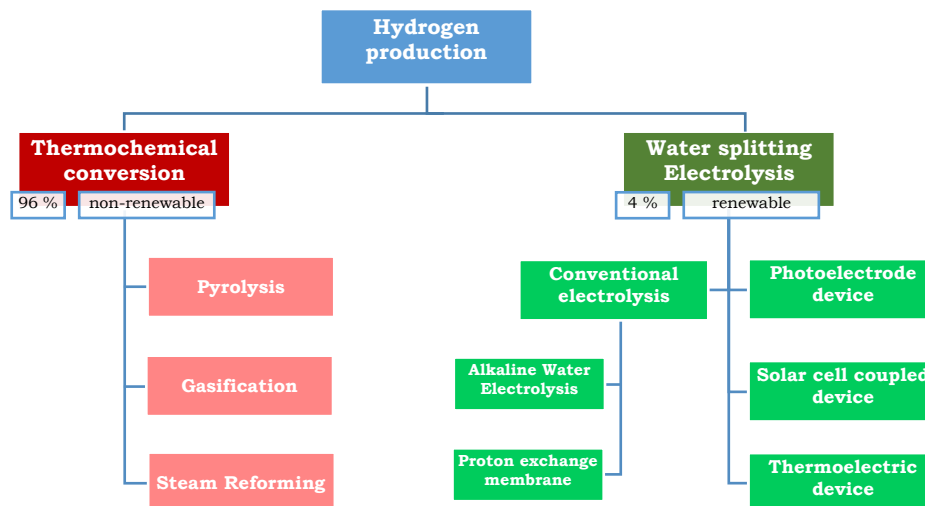


**Figure 3.** Overview of the most common hydrogen production methods by either thermochemical conversion from non-renewable fuels (94 % of worldwide H<sub>2</sub> production) or by the electrolysis of water (4 % of worldwide H<sub>2</sub> production).

In the early 1970s scientists already started working on the electrochemical photolysis of water on semiconductors<sup>[12]</sup> because hydrogen-based fuel systems are considered to be extremely effective and clean energy sources. This is based on the high chemical bonding energy of hydrogen and water as the ‘exhaust’ end product, which in turn is the raw material for hydrogen production via water splitting.<sup>[13]</sup> The environmentally friendly technology of fuel cell engines was already established in 1966 by General Motors<sup>[14]</sup> and has been further improved since then. Nevertheless, for cost reasons, the industrial hydrogen production is still done using fossil fuels during Steam Reforming ( $\text{CH}_4 + \text{H}_2\text{O} \rightarrow \text{CO} + \text{H}_2\text{O} \rightarrow \text{CO}_2 + \text{H}_2$ ), which in turn produces excessive amounts of carbon dioxide.

Already during one hour, solar energy in the magnitude of a worldwide annual energy consumption (~ 20 TW) is reaching our planet. Hence, incorporating solar energy into a large-scale hydrogen production based on water splitting would revolutionize modern life by providing an environmentally friendly and abundant energy source. In addition to fuel cell technologies, the whole chemical economy would benefit from such an outcome because massive productions of, for example, ammonia and methanol are also dependent on hydrogen.<sup>[7]</sup>

Regarding to the required energy amount for water splitting, it is reasonable to assist the electrolysis with an external energy providing system such as solar cells DSSC, which are based on  $\text{TiO}_2$ . Although  $\text{TiO}_2$  is well established in this research field and represents a benchmark as photoelectrode, the broad band gap of 3.2 eV limits the solar photocatalytic application since only ultra violet light can overcome this energy barrier.<sup>[15]</sup> Multiple functionalization, such as noble metal loadings or additional photosensitizer (DSSC) are necessary to enhance the performance but high costs (noble metal loading<sup>[16]</sup>, noble metal dyes<sup>[17]</sup>) and/or long-term instabilities (electrolyte bleaching<sup>[18]</sup>, natural dye bleaching<sup>[19]</sup>) cannot be avoided in the system. Over the past years perovskite based solar cell were intensively studied due to their high efficiencies, which will be shown hereinafter.<sup>[11]</sup>

Nevertheless, it is difficult to find a material, which utilized the solar spectrum, exhibits efficient charge separation and transfer (electron/hole) in addition to a predominating driving force for water splitting.<sup>[11][20]</sup> Therefore, different materials need to be combined in order to meet all the requirements. This led to the development of many different photoelectrochemical cells in order to push the solar-to-hydrogen efficiency > 10 % and long-term stability > 10 years.<sup>[21]</sup> There are innovative developments for photoelectrochemical anodes as well as cathodes which will be addressed in the following.<sup>[22][11]</sup>

Among the many approaches over the past years, tandem structures were intensively studied. Thereby, photovoltage is generated by light absorption of different semiconducting electrodes addressing distinct wavelength of the solar spectrum. *Gurudayal et al.*<sup>[23]</sup> took advantage of the high theoretical solar-to-hydrogen conversion of hematite  $\text{Fe}_2\text{O}_3$ . In contrast to the  $\text{CdSe@CdS}$  core-shell nanorods, fast charge recombination (electron/hole), unsuitable band gap position and poor kinetics for overall water splitting limits the performance of a hematite electrode and needs further preparation. A Mn-doped hematite photoanode stacked with only a single perovskite solar cell ( $\text{TiO}_2/\text{CH}_3\text{NH}_3\text{PbI}_3$ ) increased the performance and led to a solar-to-hydrogen efficiency of 2.4 %. The tandem cell is illustrated in Figure 4 and generates a voltage of 1.87 V and exceeds the kinetically hindered water splitting potential (1.6 V). This system is representing one of the most efficient structures with the incorporation of only one perovskite solar cell in series.

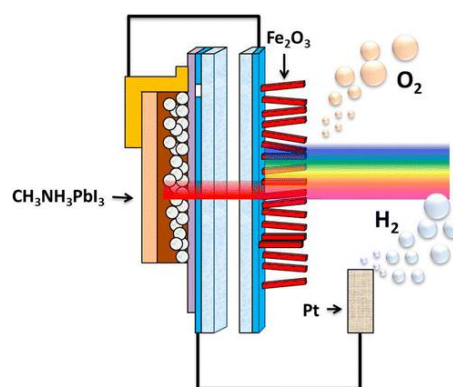


**Figure 4.** Schematic representation of nanostructured hematite based tandem design of a photoelectrochemical water splitting cell coupled to a perovskite solar cell (PSC).<sup>[23]</sup>

Other approaches are based on more complex tandem structures, such as the water splitting cell developed by *Kim et al.*<sup>[21]</sup> The device is based on a dual-doped  $\text{BiVO}_4$  complex. The suitable band gap energy and position (2.5 eV vs. RHE), good electron hole conductivity and a high theoretical solar-to-hydrogen efficiency of 9.2 % makes it a promising candidate for water splitting devices. For semiconducting CdS it is just the incorporation of a CdSe core, which increase charge carrier separation and extend the absorption range, while for  $\text{BiVO}_4$  multiple labour-intensive modifications are necessary.



Intensive optimization studies were performed in order to increase charge carrier separation and absorption range. Dual doping with (external,  $\text{Mo}_V^*$ ) 3 at% Mo and (internal,  $\text{V}_O^{**}$ ) hydrogen treatment at 300 °C led to the development of the most efficient metal oxide based photoanode. In series with a second absorber (perovskite solar cell,  $\text{TiO}_2/\text{CH}_3\text{NH}_3\text{PbI}_3$ ) the tandem structure achieves a solar-to-hydrogen efficiency of 3 % (see Figure 5).

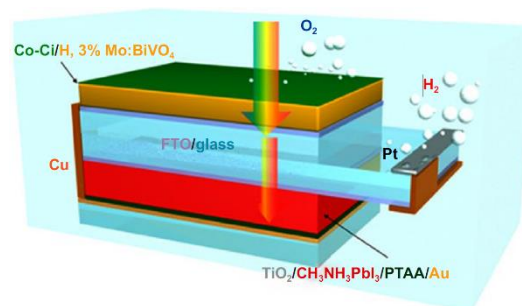


**Figure 5.** Schematic representation of a dual doped  $\text{BiVO}_4$  based tandem structure of a photoelectrochemical water splitting cell coupled to a perovskite solar cell.<sup>[21]</sup>

*Jin et al.*<sup>[24]</sup> reported of  $\text{Cu}_2\text{O}$  as a photocathodic film for water splitting.  $\text{Cu}_2\text{O}$  is a highly promising material since band gap energy (2.0 eV) and position are matching the water splitting potentials in addition to one of the highest theoretical hydrogen-to-solar efficiencies of 18 %. Similar to the  $\text{CdSe@CdS}$  core-shell nanorods used in this work,  $\text{Cu}_2\text{O}$  undergoes severe photodegradation (photoreduction to Cu). After merely 10 minutes only 7.5 % of the initial current is detected. This can be prevented by thin layers of photoprotective aluminum doped zinc oxide (AZO) (20 nm) and  $\text{TiO}_2$  (100 nm) via atomic layer deposition (ALD). The AZO/ $\text{TiO}_2$  layers promote charge carrier separation (electron/hole) and increase the photostability of the system. *Pan et al.*<sup>[25]</sup> reported that nanostructured  $\text{Cu}_2\text{O}$  and deposition of a  $\text{Ga}_2\text{O}_3$  and  $\text{TiO}_2$  layer improve solar-to-hydrogen efficiency to 3 % in series with a Mo-doped  $\text{BiVO}_4$  photoanode (see Figure 6). Additionally, the long-term stability increased to 100 h.

Compared to photovoltaic coupled electrolysis (Figure 4 and Figure 5), the main advantage of such non-coupled photoelectrochemical cells is that light absorption and electrochemical reactions are combined in one device, which decreases costs and complexity because no external energy consumption is necessary. Nevertheless, solar-to-hydrogen efficiencies are generally higher with a solar cell coupling<sup>[20]</sup> but the corresponding long-term stability problems cannot be avoided for DSSC<sup>[16][17][18][19]</sup> as well as for PSC<sup>[26]</sup>.

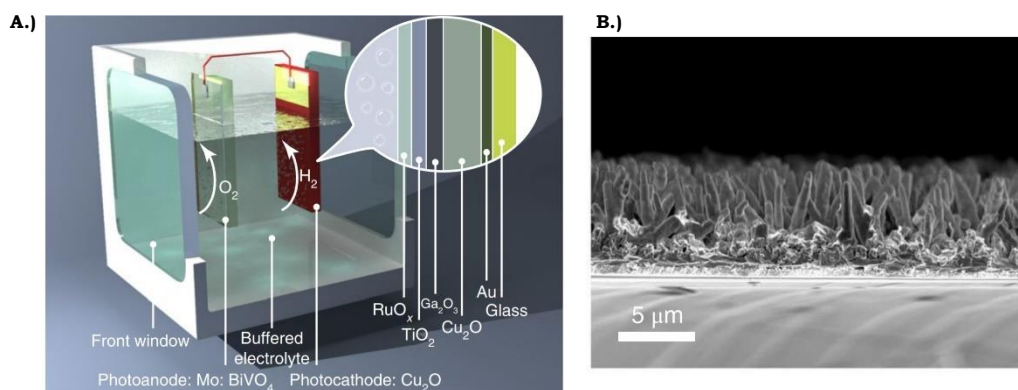


**Figure 6. A.)** Schematic representation of nanostructured  $\text{Cu}_2\text{O}$  based tandem design of a photoelectrochemical water splitting cell. **B.)** Nanostructure of uncoated  $\text{Cu}_2\text{O}$  resolved by scanning electron microscopy (cross section).



General trends are visible based on the presented water splitting cells, which are in direct relation to the envisaged cell in Figure 1. For example, additional labor-intensive preparation, as for TiO<sub>2</sub> or dual-doped BiVO<sub>4</sub>, is not necessary for CdS because it has already a suitable band gap energy (2.3 eV) and position for overall water splitting.<sup>[7]</sup> Additionally, semiconducting electrodes, such as hematite and Cu<sub>2</sub>O electrodes, are clearly improved by a nanostructured the surface, which confirms the superiority of CdS-nanorods over the bulk material regarding catalytic efficiency.

Anyway, thick coatings (> 100 nm layers) via cost- and labor-intense ALD are necessary to prevent photodegradation and increase charge carrier separation in nanostructured Cu<sub>2</sub>O. For CdS-nanorods the simple implementation of a CdSe core during the synthesis entails the same effect.<sup>[27]</sup> Additional electrochemical deposition of thin PDA films (< 20 nm) within several minutes entails different advantages, which are not given by any of the presented cells. The modulation between hole quenching (promoting nanorods stability and hydrogen production) and self-recovery by pH regulations as well as the possibility to post-functionalize the surface, based on simple chemistry, are unique properties of the intrinsic catechol/quinone moieties in PDA.

Furthermore, PDA acts as a complex charge carrier matrix, which is crucial for photocatalytic systems mimicking photosynthesis. *Sai and Stubb et al.*<sup>[28][29]</sup> developed a different approach for hydrogen production on a similar premise. Inspired by the photosynthetic organelles in plants, they designed hydrogels as complex charge carrier matrices. Their system is based on soft materials inspired by the structure of chloroplast in plants, where stacked structures promote light absorption, transport charge carriers and enable catalytic reactions needed for photosynthesis. They developed hydrogels which are based on self-assembled carboxylate-functionalized perylene monoimide chromophore amphiphile (PMI-CA) in 2D-crystalline lattice as light absorber (Figure 7A). The incorporation of crosslinked polyelectrolytes (PE) can irreversibly cause robust gel formation into a 3D network (Figure 7B), which hosts the soluble components for hydrogen production. Attachment of a Na<sub>2</sub>[Mo<sub>3</sub>S<sub>13</sub>] catalyst yielded sufficient hydrogen production under irradiation with ascorbic acid as sacrificial electron donor and proved the concept.

Compared to the previously presented inorganic catalytic systems, the supramolecular approach in organic systems enables multiple features. For example, energy levels and modes of self-assembly can be controlled by the molecular structure of the compounds, in order to design nanostructures with high aspect ratio to induce anisotropic charge transportation.

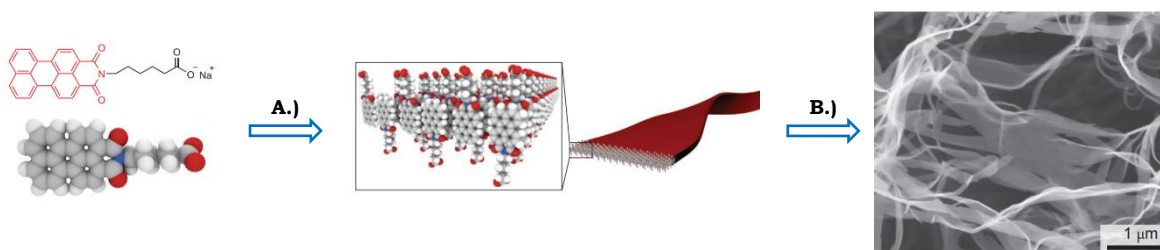


**Figure 7. A.)** Self-assembly of carboxy-functionalized perylene monoimide chromophore amphiphile into ribbon-like structures. **B.)** Scanning electron microscopy image of the hydro gel formed after the incorporation of poly(diallyldimethylammonium) chloride as polyelectrolyte.

## V.2. Photosynthesis inspired solar system

Photoelectrochemical solar fuel cells, for converting light energy into chemical energy, are highly promising as sustainable and high efficient energy sources<sup>[13]</sup> and are inspired by nature's photosynthesis, where complex light harvesting and transforming networks in the photosystem II (PS II) gain electrons from the sun light. The basic principle of such a complex photosystems, can be simplified to three major components and is shown for PS II in Figure 8A. Chlorophyll, as one of nature's photosensitizers, provides electrons from the sun light. The electrons are transferred to plastoquinon, which in turn transports the electrons as plastoquinol (nature's catechol/quinone redox mediator) further through multiple protein networks into the photosystem I and mediates the reduction of  $\text{NADH}^+$ . Hence, the three major components of such a complex system are a photosensitizer, a redox mediator and an efficient electron transportation system to transmit the electrons to the catalyst for the catalytic process of interest (Figure 8B).

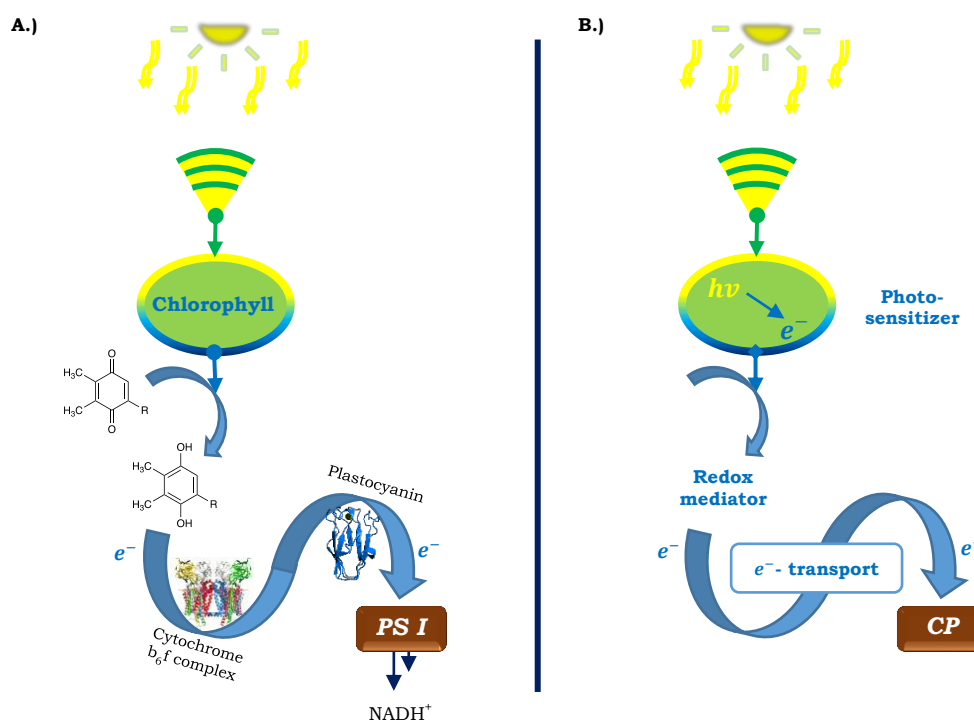


**Figure 8. A.)** Simplified representation of photosystem II (PS II) in photosynthesis. Chlorophyll as a photosensitizer provides electrons to plastoquinon. The reduced plastoquinol transports the electrons through cytochrome b<sub>6</sub>f and plastocyanin into the photosystem I, where  $\text{NADH}^+$  is reduced. **B.)** General compounds for a PS II inspired photocatalytic cell. Electrons are generated by a photosensitizer, transported to a redox mediator and transmitted through a complex electron transportation network to the catalyst.

Encouraged by the mechanism of PS II, the Weil (MPI-P) and Wächtler (Leibniz-IPHT) groups designed a photoelectrochemical system to produce hydrogen by water splitting. Photons are thereby harvested and transformed into a charge separated electron-hole confinement in n-type semiconducting CdSe@CdS core-shell nanorods (photosensitizer). Based on the band structure of the nanorods, the electron is delocalized over the hole nanorod (CdSe@CdS), while the hole is energetically favored to move to the core (CdSe).

This causes a spatial separation of the electron/hole pair and suppresses recombination, leaving the electron available for proton reduction.<sup>[1][8]</sup>

This type of photosensitizer is extremely active and was shown by *Kalisman et al.*<sup>[1]</sup> to have, in combination with platinum as catalyst, a 100 % photon-to-hydrogen production efficiency. Wet adhesion of proteins in mussels, motivated the investigation of polydopamine (PDA) as the second major component in the desired device.<sup>[30]</sup> Due to the reported versatile properties (broad absorbance in the visible spectrum<sup>[5]</sup>, photoprotectivity<sup>[2]</sup>, biocompatibility, redox mediation<sup>[3][4]</sup>, low costs and controllable deposition via cyclic voltammetry<sup>[6]</sup>), PDA suggests a promising application as a redox mediator and a charge transportation network in photocatalytic systems (Figure 9).

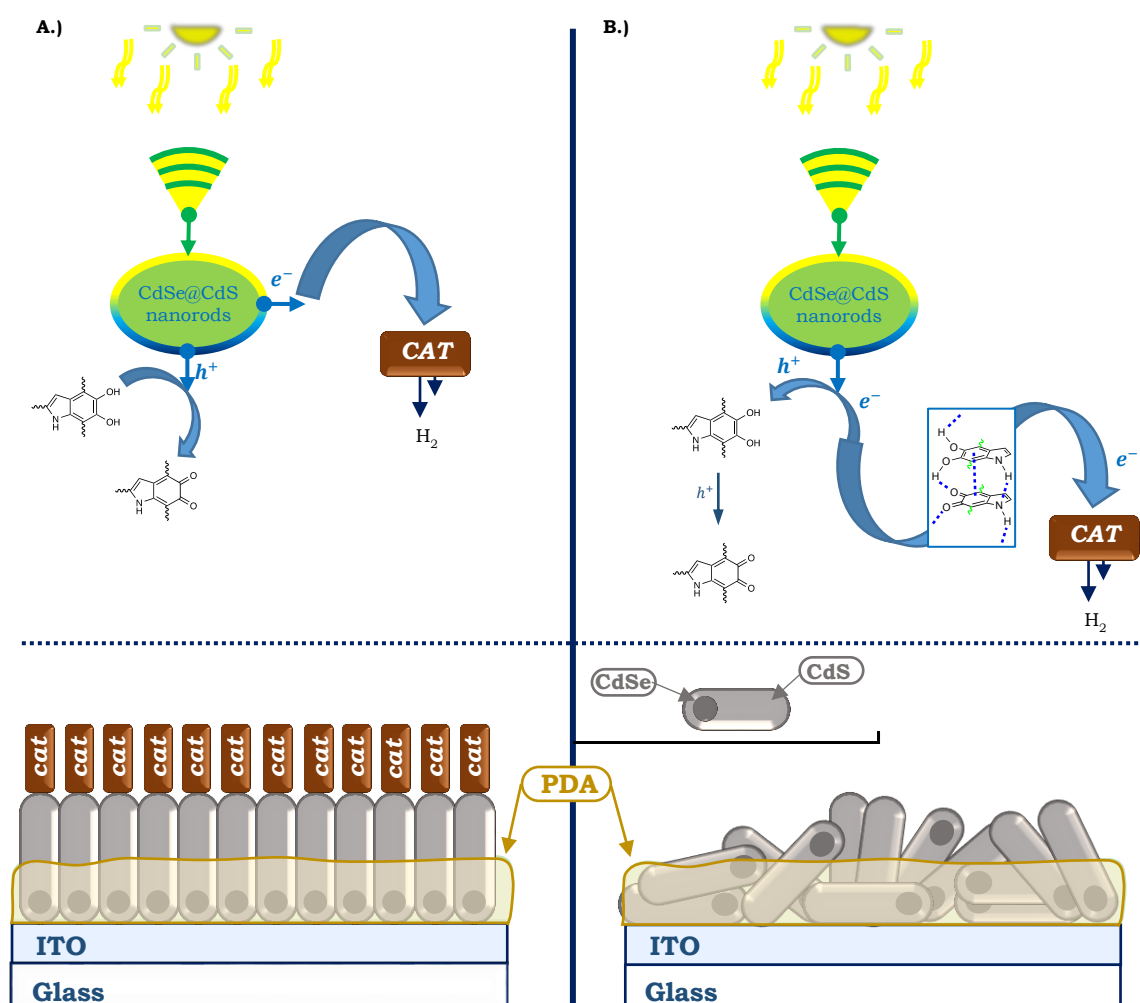


**Figure 9. A.)** Simplified model of the envisaged photoelectrochemical cell. CdSe@CdS core-shell nanorods as photosensitizers provide electrons, which are transported to the tip of the NR and reduce hydrogen. **B.)** Simplified model of current device. Polydopamine (PDA) coated nanorods provide electrons, which travel through PDA to an attached catalyst for hydrogen production. Electron holes in the nanorods are quenched in both devices by redox mediative PDA.

In the envisaged cell PDA is used as an adhesive matrix, to fix the nanorods in their perpendicular position, as well as a hole scavenger in order to quench a generated electron hole in the nanorods, while the corresponding electron can be used for catalytic processes such as hydrogen evolution (Figure 9A).

PDA is acting as a hole scavenger (oxidation: catechol  $\rightarrow$  quinone) in basic environment and self-recovers (reduction: quinone  $\rightarrow$  catechol) in acidic environment, whereby hydrogen production can be modulated. In the current device the semiconducting nanorods are covered partially in PDA (depending on the nanorod concentration and controllable thickness of the PDA layer). By taking additional advantage of the broad absorbance range and the photoprotective behavior of PDA, photodegradation of the nanorods<sup>[1]</sup> can be prevented further, which is crucial for the long-term stability and is an additional feature in the current device (Figure 9B). Both, the envisaged as well as the current system suggest a promising application in solar fuel cells when combined with a suitable catalyst for hydrogen production.

The generated photocurrent is generally a benchmark of the system to produce light induced electrons, which in turn can be used for proton reduction. Water splitting or more precisely proton reduction, is therefore electrochemically noticeable by the detection of negative currents (at negative potentials) and is enhanced/favored by a sufficient catalyst. The hydrogen evolution activity of a catalyst is assessable electrochemically in a shift of the reduction potential for hydrogen. A high negative current at small applied potentials indicates good catalytic activity.<sup>[31]</sup>

Hence, photocurrent measurements and optimization efforts in this work were carried out particularly regarding the generation of high photocurrents while maintain a long-term stability of the system.

### V.3. Photoelectrochemistry at semiconductors

#### V.3.1. Photocurrent in semiconductors

Photoelectrochemistry describes a two-step process, where light energy is converted into electrical/chemical energy. Therefore, an electrode (or a deposited material on the electrode) is first irradiated and produces subsequently a current (photocurrent), which is dependent on the electrode/deposited material, wavelength of the light and the electrolyte solution.<sup>[32]</sup>

Generally, the conductivity of semiconductors is modelled by the band model. Due to the closely packed atoms in solids, the discrete single molecular orbitals of the single atoms overlap. Taking the Pauli exclusion principle into consideration, the electrons in those overlapping orbitals cannot coexist with the same quantum number. Hence, the orbitals degenerate energetically and form a continuous energy band (see Figure 10). The filled (binding) orbitals are forming the valence band and the corresponding vacant (antibonding) orbitals are forming the conduction band. The two energy bands are separated by the band gap energy  $E_g$  and the highest occupied energy level (at 0 K) is called the fermi energy  $E_F$ . If the fermi energy falls into a band, the material is a conductor (metal, half-metal). For insulators and semiconductors, the fermi energy falls within the band gap. The band gap in intrinsic semiconductors is very small and electrons can overcome the band gap by thermal energy ( $E_g \ll kT$ ), which leads to a good conductivity ( $\hat{=}$  good electron mobility). Extrinsic semiconductors are doped with additional electron donors (n-type, electron doping) or electron acceptors (p-type, hole doping) in order to increase the charge carrier mobility in the bands.<sup>[33]</sup>

The small band gap in semiconductors can also be overcome by the absorption of photons, thus creating electron-hole pairs. Different conditions (e.g. an applied potential) might counteract a recombination of these pairs. For n-type semiconductors, the holes move to the surface and lead to an oxidation, while the electrons move into bulk material and hence into the circuit (due to an electrostatic force caused by band bending of the semiconductor at the surface). This leads to a photoanodic current (photo-oxidation, positive current). Analogous, a photocathodic current (photo-reduction) is obtained for p-type semiconductors. The holes are moving to the bulk material and into the circuit (negative current), while the electrons move to the surface leading a reduction.<sup>[32]</sup>

#### V.3.2. Nanocrystals as compound semiconductors (CdSe@CdS)

Compound semiconductors are composed of at least two different elements and are classified by their main group number in the periodic table, e.g. II-VI, II-V and IV-IV type semiconductors. Even by neglecting ternary or even higher order of compounds, there are many different possibilities of binary alloys. Varying the stoichiometry or adding dopants can even extend the possibilities. Therefore, it is important to have an idea of the desired optoelectronic behavior in order to combine the ideal compounds for a specific application. Regarding to their properties, II-VI semiconductors are mostly used in solar cells, photoelectrochemical energy conversion and storage.<sup>[34]</sup>

Semiconductors can also occur as nanocrystals, like nano-dots or nanorods, which opened a new field of research because they show different properties than the bulk material. Due to the quantum size effect, the band gap between the valence and conduction band can be adjusted by the size of the nanocrystal because the wave function of the electron is spatially limited to the nanoparticle size and needs to adjust to that restriction ( $\rightarrow$  particle in the box model).

In regular semiconductors (macrocrystals) the electrons and holes are widely delocalized, resulting in a high kinetic energy in the corresponding bands. In nanocrystals however there are not so many orbitals involved that overlap. Therefore, the energetic splitting/degeneration is not as strong as in regular semiconductors, which leads to a larger band gap (see Figure 10). Hence smaller nanocrystals lead to larger band gaps.<sup>[35][36][37]</sup>

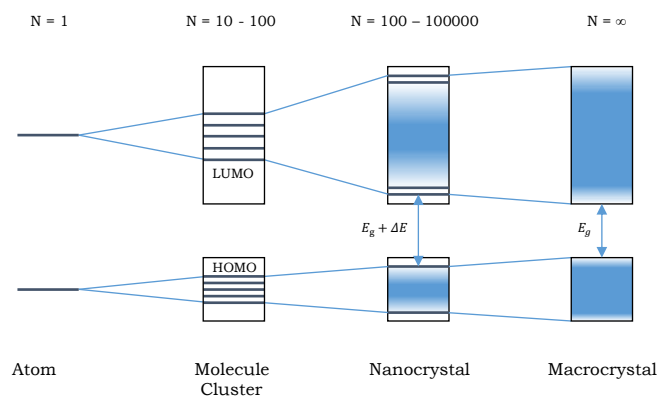


**Figure 10.** Schematical representation of orbital/band energy levels for different types of materials. The band gap  $E_g$  decreases with an increasing number of atoms  $N$ .

Especially core-shell structures of nanocrystal semiconductors have drawn attention and have been studied intensively. The design of such semiconductors is tailored according to their band structure. The valence band edge as well as the conduction band edge of the core should lie in the band gap of the shell. Consequently a created exciton is highly affine to the core and a recombination is highly probable, which leads to a high photoluminescence quantum yield (but a slight shift of the band gaps can lead to significantly different electron-hole confinements, see Figure 11 for CdSe@CdS nanorods).<sup>[38]</sup> These new structures come along with new properties in terms of color tunable emission, localized charge carriers, charge carrier separation and an increased photocatalytic reduction/oxidation efficiency. Therefore, they might be useful tools in applications for light harvesting, solar cells, photocatalysis and solar hydrogen production.<sup>[39][27]</sup>

A well-established example of these new structures is a semiconducting cadmium sulfide (CdS) shell grown onto a semiconducting cadmium selenide (CdSe) core (short CdSe@CdS). The CdSe core entails two main advantages. First, it extends the (visible) absorption spectrum<sup>[40]</sup>, which causes the photoluminescence quantum efficiency to be two orders of magnitude higher than regular CdS nanorods.<sup>[41]</sup> As a comparison, CdS nano-dots ( $r \sim 5$  nm) show an absorbance onset at 488 nm (2.54 eV band gap), whereas for CdSe nano-dots it is increased up to 670 nm (1.85 eV) ( $r \sim 5$  nm).<sup>[42]</sup> Due to the suitable band gap energies it is also a promising material in order to convert solar energy into chemical energy, for instance solar hydrogen production (see Figure 11). A catalyst is useable for hydrogen production, when the conduction band edge is at a more negative potential than the proton reduction (0 V vs. NHE) and the valence band edge in turn is at more positive potentials than the oxidation potential (1.23 V vs. NHE). This is the case for CdSe@CdS core-shell nanorods. In total an energy of 1.23 eV is needed and would be provided from a photon with a wavelength of  $\sim 1010$  nm (covered up to 70 % by the solar spectrum).<sup>[7]</sup>

Secondly, the CdSe core decreases the rate of photodegradation (oxidation) due to an improved spatial separation of an electron (in shell) and the corresponding hole (in core), which is based on a quasi-type II electron-hole confinement.<sup>[27]</sup>

This means a small conduction band offset  $\Delta E_2$ , leads to the delocalization of the electron between both, CdS and CdSe. The electron hole on the other hand is located in the CdSe core, due to a large valence band offset  $\Delta E_1$  between CdS and CdSe (see Figure 11).<sup>[43]</sup> Therefore, an enhanced electron transfer mechanism is observed for CdSe@CdS nanorods.<sup>[27]</sup> The spatial separation of electron-hole and also the photostability of CdSe@CdS can be even enhanced by increasing the length of the nanorods.<sup>[44][45]</sup>

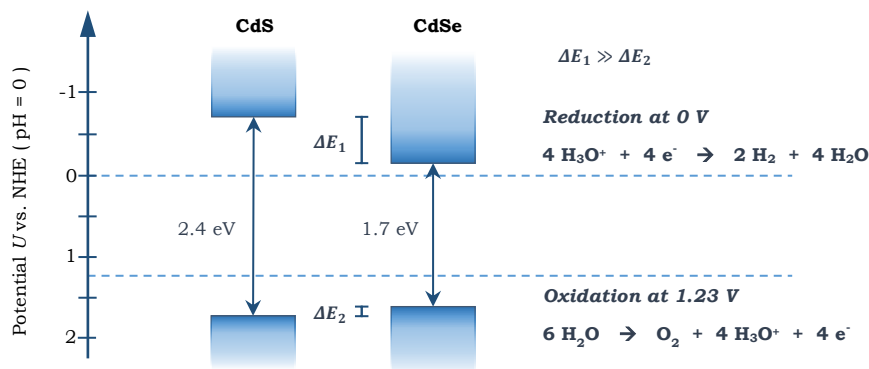


**Figure 11.** Band gap scheme of CdS and CdSe referring to the water splitting potentials against a normal hydrogen electrode (NHE). A quasi type-II electron-hole confinement is present due to different valence band and conduction band offset energies,  $\Delta E_1 \gg \Delta E_2$ .

#### V.4. Polydopamine

The synthesis and characteristics of proteins and peptides in mussels, which have shown to attach at almost every surface, were investigated in their chemical composition already over forty years ago. It was found early, that especially amino acids with catechol moieties like 3,4-dihydroxy-L-phenylalanine (L-DOPA) and lysine-enriched proteins are the major cause of the exceptionally adhesion.<sup>[46][47][30]</sup>

Almost twenty five years later in 2007, inspired by its strong covalent and non-covalent interactions, polydopamine (PDA) was firstly hypothesized by *Messersmith et al.*<sup>[48][6]</sup> to show a similar adhesive behavior (like L-DOPA<sup>[47]</sup>) and a similar polymerization pathway to melanins (like 1,2-catechol derivatives<sup>[3]</sup>). Nowadays it is known that high amounts of catechol groups in combination with high amine content (primary or secondary) are the key features of the adhesive properties observed for different kinds of proteins and polydopamine.<sup>[47][49]</sup> Moreover, due to its manageable cost, controllable deposition, biocompatibility and versatile application range, polydopamine became widespread in the scientific world.<sup>[6][50]</sup> The remarkable adhesion of PDA was one of the diverse properties taken into consideration for the designed photoelectrochemical cells in Figure 9 since PDA can embed the CdSe@CdS nanorods on the electrode surface and fix their (aligned) position.

Charge separation (electron/hole separation) in the excited state of the nanorods is crucial for producing hydrogen. Inspired by the PS II of photosynthesis, redox mediators containing catechol/quinone moieties (such as PDA) can consume charges and eventually transport them through a complex transportation network to mediate between  $\text{NAD}^+/\text{NADH}$ .

In 1998 *Davis et al.*<sup>[3]</sup> investigated first polymeric structures containing catechol/quinone moieties based on 1,2-dihydroxybenzene, 3,4-dihydroxy benzoic acid and 3,4-dihydroxycinnamic acid in their redox behavior during electropolymerization and their ability to mediate between  $\text{NAD}^+/\text{NADH}$ . It was noticed, that the oxidation/reduction peaks were decreasing with the number of cyclic voltametric (CV) cycles and indicated an irreversible chemical turnover in neutral to alkaline pH, which led to an electrochemical deposition of a thin polymeric film on the electrode. The addition of ethylene diamine to the monomer solution even reinforced that deposition. The electrochemically produced films have also shown to be able to mediate the natural redox system  $\text{NAD}^+/\text{NADH}$  electrochemically.<sup>[3]</sup> Knowing that a material can act as a catalyst for  $\text{NAD}^+/\text{NADH}$  is very useful because there are hundreds of enzymes, which require such cofactors. Those materials may have the capability to be applicable as biosensors.

Dopamine possesses the same functional groups (catechol/quinone and amino groups) as the monomers used by *Davis et al.* and shows the same electrochemical deposition of an insulating thin polymeric film on electrodes (PDA). Therefore PDA is also a promising candidate to mediate between  $\text{NAD}^+/\text{NADH}$  and inspired the application of it as part of the biosensing research field.<sup>[51][52]</sup> This supports the hypothesis of PDA acting as a hole scavenger and redox mediator according to the mechanism proposed in Figure 2 in basic environment. Despite hole quenching, PDA should also be able to act an electron acceptor under acidic conditions, as it is proposed for the desired photoelectrochemical cell.

This behavior was proven by *Kim et al.*<sup>[4]</sup> as part of static and dynamic photoluminescence studies. PDA has shown to increase the decay rate of an excited  $^3\text{MLCT}$   $[\text{Ru}(\text{bpy})_3]^{2+}$  sensitizer.



This demonstrates that instead of charge recombination in the excited inorganic sensitizer, the electron is transferred from the excited sensitizer to PDA. It is noticeable that the electron transfer on behalf of PDA is faster than charge recombination. Since the CdSe@CdS core-shell nanorods are also inorganic sensitizers, it is reasonable to assume that (regarding to the conditions, e.g. pH) in combination with PDA, PDA can either act as an electron donor (*Davis et al.*<sup>[3]</sup>) or an electron acceptor (*Kim et al.*<sup>[4]</sup>). This conclusively highlights the redox mediative behavior of PDA.

In addition, the broad (visible) absorption range from 400 nm to 700 nm<sup>[5]</sup>, should favor photon absorption. If there is a sufficient energy transfer between PDA and nanorods, the amount of photogenerated electrons sensitized by the nanorods might be increased and favor hydrogen production, while the distinct photoprotective property<sup>[2]</sup> of PDA prevents the nanorods from photodegradation.

Despite the many year of PDA research, the chemical/physical properties and the formation mechanism is not fully understood and is still under investigation.<sup>[50]</sup> Inspired by the biosynthesis of Eumelanin<sup>[53]</sup>, the proposed electrochemical polymerization mechanism of PDA is shown in Figure 12. In the process dopamine (DA) is oxidized electrochemically (E) to dopaminequinone (DAQ) followed by a chemical (C) cyclization (1,4-Michael addition) to leucodopaminechrome (LDAC). LDAC undergoes an electrochemical (E) oxidation to dopaminechrome (DAC), which chemically rearranges (C) to 5,6-dihydroxyindole. Once more an electrochemical (E) oxidation finally leads to 5,6-indolechinone, which is being polymerized to PDA.

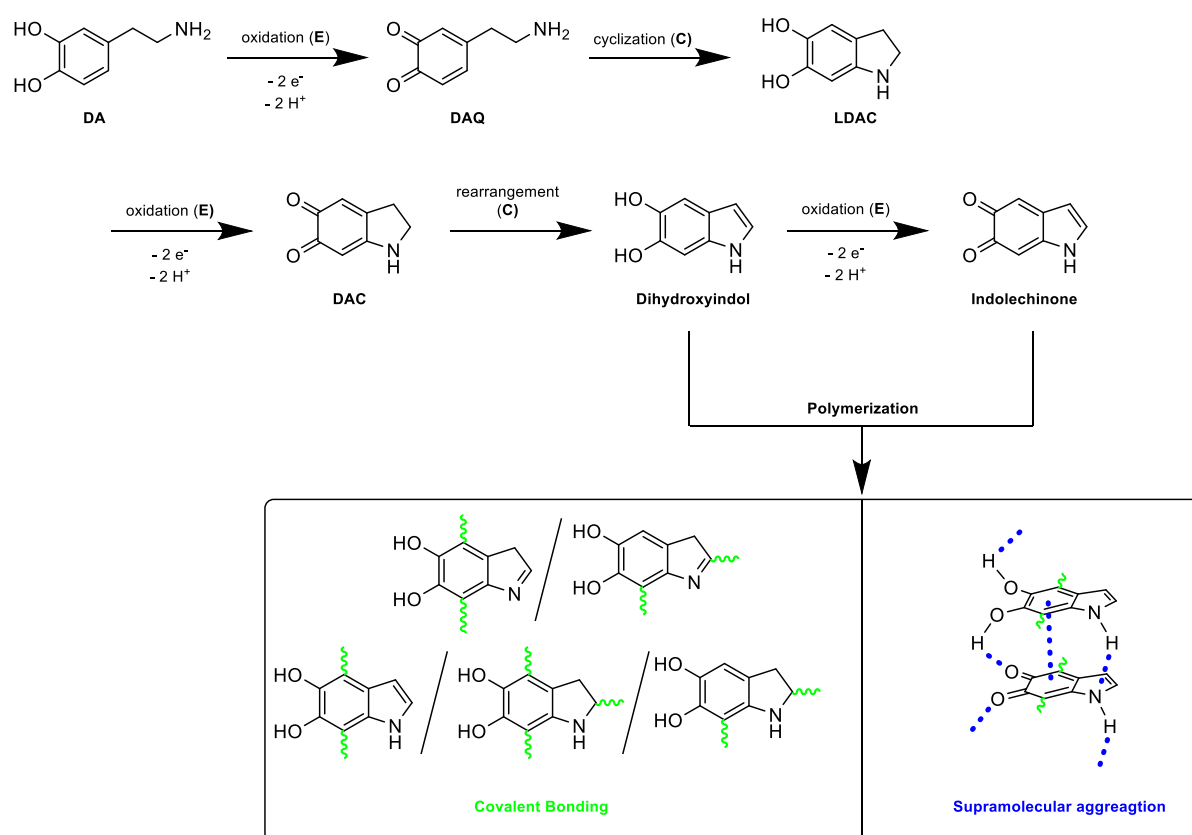


**Figure 12.** Proposed formation mechanism<sup>[54][55]</sup> and structure<sup>[56][57]</sup> of polydopamine (for clarity the corresponding covalently bonded quinone products were disregarded).

From cyclic voltammetry only the first steps of the mechanism could be identified as an ECE mechanism. It might be because either the intermediates are extremely unstable or the redox potentials are too close to be resolved via cyclic voltammetry.<sup>[54][55]</sup> The structure of PDA is also illustrated in Figure 12. On the one hand there are covalent bonds, which are formed due to oxidative polymerization of 5,6-dihydroxyindole or 5,6-indolechinone. On the other hand there is also a physical self-assembly pathway for the molecules, which include hydrogen bonding,  $\pi - \pi$  stacking and charge transfer interactions leading to supramolecular aggregation.<sup>[56]</sup>

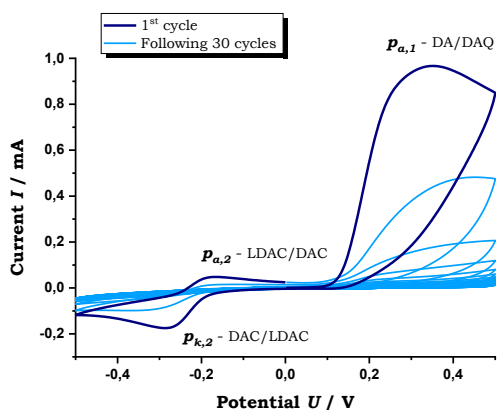


**Figure 13.** Cyclic voltammogram of a 30 Cycles PDA film, indicating a ECE mechanism.

The electrochemical deposition of PDA on a gold working electrode via cyclic voltammetry is shown in Figure 13, where only three distinct peaks are visible.  $p_{a,1}$  as the first anodic peak indicates an electrochemical oxidation, probably  $DA \rightarrow DAQ$ . The corresponding cathodic peak for  $DAQ \rightarrow DA$  at 0.12 V<sup>[54]</sup> cannot be observed, indicating an irreversible chemical turnover before DA can be formed again. This chemical turnover might be the cyclization of  $DAQ \rightarrow LDAC/DAC$ . Accordingly, peak  $p_{k,2}$  and  $p_{a,2}$  indicate the LDAC/DAC redox couple. Ultimately only the first three ECE steps are visible in cyclic voltammograms of PDA formation.

Further recent work by *Stöckle et al.*<sup>[58]</sup> has also shown that the electropolymerization via cyclic voltammetry can lead to a polydopamine film, whose thickness can be controlled by the number of voltammetric cycles. The thickness can be determined by atomic force microscopy (AFM) and X-ray photon spectroscopy (XPS), which was proven for a wide range of CV cycles from *Szelwicka*<sup>[59]</sup> in a non-published treatise (Figure 14). The decreasing peak area (Figure 13) and the decreasing response to the film thickness with each cycle indicates an insulating behavior of PDA as it was for the monomers used by *Davis et al.*<sup>[3]</sup>.

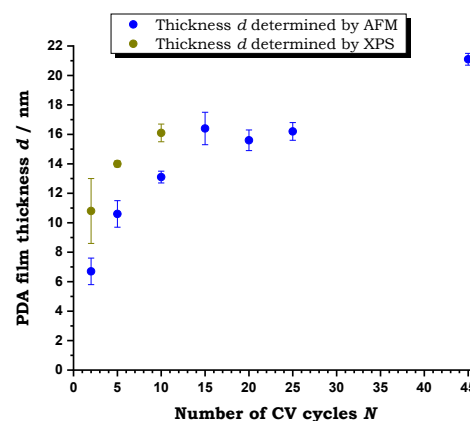


**Figure 14.** Dependency of the PDA film thickness  $d$  and the number of CV cycles  $N$ .

The characterization of PDA with common techniques like NMR spectroscopy, UV-VIS spectroscopy and gel permeation chromatography (GPC) is quite difficult since it is insoluble in water and organic solvents. Therefore, mostly solid state analysis (solid state NMR, EPR spectroscopy, powder XRD, FT-IR spectroscopy) of the product or soluble intermediates/degradation products are used to characterize PDA.<sup>[57]</sup>

## VI.Theoretical Basics

### VI.1. Basics of Electrochemistry

Nowadays electrochemistry has moved closer into the focus of scientists researching new possibilities of renewable energy technologies. Electrochemical techniques can be used to analyze chemical redox processes driven by an applied potential in order to measure redox potentials, investigate the reversibility of a chemical reaction, deposit materials electrochemically, examine catalyst efficiency, etc.<sup>[60][61]</sup> An occurring electrochemical redox process is theoretically divisible into two separated half-cells, which is shown in Figure 15 for the Daniel cell (classic galvanic cell). Since copper has a lower reduction potential than zinc, the oxidation of zinc and the reduction of copper is thermodynamically favored (see Equation (1)).<sup>[62][63]</sup>

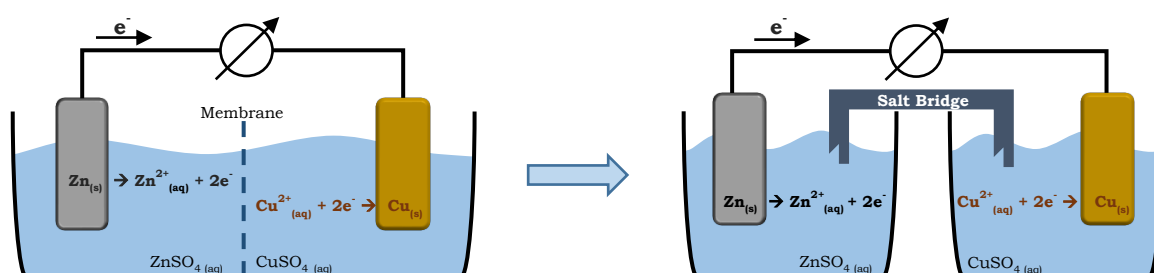


**Figure 15.** Dividing an electrical/galvanic cell into two theoretical half-cells, connected via a salt bridge.

In terms of thermodynamics the redox process is driven by the energy difference in their involved orbitals, which can be controlled by the applied voltage  $U$ . The electron accepting partner requires its lowest unoccupied molecular orbital (LUMO) to be energetically lower than the highest occupied molecular orbital (HOMO) of the electron donating partner to measure a spontaneous current flow. If this is not the case, a potential has to be applied to increase/decrease the potential of the electrons in the electrode and favor to an electron transfer (ET).<sup>[64][65]</sup>

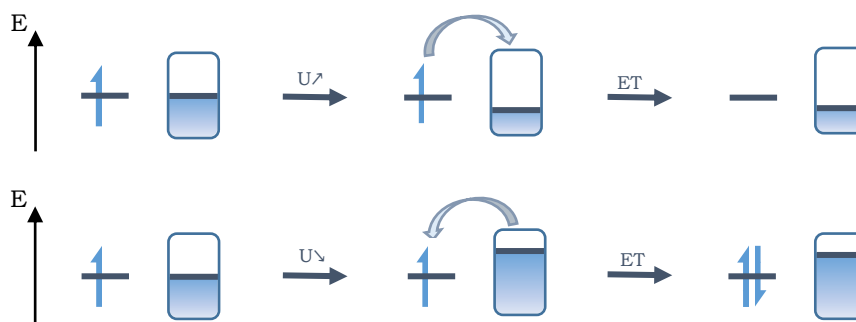


**Figure 16.** Schematic representation of the electron transfer (ET) between an agent and the electrode, where the electron energy at the electrode can be adjusted by an applied potential  $U$ . Increasing the potential  $U$  at an electrode favors an electron uptake, while decreasing  $U$  favors an electron donation.

As it is not possible to measure absolute values of those energy levels, the energy/potential is measured in reference to a defined secondary electrode (e.g. silver/silver chloride electrode or saturated calomel electrode) for defined conditions. The potential difference (electromotive force  $\Delta E$ ) is obtained by summing up all thermodynamical parameters and represents the capability of a system to create a voltage. The potential difference  $\Delta E$  is positive when the process is thermodynamically favored (exergonic) since the Gibbs enthalpy is then negative. *Vice versa* the potential difference is negative if the process is not thermodynamically favored (endergonic). The potential difference is described by the Nernst equation of the involved half-cells (reduction and oxidation):<sup>[66][65]</sup>

$$\Delta E = -\frac{\Delta G}{zF} = E_{\text{red}} - E_{\text{ox}} = \begin{cases} > 0 \text{ exergonic} \\ < 0 \text{ endergonic} \end{cases} \quad (1)$$

$$= \left( E_{\text{red},0} + \frac{RT}{zF} \ln \frac{[\text{ox}_1]}{[\text{red}_1]} \right) - \left( E_{\text{ox},0} + \frac{RT}{zF} \ln \frac{[\text{ox}_2]}{[\text{red}_2]} \right) = \Delta E_0 + \frac{RT}{zF} \ln \frac{[\text{ox}_1][\text{red}_2]}{[\text{ox}_2][\text{red}_1]} \quad (2)$$

|       |                          |     |                                   |                |                                |
|-------|--------------------------|-----|-----------------------------------|----------------|--------------------------------|
| $E_0$ | - Standard potential     | $F$ | - Faraday constant                | $[\text{ox}]$  | - Activity of oxidated species |
| $R$   | - Universal gas constant | $z$ | - Number of transferred electrons | $[\text{red}]$ | - Activity of reduced species  |
| $T$   | - Temperature            |     |                                   |                |                                |

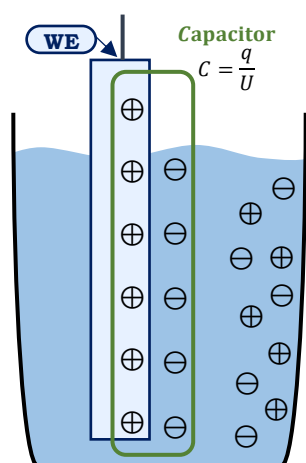
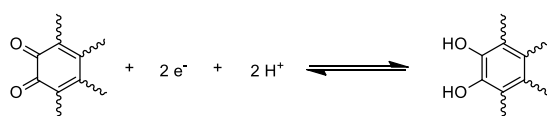


**Figure 17.** Formation of an electrical double at an electrode.

If a potential is applied to a conductive substrate but no current is passing, the electrode is building up positive or negative charges, depending on the nature of the applied potential. Since the charges need to be balanced, oppositely charged ions from the electrolyte diffuse to the electrode/solution interface forming an electrical double layer. An example of such a layer is shown in Figure 17 for a positively charged electrode. The system is now acting as a capacitor and the capacity  $C$  of the system is dependent on the applied potential  $U$  and the charge of the charge carrier  $q$ . The higher the applied potential is, the higher the capacity of the system becomes. Hence, the charged current is larger.<sup>[67]</sup>

Looking at the half-cell for the reduction of a quinone (Q) to a catechol ( $\text{H}_2\text{Q}$ ), the Nernst equation (2) can be rearranged to equation (3). Clearly the potential of a quinone/catechol redox process is directly dependent on the pH of the solution. Thereby, the catechol/quinone ratio should be either adjustable by the pH value or an applied potential.<sup>[68]</sup> Consequently, the electropolymerization of catechols, requires the use of a buffer while polymerizing to maintain constant pH.



$$\begin{aligned}
E_{\text{red}} &= \Delta E_{\text{red},0} + \frac{RT}{zF} \ln \frac{[\text{ox}]}{[\text{red}]} = \Delta E_{\text{red},0} + \frac{RT}{zF} \ln \frac{[\text{Q}][\text{H}^+]^2}{[\text{H}_2\text{Q}]} = \Delta E_{\text{red},0} + \frac{2.203 \times RT}{zF} \log \frac{[\text{Q}][\text{H}^+]^2}{[\text{H}_2\text{Q}]} \\
&= \Delta E_{\text{red},0} + \frac{2.203 \times RT}{zF} \left( \log \frac{[\text{Q}]}{[\text{H}_2\text{Q}]} + 2 \log[\text{H}^+] \right) = \Delta E_{\text{red},0} + \frac{2.203 \times RT}{zF} \left( \log \frac{[\text{Q}]}{[\text{H}_2\text{Q}]} + 2 \text{pH} \right) \quad (3)
\end{aligned}$$

Finally, it is important to mention, that most of the assumptions and references to the Nernst equation are only considering thermodynamic effect. Whether a reaction or more precisely an electron transfer of interest is occurring is still bound to additional kinetic effects. The kinetic effects in electrochemical cells are commonly known and summarized by the overpotential. The overpotential hence includes all additional parameters such as adsorption, charge-transfer, desorption and mass-transport (diffusion, convection and migration), which are not considered by thermodynamics. Therefore, it is an additional driving force, which needs to be expended for electrochemical processes. Oxygen or hydrogen generation in electrochemical cells are not excluded by overpotentials. Regarding to thermodynamics, a redox potential (vs. SHE) of 1.23 V is enough for oxygen evolution and 0 V for hydrogen evolution but the values are relative and shift for different conditions due to kinetic effect. Beside temperature, current density, solvent, additives, etc., the electrode also has a huge influence on the overpotential and plays therefore a major role. Table 1 shows some overpotentials for different electrode materials.<sup>[69]</sup>

**Table 1.** Overpotentials  $U_0$  for oxygen and hydrogen evolution at different electrode materials.<sup>[69]</sup>

| Electrode material | $U_0$ for O <sub>2</sub> evolution / V | $U_0$ for H <sub>2</sub> evolution / V |
|--------------------|----------------------------------------|----------------------------------------|
| Plat. platinum     | 0.46                                   | - 0.01                                 |
| Rhodium            | -                                      | 0.08                                   |
| Gold               | 0.96                                   | - 0.12                                 |
| Indium             | -                                      | - 0.80                                 |
| Tin                | -                                      | - 0.81                                 |

## VI.2. Cyclic Voltammetry

In contrast to a classical two electrode electrochemical cell (Figure 15) the general setup for cyclic voltammetry (CV) involves three electrodes (working, reference and counter electrode), a potentiostat and an electrolyte solution (see Figure 18).<sup>[70]</sup> The potentiostat controls the potential, which is applied on the working electrode and allows the measurement of the passed current.<sup>[71]</sup> CV is based on a linear potential sweep, where the potential is applied between the working electrode (WE) and the reference electrode (RE), while the current between the WE and the counter electrode (CE) is recorded.<sup>[72]</sup> At the WE the reaction of interest is taking place and it should therefore consist of a chemically inert material in the applied potential range. Common materials are glassy carbon, platinum or gold electrodes, which can be polished mechanically or chemically to obtain clean surfaces. Different electrode materials can lead to different electron transfer kinetics and influence the recorded CV curve.<sup>[61][64][73]</sup> For electrodes, which are deposited onto glass (for example indium tin oxide electrodes), also the layer thickness is an important parameter since the resistivity of a material is dependent on its thickness.<sup>[74]</sup>

An electrochemical process always coincides with a current flow. The main purpose of the CE is to redirect the current away from the RE and measure the current from the WE. To guarantee that the reactions at the CE do not disturb the reactions at the WE, the WE need to have a smaller surface area. The CE also needs to be inert because otherwise side products can deposit on it. For example, the polymerization conditions of dopamine lead to an oxidative deposition of PDA on a gold CE. Therefore, ideally the CE should be separated from the solution by a membrane or need be cleaned after each se.<sup>[64][73]</sup> The recorded applied potential is always in reference to the secondary reference electrode (RE). Common reference systems are Ag/AgCl, saturated calomel or standard hydrogen electrodes, which are separated by a frit from the solution. To reduce the liquid junction potential (resulting potential due to different mobility of ions in different solvents) the electrolyte solvent in the reference system, as well as the solvent of the electrochemical cell should match.<sup>[75][76]</sup> Additionally, in order to compare experimental data between

different systems, e.g. where another RE was used, calibration of the REs is required. Such a calibration (and at the same time a classic CV curve) is shown in Figure 19 for a Ag/AgCl RE. Calibration takes advantage of the well reported electrochemical behavior of  $K_4[Fe^{II}_2(CN)_6] / K_3[Fe^{III}_3(CN)_6]$ .<sup>[72][77]</sup> The area under a CV curve is proportional to the amount of electrons flowing. Fast scan rates decrease the size of the diffusion layer, hence higher currents are detected. According to the Randles-Ševčík equation<sup>[78][79]</sup> (4), the number of the electrons  $n$  can be calculated by the peak current  $i_p$ .

$$i_p = 0.4463 n F A C \left( \frac{n F v D}{RT} \right)^{1/2} \Leftrightarrow n = \frac{i_p}{0.4463 F A C} \left( \frac{n F v D}{RT} \right)^{-1/2} \quad (4)$$

|       |                       |     |                         |     |                          |
|-------|-----------------------|-----|-------------------------|-----|--------------------------|
| $i_p$ | - Peak current        | $A$ | - Electrode area        | $R$ | - Universal gas constant |
| $n$   | - Number of electrons | $C$ | - Analyte concentration | $T$ | - Temperature            |
| $F$   | - Faraday constant    | $v$ | - Scan rate             | $D$ | - Diffusion coefficient  |

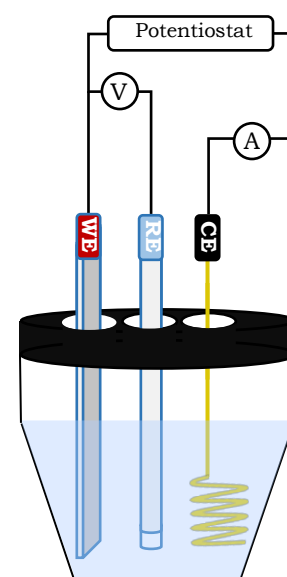


**Figure 18.** General set up of cyclic voltammetry.

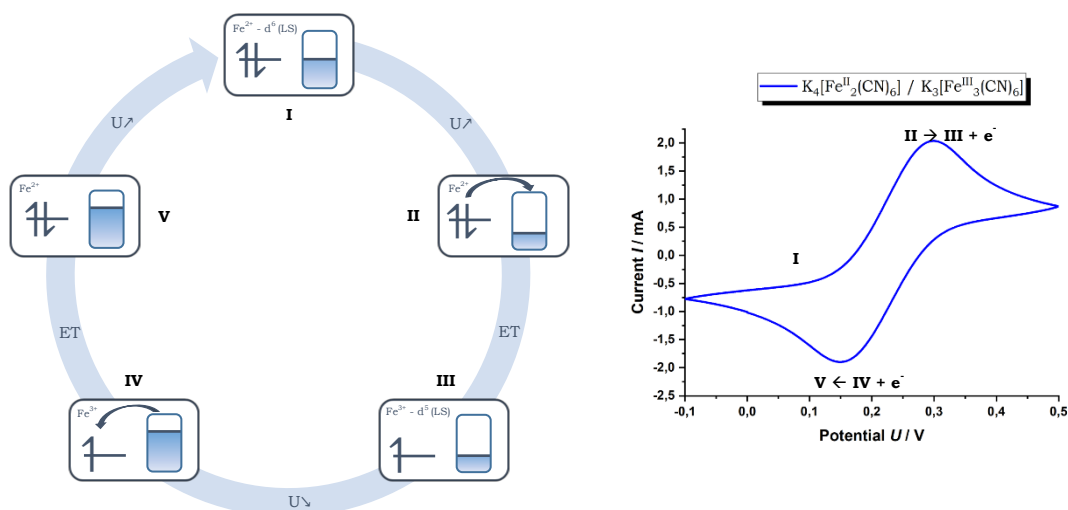


**Figure 19.** Representation of the electron transfer (ET) process controlled by an applied potential  $U$ . The CV curve is showing the oxidation/reduction of 12 mM  $K_4[Fe^{II}_2(CN)_6] / K_3[Fe^{III}_3(CN)_6]$  in phosphate buffer (pH = 7).

**Mass transport** in an electrochemical cell can be driven either by diffusion, convection or/and migration.<sup>[80]</sup> Since the molecular movements should be only driven by diffusion, mechanical stirring is prohibited (inhibit convection) and high electrolyte concentrations are used (inhibit migration). While sweeping into positive potentials, the diffusion of  $Fe^{II}$  to the WE leads to an oxidation to  $Fe^{III}$ . More  $Fe^{II}$  is subsequently diffusing to the electrode, is oxidized and the current is increasing and reaching its peak at  $\sim 0.3$  V.

Simultaneously the  $Fe^{III}$  concentration near the electrode is increasing and forms the so-called diffusion layer, which hinders further diffusion of  $Fe^{II}$  to the WE. Consequently, the current is decreasing above  $\sim 0.3$  V because less  $Fe^{II}$  is oxidized.<sup>[72][77]</sup>

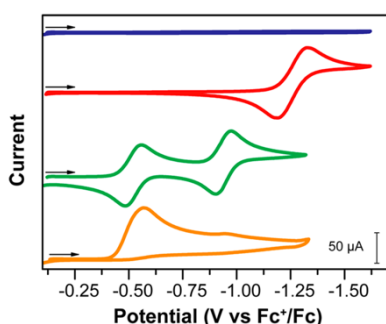
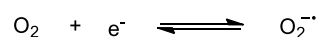


**Figure 20.** CV curve of  $N_2$  saturated (blue), air saturated (red),  $[CoCp(dppe)(CH_3CN)][PF_6]_2$  with  $N_2$  saturated (green) and air saturated (orange) electrolyte (0.25 M  $[NBu_4][PF_6]$ ,  $CH_3CN$  solution, 100 mV/s scan rate, 3 mm glassy carbon WE, 3 mm glassy carbon CE, silver wire pseudo-RE).<sup>[64]</sup>

The **presence of oxygen** can also influence electrochemical experiments because oxygen can undergo a reversible electron reduction to superoxide<sup>[81]</sup>:



The superoxide does not only overshadow important peaks, but can also react and/or inhibit reversible redox processes, like the one for  $[CoCp(dppe)(CH_3CN)][PF_6]_2$  (Figure 20)<sup>[64]</sup>. The green CV curve in Figure 20 shows the  $N_2$  saturated reversible redox processes, whereas in the presence of oxygen the processes seems to be irreversible (orange curve). Therefore, it is important to pre-bubble electrolyte solutions with nitrogen to remove the oxygen (blue and red curves).

The electrolyte solutions used in such an electrochemical cell show a **solution resistance**. Most of this resistance can be compensated by the potentiostat but the one between the RE and WE generally stays uncompensated. This effect was proven experimentally to be dependent on the geometry of the cell<sup>[82]</sup> and the non-ideal behavior of the reference electrode<sup>[83]</sup>. It can be minimized by increasing the electrolyte concentration (increase conductivity) and/or reducing the special separation between WE and RE.<sup>[73]</sup>

In general, cyclic voltammetry is a useful tool to study electron transfer steps in redox processes. Therefore, a notation has been introduced to distinguish between an electron transfer step *E* and a chemical reaction step *C*. The reversibility/irreversibility of an electrochemical process is indicated by a *r/i* subscript. If the electron transfer is slower than the chemical conversion, the process is irreversible. The mechanism in Figure 19 correspond to an  $E_r$  mechanism, whereas the PDA formation is more complicated and is formally described by as a ECECEE mechanism.<sup>[55]</sup>



## VII. Results and Discussion

For the detailed synthesis and characterization procedures/parameters see chapter IX. *Experimental Part*. Except for exemplary and/or significant recorded data, the synthetic PDA cyclic voltammograms as well as the recorded curves for the photocurrent measurements were marked and referred to the X. *Appendix*.

### VII.1. Polydopamine film characteristics

#### VII.1.1. Nitrogen vs. regular atmosphere

As discussed in chapter VI.2. *Cyclic Voltammetry*, the presence of oxygen can have a huge influence on the electrochemical behavior of redox active species. This was investigated for a 30 cycle PDA film. The PDA film was polymerized in regular atmosphere (RA film) (Figure 21A) and in a nitrogen saturated electrolyte/monomer solution under continuous N<sub>2</sub> flow (Figure 21B, N<sub>2</sub> film). The reported CV curves and a picture of the deposited PDA film on the gold electrodes are shown in Figure 21.

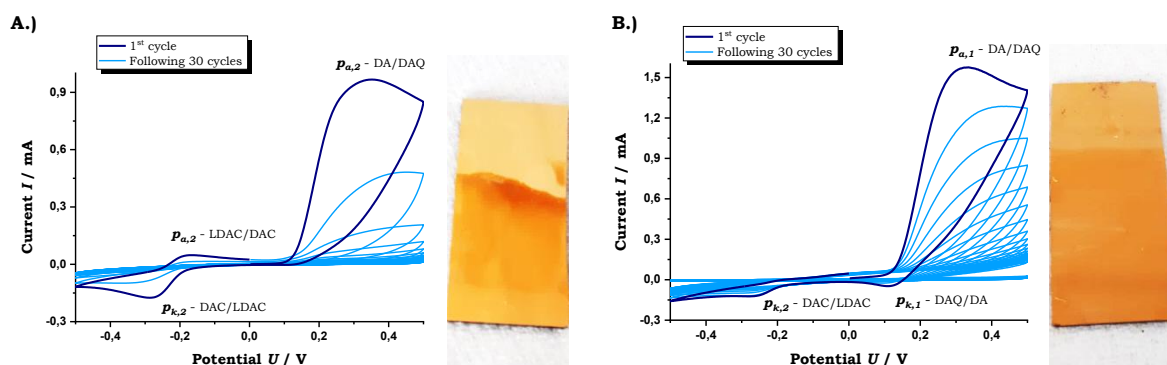


**Figure 21.** Cyclic voltammograms of 30 CV cycle PDA films. **A.)** In regular atmosphere (RA film). **B.)** Under Nitrogen atmosphere (N<sub>2</sub> film).

The drop in current per each cycle is a well-known behavior for the formation of PDA because it is insulating the electrode. The passivation of the WE hence decreases the current flow. Additionally, the electrode is passivated faster in the case for the RA film than for the N<sub>2</sub> film. This is probably due to the autoxidative behavior of dopamine (DA). The chemical driving force is significantly higher in the presence of oxygen than the electrochemical driving force, leading to a higher uncontrollable autoxidation of dopamine (less controllable PDA deposition). The balance between electrochemical and chemical driving force is also the reason why the peaks behave differently. While the DAQ → DA reduction peak  $p_{k,1}$  is not visible in the RA film voltammogram, it does appear in the N<sub>2</sub> film voltammogram. The dopamine formation (reduction) in the presence of oxygen at positive potential is not favored enough to be visible via CV since the chemical driving force predominated the electrochemical driving force. The LDAC → DAC oxidation peak  $p_{a,2}$  on the other hand is only visible in the RA film voltammogram since oxygen favors the formation (oxidation) and the chemical driving force again predominated the electrochemical driving force.

In Summary, the presence of oxygen plays a major role in controlling homogeneity and thickness of the generated PDA films.

This is additionally supported by the observations made at the edge of the films. For the RA film the film is getting darker the closer it gets to the edge, while the N<sub>2</sub> film seems to be more homogenous. Figure 22 illustrates this phenomenon schematically. At the air/solution interface the oxygen concentration is especially high, leading to a higher autoxidative deposition of PDA at the edge of the RA film.

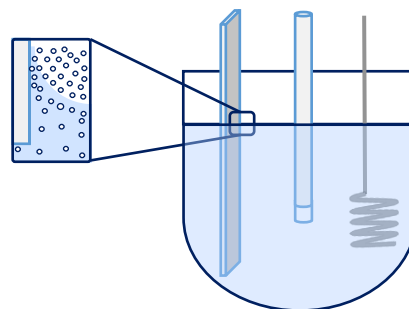


**Figure 22.** Schematical representation of the higher oxygen concentration at the water/air interface due to the meniscus.

### VII.1.2. Redox behavior: Controllability of catechol/quinone ratio

Regarding to the proposed mechanism for the envisaged photoelectrochemical cell in Figure 2, hydrogen production can be modulated by the pH of the solution. Catechol and quinone moieties of PDA are, depending on the pH, always in an equilibrium. In basic environment quinone groups are the major component and the equilibrium is favoring their formation. The premise of PDA acting as an efficient hole scavenger is driven by the chemical driving force acting on the minor catechol groups to be oxidized in basic pH. In acidic environment on the other hand, catechol formation is favored. Therefore, the self-recovery of PDA is based on the driving force towards catechol formation and is therefore favoring the reduction of quinone groups as the minor species in the equilibrium. Altogether, it is crucial to control the intrinsic catechol/quinone ratio of PDA in order to promote post-functionalization by a catalyst (or the attachment of a ligand which coordinates at the catalyst) as well as for hydrogen production modulation (switching between hole scavenging/hydrogen production and self-recovery).

According to the Nernst equation (3) the redox potential is depending on the pH of a solution. Hence, the catechol/quinone ratio of PDA should also be adjustable through the pH or an applied potential. Negative potential should therefore shift the equilibrium in favor to the catechol groups, whereas a positive potential should favor the quinone formation. In the following experiments the behavior of PDA in different pH as well as at different applied potentials was investigated.

#### a. pH dependency

In order to investigate the catechol/quinone ratio in PDA, three regular 5 cycle PDA films were prepared and placed separately in acidic buffer (0.1 M Acetyl Buffer pH = 3.99, Film **A**), in neutral buffer (0.1 M Phosphate Buffer pH = 7.01, Film **B**), and basic buffer (0.1 M Ammonium Buffer pH = 10.32, Film **C**) for 5 minutes to ensure that the system equilibrated and to check whether there are any stability issues, e.g. detachment from the electrode. CV curves were recorded afterwards for each film in the specific buffer. Considering only the first curve of the films reveals an interesting relation (Figure 23A). The current starts at different signs for a different pH. While for the basic buffer immediately a positive current was measured, the neutral one starts at around 0 A. This is probably due to the fact, that at basic pH the equilibrium of catechol/quinone is favoring quinone groups. The non-oxidized catechol groups in that equilibrium are now more easily ready to be oxidized in the basic medium.

This results to a lower potential needed for the oxidation since the chemical force is an additional driving force acting in the same direction as the applied potential does. That means, that the oxidation peak is shifted to the left on the x-axis. The same explanation applies to the behavior of the initial current for the acidic buffer. Here the catechol/quinone equilibrium is favoring the catechol formation. If a positive potential is now being applied, a higher (positive) potential is needed to oxidize the excess of catechol groups since the chemical driving force is now acting against the formation of quinone groups and a higher energy input (potential) is needed.

Despite the initial current, which gives valuable information about the favored species, Figure 23A additionally reveals a relation between the redox potential and the pH of a solution. It is observable that a basic pH is shifting the potential towards negative potentials (Figure 23A, **0**  $\rightarrow$  **1**), while an acidic environment is shifting them towards positive potentials (Figure 23A, **0**  $\rightarrow$  **2**).

This is supported by the only visible peak in the voltammogram of the neutral curve (Figure 23A, **3**  $\rightarrow$  **4**). Interestingly, two peaks appear in the basic voltammogram (blue). These peaks are not visible for the neutral and acidic curves because they appear at higher potential under these conditions. Therefore, a control voltammogram was measured in neutral pH and confirmed the two peaks appearing at 0.52 V and 0.73 V (Figure 23B). The two peaks  $p_{a,1}$  and  $p_{a,2}$  can be assigned to the two catechol groups being oxidized.

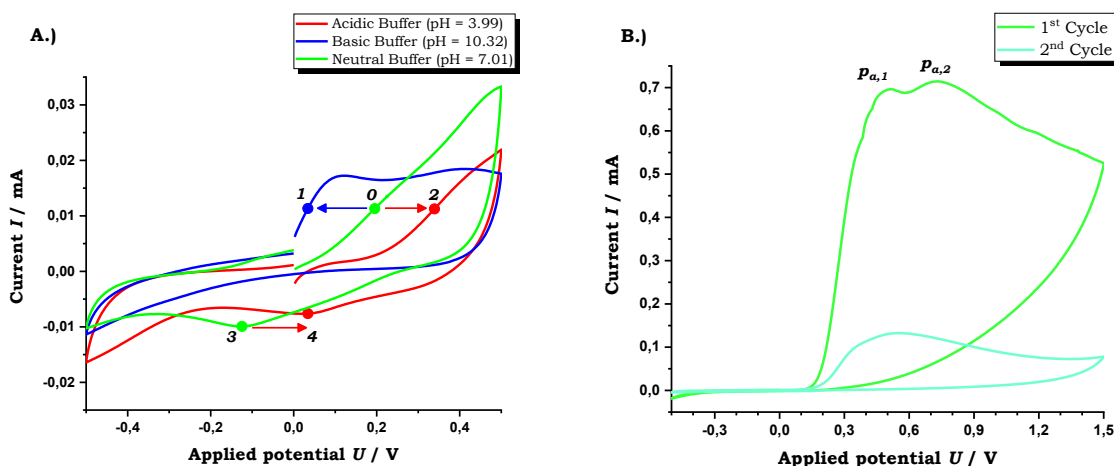


**Figure 23. A.)** Overlay of initial CV curve for PDA films placed in different pH buffers. Red: 0.1 M acetyl buffer pH = 3.99 (Film A), green: 0.1 M phosphate buffer pH = 7.01 (Film B) and blue: 0.1 M ammonium buffer pH = 10.32 (Film C). **B.)** CV of a PDA film in neutral buffer. Potential sweeps from  $-0.5$  V to  $+1.5$  V and reveals two anodic peaks ( $p_{a,1}$ ,  $p_{a,2}$ ) for the 1<sup>st</sup> cycle.

The pH dependency on redox potentials (shift on x-axis) is a well-known phenomenon and in accordance with the Nernst equation. *Palomäki et al.*<sup>[84]</sup> showed a similar behavior for different catechols, such as benzene-1,2-diol (catechol), 4-Methylbenzene-1,2-diol (methylcatechol) and dopamine. The results are summarized in Table 2. Reduction peaks in basic pH are hardly visible, due to irreversible chemical processes, such as polymerization. Only for methylcatechol a reduction peak is clearly visible (the positive inductive effect of the methyl group probably decreases the electron density in the ring, making it less attractive for nucleophilic attack needed for polymerization).

**Table 2.** Oxidation and reduction peaks of catechol, methylcatechol and dopamine for acidic (pH 0.65), neutral (pH 7.2) and basic (pH 10.8) pH solutions (potential sweep:  $-1$  V to  $1.5$  V, scan rate:  $0.05$  V/s, RE: Ag/AgCl with  $0.197$  V vs. SHE, CE: Pt wire, WE: tetrahedral amorphous carbon).

| Catechol/Quinone      | pH   | Oxidation peak | Reduction peak |
|-----------------------|------|----------------|----------------|
| <b>Catechol</b>       | 0.65 | + 0.7          | + 0.34         |
|                       | 7.20 | + 0.34         | + 0.01         |
|                       | 10.8 | + 0.03         | -              |
| <b>Methylcatechol</b> | 0.65 | + 0.61         | + 0.35         |
|                       | 7.20 | + 0.29         | - 0.01         |
|                       | 10.8 | - 0.01         | - 0.12         |
| <b>Dopamine</b>       | 0.65 | + 0.67         | + 0.39         |
|                       | 7.20 | + 0.39         | 0              |
|                       | 10.8 | + 0.04         | -              |

Running additional CV cycles for the films A, B and C reveals that likewise to the polymerization of dopamine, additional CV cycles cause an irreversible insulating chemical turnover at the electrode (Figure 24A1, B1 and C1). But taking a closer look at the first and fifth cycle, reveals different behavior (Figure 24A2, B2 and C2). While peak  $p_{a,1}$  and  $p_{k,1}$  decrease with further cycles, peak  $p_{k,2}$  surprisingly increases. This means that a chemical turnover destroys the functionalities at  $p_{a,1}$  and  $p_{k,1}$  equally. Hence, it is reasonable to assume that  $p_{a,1}$  and  $p_{k,1}$  correspond to a redox couple (probably DA/DAQ).

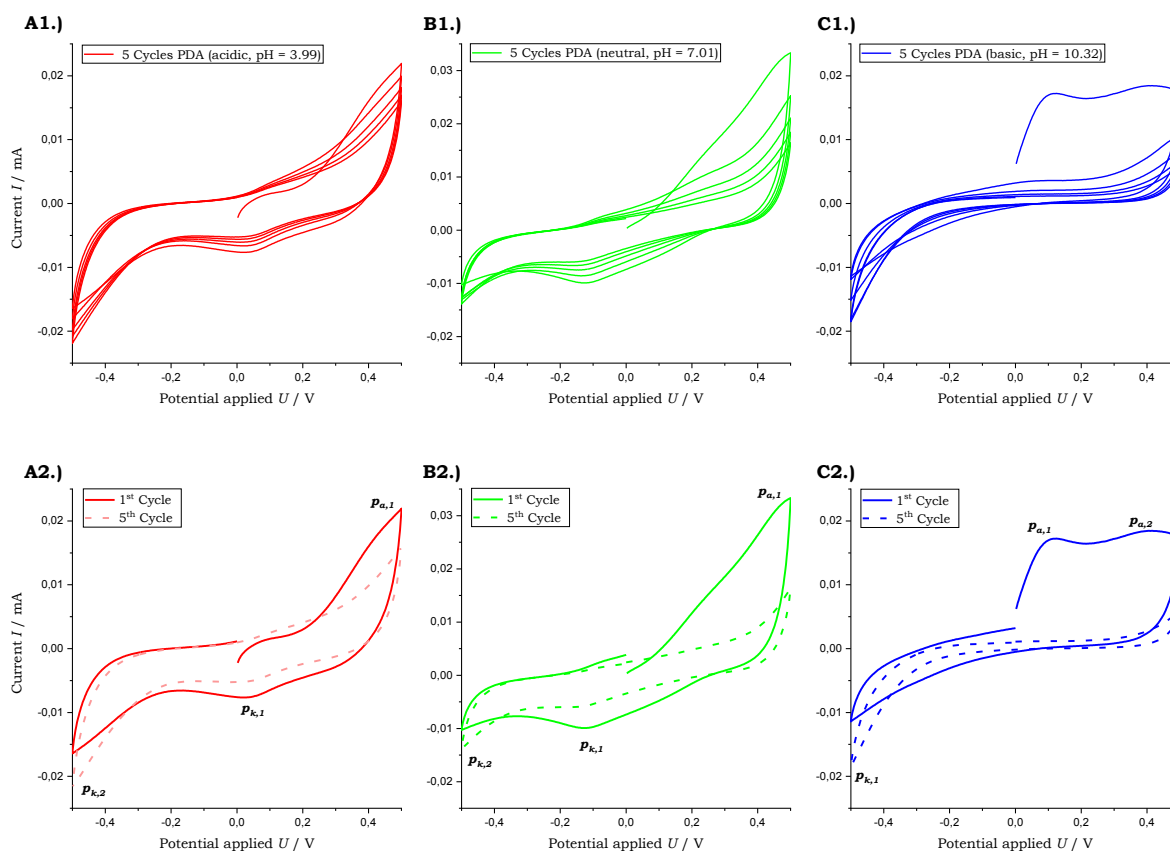


**Figure 24.** CV curve of three different 5 Cycle PDA film in **A.)** acidic pH (phosphate buffer), **B.)** neutral pH (ammonium buffer), **C.)** basic pH (acetyl buffer). The first row shows all cycles, while the second row highlights the first and fifth cycle to the corresponding film.

Their decrease appears to be greatest at basic pH. Since quinone groups, are the major groups in basic pH, the decrease might be due to inter-/intramolecular nucleophilic attacks by the amino moieties for example. Quinone moieties are irreversibly destroyed and the peaks decrease. In turn a new species is formed, which can be reduced further. Hence, peak  $p_{k,2}$  is increasing.

### b. potential dependency

Beside the pH value, the redox groups should also be also controllable by an applied potential. Since it is easier to switch between potentials rather than switching the buffer/electrolyte solution, a series of measurements was performed to investigate the influence of an applied potential on PDA. Therefore, after preparing a 5 cycle PDA film, a potential of + 0.4 V (first run) was applied, followed by a recorded CV curve. Then a negative potential of - 0.4 V (second run) was applied for 5 minutes on the same film and a CV curve was taken again. Voltammograms were recorded 5 seconds after film manipulation via the potential, to prevent flawed data by overlapping effects due the previous applied potential. In Figure 25 these two voltammograms are shown together with a regular start without prior manipulation. The corresponding integrated peak areas are shown in Figure 26 and Figure 27.

At first glance similar characteristic initial currents as the ones for the pH measurements in chapter *a. pH dependency* are observed. But especially, the fact that the oxidation area (1.37  $\mu\text{AV}$ ) is much smaller than the followed reduction area (5.1  $\mu\text{AV}$ ) indicates a different behavior. Generally, reduction areas should be smaller due to chemical turnovers, which take place in the positive potential range after quinone groups were formed. Therefore, in the case of an applied potential other more complex relations need to be taken into consideration.

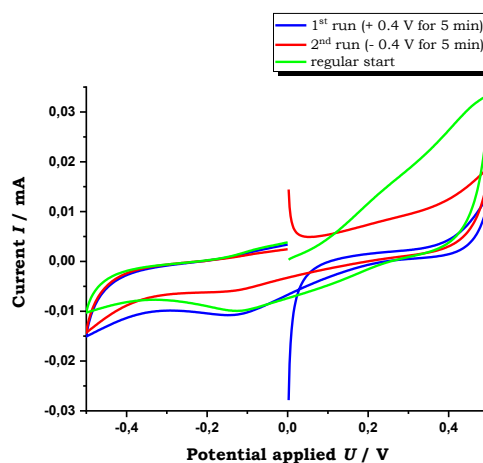


**Figure 25.** Overlay of CV curves for pretreated PDA Films via an applied potential (green: none, red: - 0.4 V for 5 minutes, blue: + 0.4 V for 5 minutes).

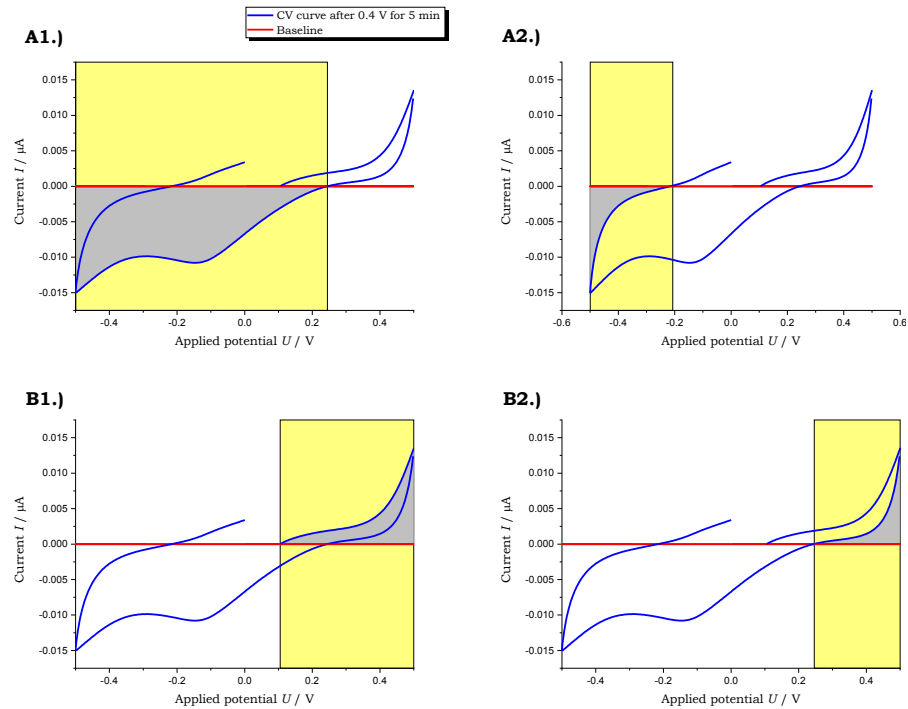


**Figure 26.** Masked areas (grey) of a cyclic voltammogram for the peaks of a 5 cycle PDA film after applying a potential of +0.4 V for 5 minutes. Areas were calculated according to a baseline at 0 A (red). **A.)** The reduction peak area was calculated by subtraction of masked areas in **A1** and **A2**. **B.)** The oxidation peak area was calculated by subtraction of the masked areas in **B1** and **B2**. Charge current was disregarded.

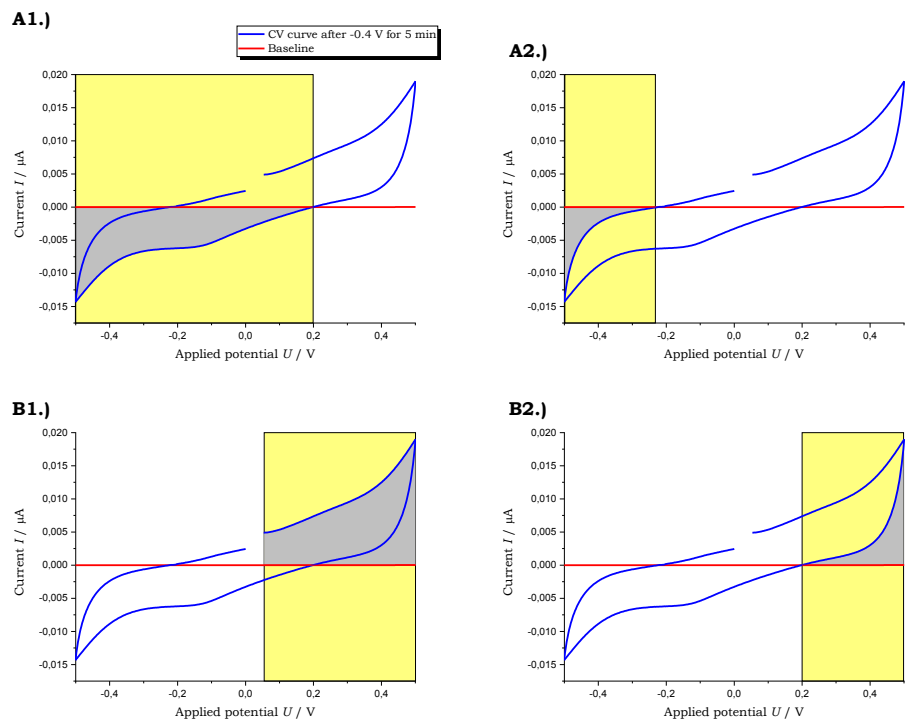


**Figure 27.** Masked areas (grey) of a cyclic voltammogram for the peaks of a 5 cycle PDA film after applying a potential of -0.4 V for 5 minutes. Areas were calculated according to a baseline at 0 A (red). **A.)** The reduction peak area was calculated by the subtraction of the masked areas in **A1** and **A2**. **B.)** The oxidation peak area was calculated by the subtraction of the masked areas in **B1** and **B2**. Charge current was disregarded.

Applying a positive potential for 5 minutes leads to an extreme negative current at the beginning of the analytical CV, which is dropping sharply to zero. This negative current has two origins. Mainly the current is based on charging current, which was formed at the surface of the WE while applying the positive potential. The WE was charged positively, which means that on the surface positive charge was accumulated, while the electrolyte solution near the WE was accumulating negative ions (electrical double layer). These two layers were separated by solvent and PDA. While jumping from the applied + 0.4 V to 0 V for starting the CV measurement, the excess of positive charges on the surface (charging current) need to be balanced by electrons from the electrode, leading to a negative initial current. Hence, the current flow right at the beginning is dropping fast from  $-0.028$  mA to 0 mA ( $U = 0$  V  $\rightarrow$  0.105 V) until the charge was compensated. Then oxidation of the PDA film was taking place, which increased the current again. Since the area is a quantitative measure of the electron flow, it seems like there is more reduction occurring than oxidation. This is probably due to prior oxidation of PDA while forming the charge current. Since the surface of the WE was positively charged and PDA is in between of the electrical double layer (right at the interface to the positively charged surface) it is quite possible that there was already some oxidation happening (Figure 28A). This means that applying + 0.4 V to the system indeed leads to oxidation of PDA (catechol  $\rightarrow$  quinone). If now a negative potential of  $-0.4$  V is applied, a similar charging phenomenon is observable. The surface of the WE is charged negatively. Hence, an electrical double layer is forming between the WE and the electrolyte, while PDA is in-between both layers (right at the negatively charged interface to the WE). Again, current is being charged by the double layer. That charge is compensated right at the beginning of the analytical CV. The balance of this charging current is noticeable through the positive current which is dropping fast right at the beginning from 0.014 mA to 0.005 mA ( $U = 0$  V  $\rightarrow$  0.054 V) and increases again towards + 0.5 V. But unlike the first case, the oxidation area (3.78  $\mu$ AV) and reduction area (3.11  $\mu$ AV) are quite similar. That means that no (or less) reduction at the WE/PDA interface was occurring while forming the electrical double layer and the charging current (Figure 28B). This means that  $-0.4$  V is not a negative enough potential to reduce PDA (quinone  $\rightarrow$  catechol) sufficiently. This is additionally supported by the charging currents in both cases. For the prior positive applied potential, the maximum of charging current is at  $-0.028$  A. The prior negative applied potential exhibits a charging current of only 0.014 A. This could mean that there is a kinetic barrier in the system, which cannot be overcome by an applied potential of  $-0.4$  V. Such kinetic barriers are well known in electrochemical cells and can be caused due to overpotentials at the electrode (see end of chapter VI.2. *Cyclic Voltammetry*).

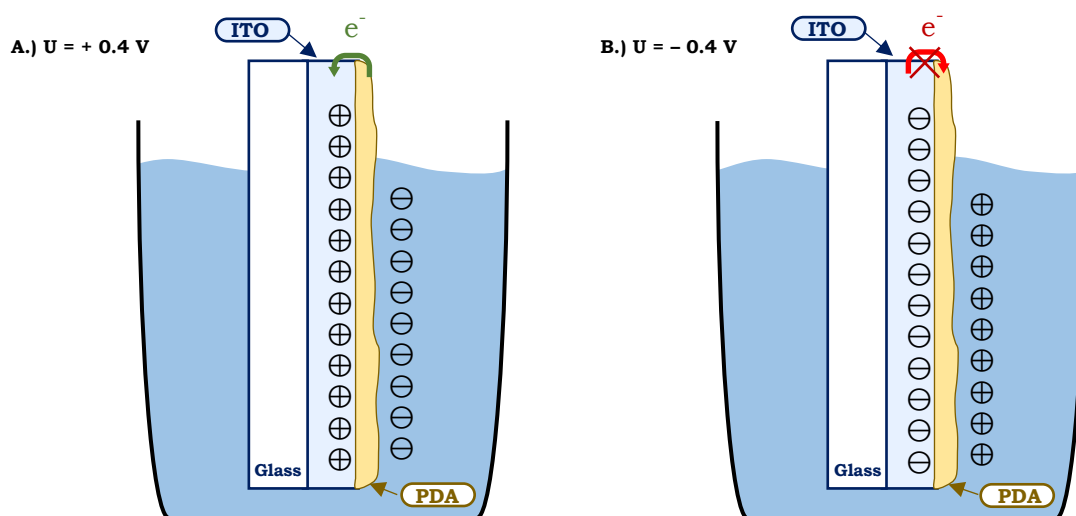


**Figure 28.** Illustration of the electrochemical double layer at **A.)**  $U = +0.4$  V with an electron transfer at the ITO/PDA interface and **B.)**  $U = -0.4$  V without an electron transfer at the ITO/PDA interface.

All together the equilibrium between catechol/quinone can be shifted with the pH of a solution, which is a necessary property for our catalytic system to modulate hydrogen production and attach different catalyst by simple chemistry. Unfortunately, it is not possible to get quantitative results on the equilibrium by cyclic voltammetry, in order to adjust the catechol/quinone ratio to a specific value. Sweeping the potential in different pH seems to be a useful technique to investigate the complex mechanism and structure in PDA, but it would be impractical to sweep the potential (especially in into the positive potential range) while the device for hydrogen production is running because the film undergoes an irreversible chemical turnover.

Due to the instability of the formed quinone groups to nucleophiles, chemical processes might interfere and hinder smooth operation of the device. But this is a manageable disadvantage since hydrogen is produced at negative potentials anyway. The adjustment of the catechol/quinone equilibrium shows to be also somehow possible but leaves to many questions open in order to be used in the envisaged product and would need further investigations. Although it would be a helpful feature, it is not necessary to include regulations over the potential into the envisioned device since pH regulations have already show promising results.



## VII.2. New experimental set up and design

It was already mentioned that the experimental setup could have an influence on the collected data from cyclic voltammetry. Namely, the uncompensated resistance from the solution is dependent on the setup and is minimized by minimizing the distance between WE and RE. To collect accurate data the distance should be constant and as short as possible. In addition to the high costs of the ITO and gold WE it was decided to polymerize in a cuvette (cut to 30 mm length) instead of a vessel similar to the one in Figure 18 (old setup). A suitable cuvette cap was therefore designed (Figure 29B). It contains a slit for the ITO/gold WE, a small hole for the CE, which is wrapped around the RE. For the reference electrode another hole was in close proximity to the WE. Beside the small hole for the CE two additional holes were incorporated for a N<sub>2</sub> in- and outlet.

Additionally, to the cuvette cap a corresponding cuvette holder was designed (Figure 29A). The cuvette holder is containing a screw to lift the cuvette in order to irradiate a chosen area on the film. The cuvette holder incorporates four symmetrical ports, which are useful for different characterization techniques. With this construction it is for example possible to measure the fluorescence in a 90 ° angle relative to the incoming beam. The PDA film as well as the solution (detecting degradation products, e.g. oligomers or release of nanorods) might be characterized while irradiating the (functionalized) PDA films from behind. Beside fluorescence spectroscopy it is also possible to measure UV-VIS spectroscopy (180 ° relative to the incoming beam) of the film or the solution while irradiating the sample from behind.

For conducting photocurrent measurement in chapter VII.3. *Photocurrent optimization* only one port for the irradiation is necessary. The setup for this is shown in Figure 30.

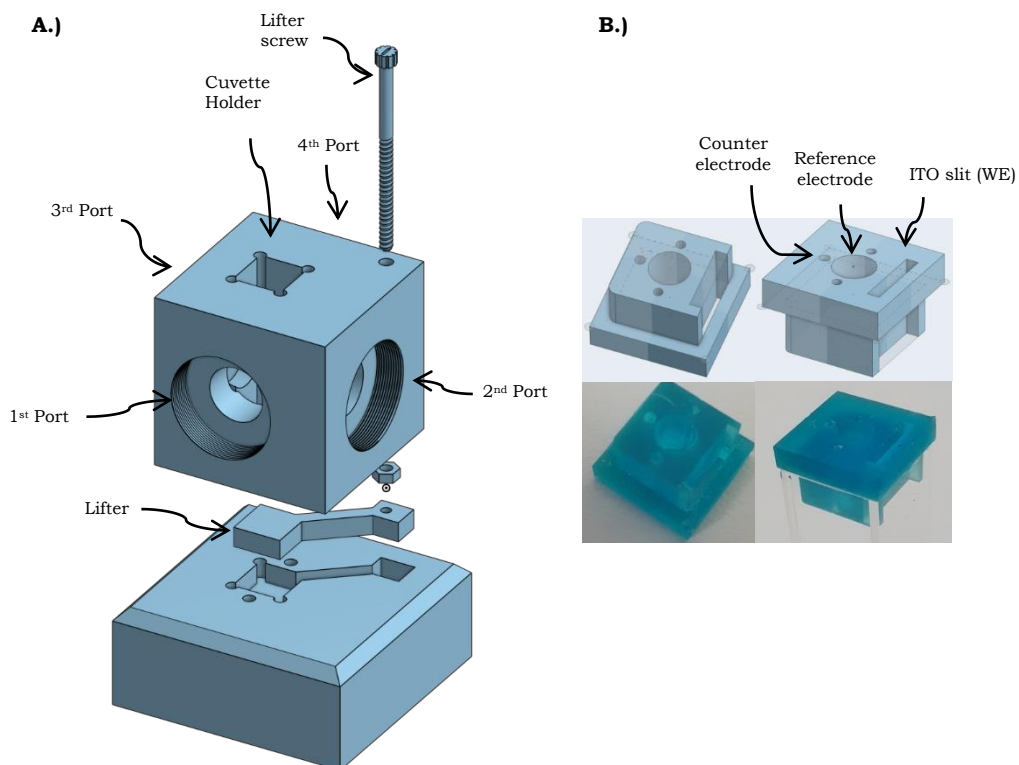


**Figure 29.** New 3D design of the cuvette holder (left) and the cuvette cap (right). Designed via *OnShape CAD*.

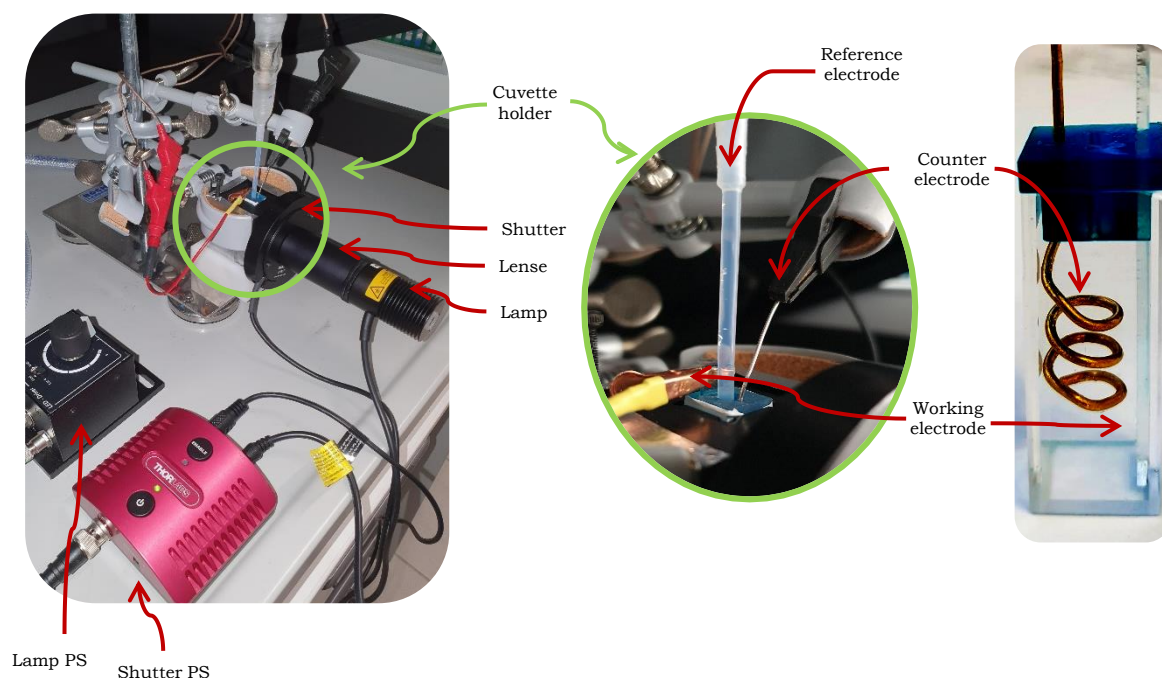


**Figure 30.** Final experimental set up for the photocurrent measurements, containing the power supply (PS) for the lamp and for the shutter as well as the UV lamp for irradiation, a lens to focus a 5 mm diameter light cone and a shutter to enable/disable irradiation. Highlighted is the designed cuvette holder and the corresponding cuvette (cap) showing the minimized distance between CE/RE and WE.

### VII.3. Photocurrent optimization

The released photocurrent was electrochemically recorded and used as a benchmark for the system to generate electrons, which in turn reduce hydrogen if a suitable (co-)catalyst for hydrogen production is chemically bound to the PDA surface. Functionalization can be achieved by taking advantage of the amino functionalities or catechol/quinone moieties in PDA to attach a catalyst or a ligand, which can coordinate to an inorganic complex (catalyst) by ligand exchange. To achieve this objective two methods were used to measure the photocurrent on an ITO WE. The sweeping potential photocurrent measurement (SPM) method was used to investigate on one hand the stability of the system (optimization of PDA to nanorods ratio) and on the other hand to identify a specific potential where the highest photocurrent is being released (optimization of the applied potential for electron generation). In another experiment, the potential was held constant during photocurrent measurements (CPM) and different hole scavengers were compared regarding to their ability to increase the photocurrent. Both methods were performed using strong irradiation conditions (100 mW, 100 min for SPM, 30 min for CPM) to push the system towards its limits in order to find the optimized conditions and extend the long-term stability of the system. The irradiation with high intensity and over long times, led to complete degradation of the CdSe@CdS nanorods, as confirmed by SEM measurements (see X. Appendix Figure 61/Figure 62 (pre-irradiation) and Figure 63 (post-irradiation)).

#### VII.3.1. Sweeping potential measurement (SPM)

The optimized composition of PDA-to-nanorods was evaluated by determining their contribution to the photocurrent (average mean photocurrent  $I$ ) and to the film stability (half-life  $\tau$ ) determined by SPM. Therefore, the spin coated nanorod concentration  $c$  and number of synthetic PDA CV cycle  $N$  (proportional to film thickness) in single and combined films, as well as the length of the nanorods were considered. In Figure 31 and Figure 32 HR-TEM and TEM pictures of two different nanorod sizes are shown. The short ones have a size of  $(13 \pm 1) \times (3 \pm 0.4)$  nm (aspect ratio  $R = (4.3 \pm .7)$  nm) and the longer ones of  $(46 \pm 4) \times (5.2 \pm 0.6)$  nm ( $R = (8.9 \pm 1)$  nm).

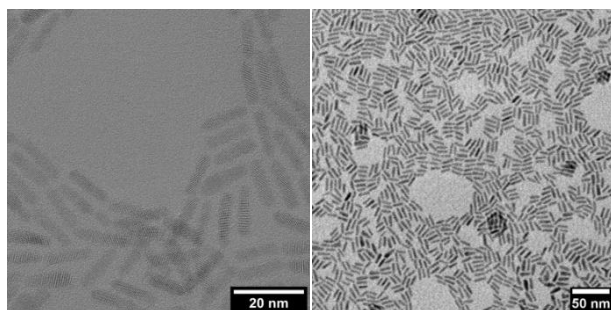


**Figure 31.** HR-TEM (left) and TEM (right) images of CdSe@CdS nanorods. Length  $l = (13 \pm 1)$  nm, width  $w = (3 \pm 0.4)$  nm.

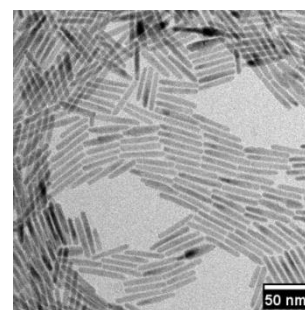


**Figure 32.** TEM image of CdSe@CdS nanorods. Length  $l = (46 \pm 4)$  nm, width  $w = (5.2 \pm 0.6)$  nm.

The data processing for the recorded SPM raw data is shown exemplary for a pure 5 cycle PDA film. Since the lamp was turned on/off for specific time intervals, the recorded raw data show steps for the lamp-on time (Figure 33A). In order to calculate the photocurrent, the lamp-off data were interpolated (Figure 33B) and then subtracted from the lamp-on curve (Figure 33C). The absolute values of the lamp-on blocks were averaged (absolute mean photocurrent  $I$ ). The sweeping measurement was repeated  $N = 30$  times, leading to a total of 30 absolute mean photocurrents. These currents show an exponential trend (Figure 33D) and were fitted by an exponential decay function (5) which in turn yielded the half-life  $\tau$ . Seen that way, the half-life has a ‘unit’ of  $\left[ \frac{1}{\text{Number of absolute mean measurements } N} \right]$ . For the sake of clarity this theoretical unit was not mentioned hereinafter.

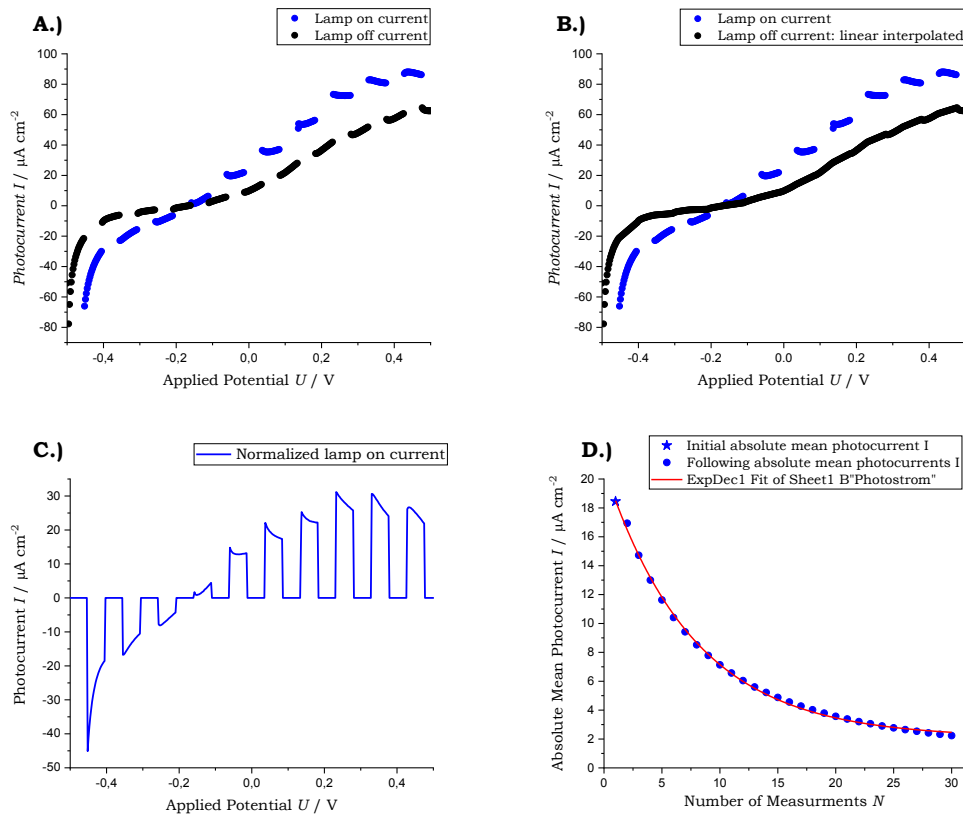


**Figure 33.** Data processing for the sweeping potential measurement (SPM). **A.)** Raw Data. Current curves for the lamp on/off times. **B.)** Interpolated lamp-off curve (Baseline). **C.)** Subtracted Baseline leads to the absolute mean photocurrent  $I$ . **D.)** Exponential decay fit of the absolute mean photocurrents  $I$ . Highlighted is the initial absolute mean photocurrent  $I_i$ .

$$y = y_0 + A \cdot e^{-\frac{N}{\tau}}, \text{ with } \tau = t \cdot \ln 2 \quad (5)$$

$y$  – Peak current  
 $y_0$  – Y-axis offset  
 $A$  – Amplitude

$N$  – Number of measurements  
 $\tau$  – Half-life  
 $t^{-1}$  – Decay rate

### a. NR concentration series

In order to analyze the dependency of the average mean photocurrent  $I$  and the half-life  $\tau$  on the nanorod concentration, PDA was always polymerized with 5 CV cycles, while the concentration of the spin coated nanorod solution was varied from 0.05 mg/mL to 2 mg/mL. The result is shown in Figure 34. The recorded data show a correlation of the initial absolute mean photocurrent  $I_i$  to the half-life  $\tau$ . The higher the concentration of the nanorods is, the higher the photocurrent  $I_i$  and lower the half-life  $\tau$  get. Since the nanorods are degradable, increasing the absolute amount of nanorods (degradable material) consequently leads to higher detectable degradation. More precisely, increasing the amount of nanorods, increases the photocurrent  $I$ , but lowers the half-life  $\tau$ . Depending on the application, conditions that yield a higher photocurrent (1.2 mg/mL sample) but shorter half-life or better stability (0.4 mg/mL sample) but lower photocurrent can be chosen through the appropriate composition. A good compromise between moderately high photocurrent and acceptable film stability is found for the film consisting of (0.4 – 0.8) mg/mL spin coated nanorods, which were embedded into a 5 cycle PDA film.

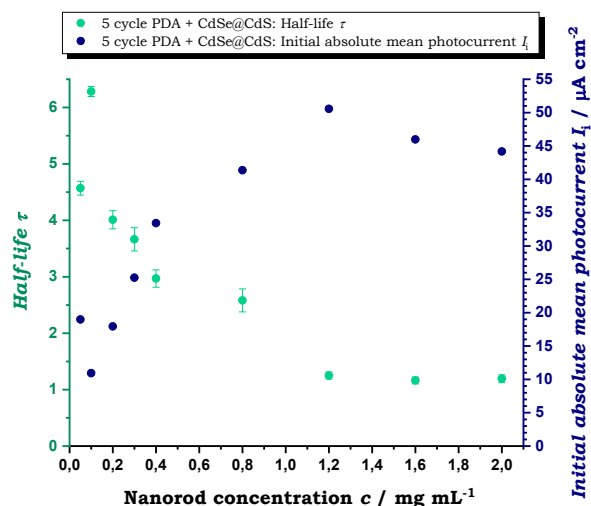


**Figure 34.** On WE (ITO) spin coated nanorod concentration series for 5 CV cycle PDA films. The nanorod concentration  $c$  is plotted against the calculated initial absolute mean photocurrent  $I_i$  and the half-life  $\tau$ .

### b. PDA cycles series

The dependency on the number of polymerized PDA CV cycles on the initial absolute mean photocurrent  $I_i$  and the half-life  $\tau$  was also investigated. Therefore, the collected data of pure ITO, pure NR, and pure PDA were compared to combined films consisting of 5, 15 and 30 PDA cycles. Because attempts were made to improve the photostability, film conditions with a low half-life were needed to see even small changes on the half-life. Therefore, the spin coated NR concentration was held at 1.2 mg/mL. The results are summarized in Figure 35. The pure ITO baseline shows an extremely low and therefore negligible photocurrent. Interestingly ITO also seems to degrade (see Figure 103 in the *Appendix*). The pure NR, as expected, show a high photocurrent together with an extremely low half-life. For an additional 5 cycle PDA film on top of the NR, the photocurrent is increasing, which might be due the ability of PDA to create a photocurrent for itself and due to synergistic effects (hole quenching by PDA) since the half-life of the system is increasing as well.

In contrast, further increasing the number of PDA cycles leads to a decrease of the photocurrent. This might be a result of the photoprotective<sup>[2]</sup> property of PDA, whereby PDA absorbs some of the light (broad absorbance range<sup>[5]</sup>). In accordance to that, the photostability of the system (half-life) is increased. Despite the small difference in the initial photocurrent for pure PDA in comparison to the nanorods coated in 30 CV cycles of PDA, the difference in half-life is significant. This is probably due to degradation of the nanorods, which may still occur. The nanorods might be photo-protected to some degree by the PDA, but since the potential is also sweeping to positive potentials electrooxidation additionally to photooxidation may occurs in the nanorods. In pure PDA films, no significant influence of the film thickness on the photoelectric properties was found (see 5 cycle vs. 45 cycles in Figure 64 of the *Appendix*). Therefore, all the films with different PDA/nanorod ratio in Figure 35 can be compared to a pure 5 cycle PDA film.

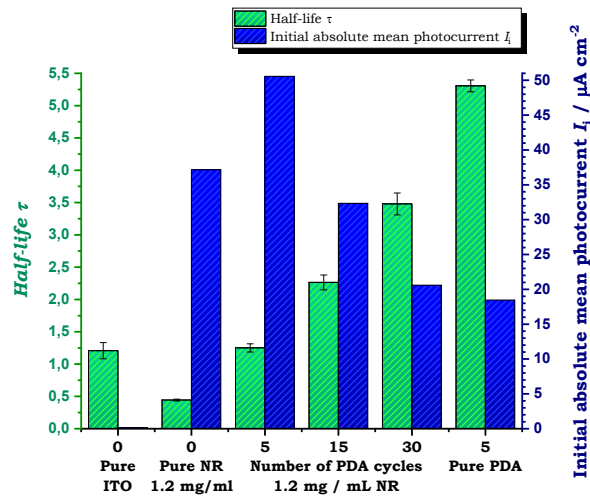


**Figure 35.** A comparison of a spin coated nanorod concentration of 1.2 mg/mL for different numbers of PDA cycles relative to pure ITO, pure nanorods (1.2 mg/mL) and pure PDA (5 cycles).

In consideration of all the presented results, for each nanorod concentration there is an ideal number of PDA cycles. For example, the nanorod concentration of 0.4 mg/mL + 5 PDA cycles ( $I_i \sim 32 \mu\text{A cm}^{-2}$ ,  $\tau \sim 2.3$ ) has similar properties as a film with 1.2 mg/mL + 15 PDA cycles ( $I_i \sim 34 \mu\text{A cm}^{-2}$ ,  $\tau \sim 2.4$ ). It is noticeable that the photoelectrical film characteristics are similar if the compound ratio stays the same. This means that (0.4 – 1.2) mg/mL nanorods + (5 – 15) PDA cycles have the same properties if the PDA/nanorod compound ratio is at  $12.5 \frac{\text{PDA cycles}}{\text{mg/mL nanorod solution}} = \frac{5}{0.4} = \frac{15}{1.2}$ .

### c. Synergy of PDA and CdSe@CdS core-shell nanorods

In Figure 36A the data are summarized in order to compare synergistic effects of PDA and the NR. The PDA coated NR show a significantly higher photocurrent, which is approximately additive. The half-life and thus the stability of the NR is also increased significantly through coating with PDA, which is in accordance with the photoprotective properties of PDA. Additional characterization of the short NR (Figure 31) via SPM leads to the result, that also the length has a significant influence on the photoelectric properties (Figure 36B). The short NR tend to have a lower photocurrent but are slightly more stable (higher half-life) than the longer nanorods.



Considering the harsh irradiation conditions, the excess of destabilized electron holes generated cannot be quenched completely by PDA and are thus causing more oxidation/degradation of the NR. This behavior might be different for more practical irradiation conditions (lower light power).

Due to the effective spatial separation of electron/electron hole in the long NR, less photoluminescence occurs and more electrons tend to flow into the electrode (higher positive photocurrent). The recombination of an exciton (more likely for short nanorods) does not increase the degradation of the NR, but a higher rate of electrons flowing into the electrode does (more likely for long NR  $\rightarrow$  higher positive photocurrent). It was already shown that the length of the NR has an influence on the spatial separation of electron and hole<sup>[45][44]</sup> and therefore on the stability of the system. This is supported by the sweeping potential measurement (SPM) data in Figure 36B.

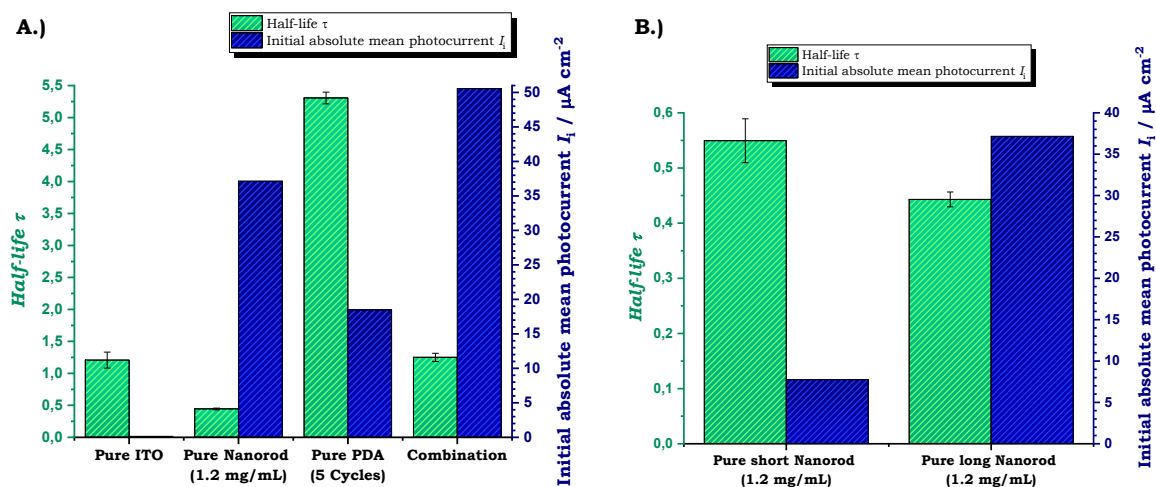


**Figure 36. A.)** Comparison of photoelectric properties (photocurrent and half-life) between pure ITO, pure nanorods (1.2 mg/mL), pure 5 cycle PDA film and a combined film. **B.)** Comparison of photoelectric properties between long [(46 ± 4) × (5.2 ± 0.6) nm] and short nanorods: [(13 ± 1) × (3 ± 0.4) nm].

After irradiating the nanorods (quasi type II class, see chapter V.3.2. *Nanocrystals as compound semiconductors (CdSe@CdS)*), the electron is delocalized in the conduction band of CdSe/CdS, while the electron hole is localized in the CdSe core. The exciton recombination would lead to luminescence with a quantum yield of 30.7 % (see Figure 37 for uncoated/bare nanorods). Since SPM data show only a positive photocurrent (see X. Appendix Figure 87 and Figure 98), large amounts of the electrons are flowing into the electrode, leaving behind a destabilized electron hole, which cannot be quenched for the bare nanorods. This electron hole might cause oxidation of cadmium and the nanorods start to degrade. A PDA coating leads to several improvements in the system based on the stabilization of the electron holes as well as of the electron.

For PDA coated nanoparticles the quantum yield decreases to 0.1 % (see Figure 37). This means that the electron/hole charge separation is improved by PDA. The electron at this point has multiple paths. Either delocalization in PDA or flowing into the electrode might be possible or (most importantly) it might be used to reduce protons if a catalyst is attached on the PDA. Which path is preferred depends now on the driving forces while it is delocalized in PDA. If the chemical driving force (fast electron transfer to the catalyst) predominates the electrostatic driving force (originating from the electrode), catalytic processes as proton reduction are feasible.

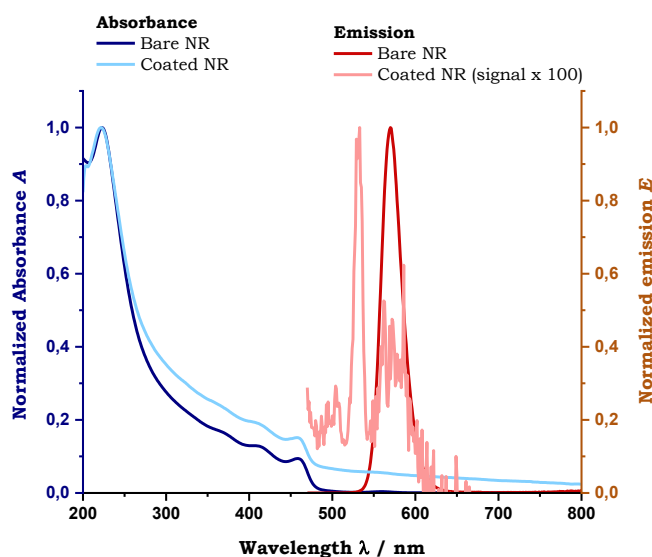


**Figure 37.** Photoluminescence of pure CdSe@CdS core-shell nanorods (quantum yield: 30.7 %) compared to PDA coated nanorod particles (quantum yield: 0.1 %). The measurements were performed by the Wächter group (Dr. Mathias Micheel) at Leibniz-IPHT for PDA coated nanorod particles.

In order to understand the nature of the generated electron/electron hole in CdSe@CdS core-shell nanorods, transient absorption spectroscopy (TAS) was performed on PDA coated nanorod particles (Figure 38). The recorded TAS data reveal complex electron/hole mechanistic. The differential absorbance  $\Delta A$  was measured for the coated nanorods over a wavelength range from 600 nm to 380 nm and the characteristic CdS and CdSe peaks are visible at 460 nm and 560 nm (Figure 38A). Additionally, the normalized  $\Delta A$  was measured separately at 460 nm (CdS) and 560 nm (CdSe) against a delay time approaching 1000 ps (Figure 38B). As mentioned prior in chapter V.3.2. *Nanocrystals as compound semiconductors (CdSe@CdS)* due to the unique band structure of CdSe@CdS core-shell nanorods, irradiation leads to the electron hole being localized in the valence band of CdSe, leading to a localization in the core. The electron is localized in the conduction band of CdS as well as CdSe since the energy difference of those bands is very small. Therefore, the electron is delocalized throughout the whole nanorod. The detected ground state bleaching shows (in terms of the transmission signal before and after the irradiation pulse) how fast the electron is falling back into the valence band. The uncoated nanorods show bleach recovery only up to  $\sim 50\%$  after 1000 ps (Figure 38B), while the coated nanorods tend to recover faster and almost completely after 1000 ps (Figure 38A+B). This result can be confirmed for the CdSe as well as for the CdS signals, indicating that on the one hand PDA shows characteristics of a hole scavenger (recovery of CdSe signal) and on the other hand it is able to stabilize the electron in the conduction band of CdSe@CdS (recovery of both CdS and CdSe signals). Consequently, this leads to a charge carrier spatial separation throughout the whole system, which is useful for the aimed hydrogen production cell. Nevertheless, regarding our desired system, these results from TAS only clearly prove that the electron is being removed from the conduction band successfully by the PDA coating. Since the electron is not used for any reduction, it can be only assumed that it is either recombining radiationless or flows into the WE electrode leading to a positive photocurrent, which was measured in SPM. The next step would be to attach and try out different catalysts to see whether the chemical driving force (electron transfer to catalyst) or the electrostatic driving force (electron flowing into the electrode) predominates.



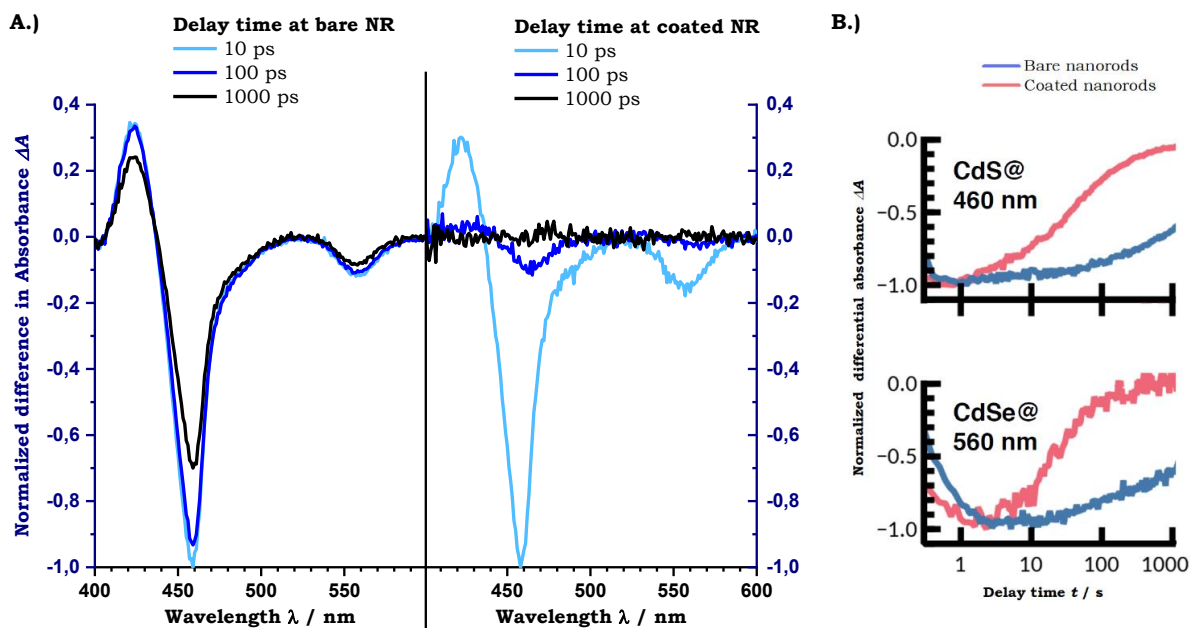


**Figure 38.** Transient absorption spectroscopy (TAS) data. **A.)** Differential Absorbance  $\Delta A$  of PDA coated CdSe@CdS nanorods in the wavelength range of 380 – 600 nm for different delay times (10 ps: light blue, 100 ps: blue, 1000 ps: dark blue). **B.)** Normalized  $\Delta A$  for single CdS (at 460 nm) and CdSe (at 560 nm) peaks of PDA coated and pure nanorods plotted against the delay time (approaching 1000 ps). TAS was performed by the Wächtler group (Dr. Mathias Micheel) at the Leibniz-IPHT.

### VII.3.2. Constant potential measurement (CPM)

Beside long-term stability studies, the SPM method was also performed in order to find a specific potential, where the most negative current is being produced. Unfortunately, the films undergo degradation upon potential sweep (probably in the positive potential range) and it was therefore not possible to certainly find the specific potential where the highest current was produced. Still a trend was observable, which needed further investigation with the constant potential measurement (CPM) method. CPM at positive potentials was performed on a 5 cycle PDA film to confirm the instability of PDA in positive potentials upon irradiation. CPM at negative potential was also performed on 5 cycle PDA films to find the most effective potential to produce photocurrent. The negative potential measurements were additionally performed on pure nanorods (0.8 mg/mL spin coated solution) and combined films (5 cycles PDA + 0.8 mg/mL spin coated nanorods solution). After the optimized potential was found, additional hole scavengers were included and the response of the system regarding to the photocurrent was recorded via CPM at constant ionic strength of the electrolyte. Data processing for the recorded CPM raw data is shown exemplary for a pure 5 cycle PDA film in Figure 39. Since the lamp was turned on/off for specific time intervals, the recorded CPM raw data also show steps for the lamp-on times (Figure 39A). The lamp-off curve was interpolated (Figure 39B) and subtracted from the lamp-on curve (Figure 39C). The resulting function was integrated and led to the lamp-on photocurrent  $I_{on}$  (Figure 39D). Additionally, the lamp-on curves were fitted exponentially with equation (6) to determine the asymptote (see Figure 40). The asymptote is a useful tool to see the magnitude of the photocurrent after it reached an equilibrated state. If the equilibrium was not reached after 2000 s, the last lamp-on value was taken into consideration and was marked (\*) accordingly.

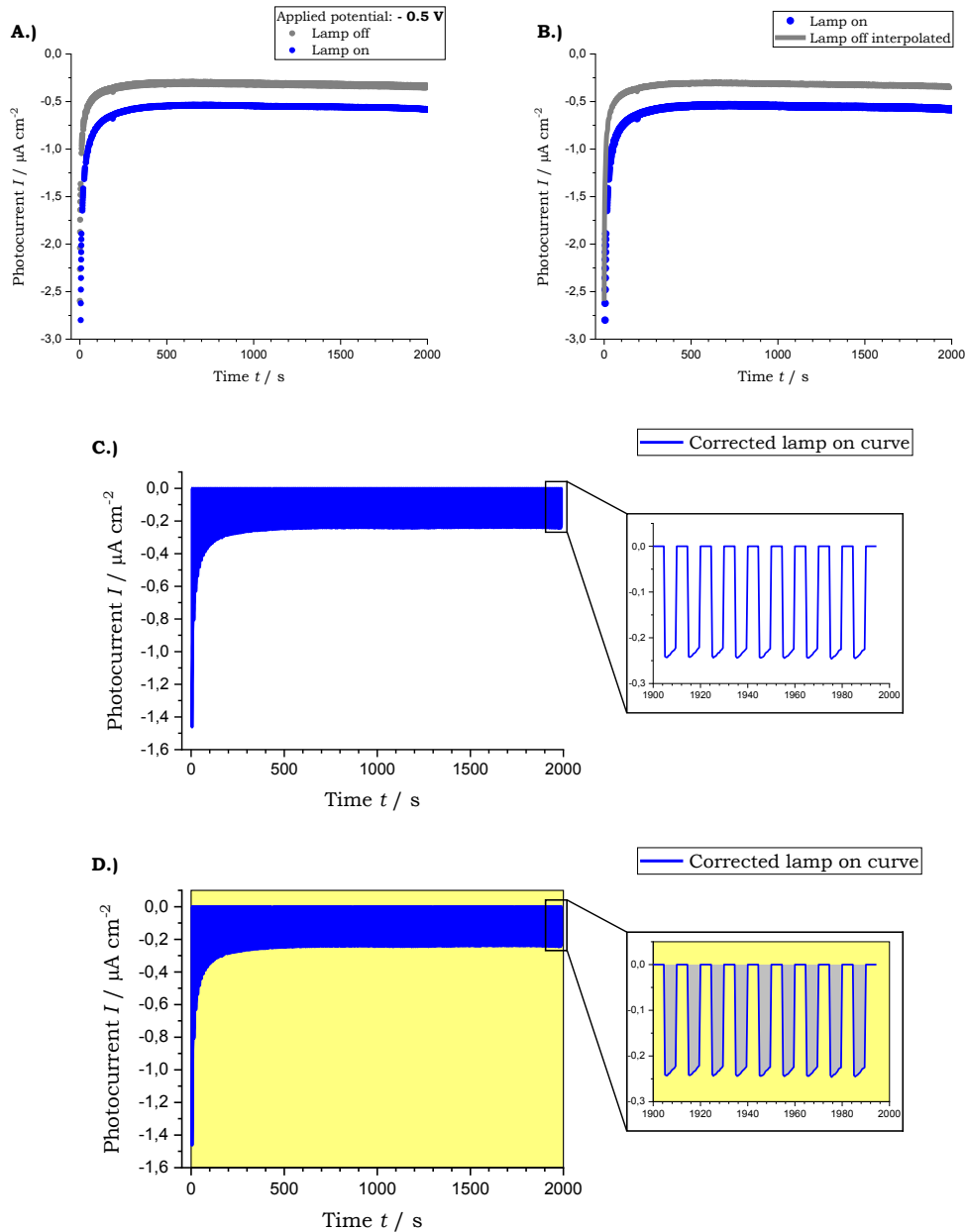


**Figure 39.** Data processing for the constant potential measurement (CPM). **A.)** Raw Data. Current curves for the lamp on/off times. **B.)** Interpolated lamp-off curve (Baseline). **C.)** Subtracted Baseline leads to the actual lamp on photocurrent curve  $I$ . **D.)** Integration finally leads to the actual photocurrent as  $\mu\text{A} \cdot \text{cm}^{-2} \cdot \text{s}$ . Grey highlighted is the corresponding area.

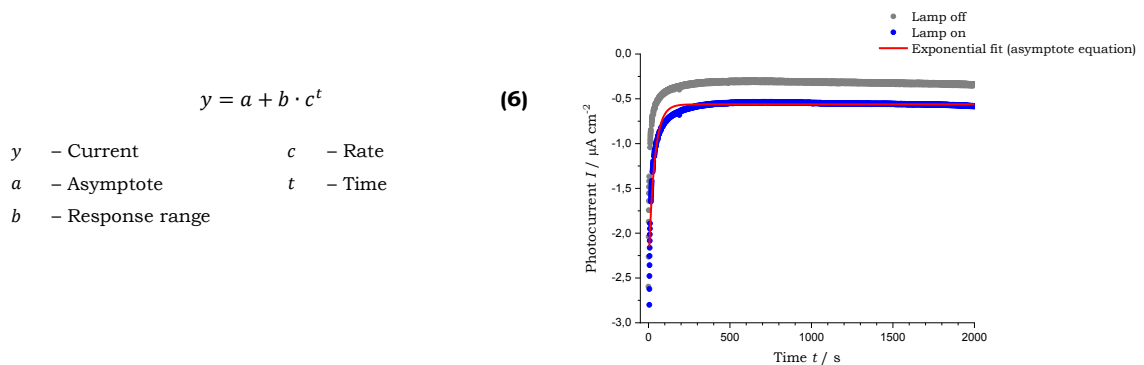


**Figure 40.** Applied asymptote fit equation (6) on the lamp on curve.

### a. Pure PDA at positive potentials

Throughout the SPM it was always the oxidative peaks, which drop off more strongly, indicating a change of chemical nature while sweeping into positive potentials. Probably, the resulting quinone groups (which are formed at positive potentials) are attacked by intra-/intermolecular nucleophiles, which destroyed their switchable redox and optoelectronic properties. Therefore, CMP was performed on 5 cycle PDA films at +0.1 V, +0.2 V, +0.3 V, +0.4 V and +0.5 V and the data are shown in Figure 41.

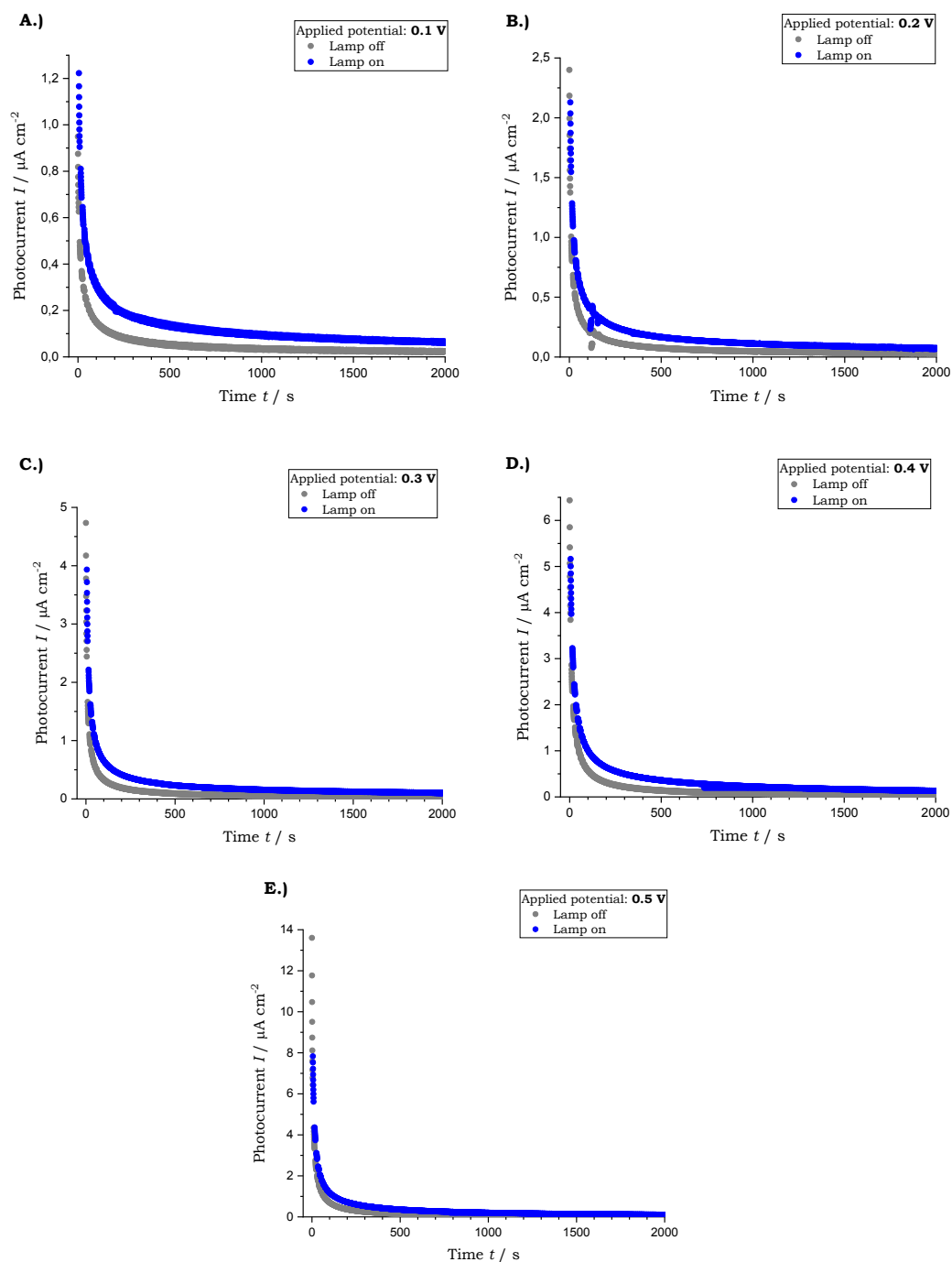


**Figure 41.** Constant potential  $U$  photocurrent measurements (CPM) + 0.1 V  $\leq U \leq$  + 0.5 V at 5 cycle PDA films for 2000 seconds. Blue curves indicate lamp-on times, while grey curves indicate lamp-off times. **A.)** 0.1 V applied potential.

**B.)** 0.2 V applied potential. **C.)** 0.3 V applied potential. **D.)** 0.4 V applied potential. **E.)** 0.5 V applied potential.

The calculated lamp-on photocurrent  $I_{on}$  and the lamp-on asymptote  $A_{on}$  are summarized in Figure 42. The main difference to the following negative potential series is that the current for positive potentials is also positive. This means that released electrons are flowing into the WE. Applying higher potentials leads to higher initial currents but then the current is decreasing even stronger right at the beginning. After 2000 seconds the current dropped to a small fraction compared to the initial one. This is shown especially in Figure 41E (+ 0.5 V). The current in Figure 41E (+ 0.5 V) is dropping from  $13.6 \mu\text{A cm}^{-2}$  to  $\sim 0.25 \mu\text{A cm}^{-2}$ . In the first 5 seconds without irradiation, the current drops from  $13.6 \mu\text{A cm}^{-2}$  to  $6.4 \mu\text{A cm}^{-2}$ , a total decrease of 53 %. Turning the light on thus causes an increase by only 22 % up to  $7.8 \mu\text{A cm}^{-2}$ .

By decreasing the applied potential to + 0.1 V (Figure 41A), the influence of the potential is of course decreased and thus the expected degradation is reduced. Indeed, the current in the first 5 seconds right at the beginning is dropping only by 34 % ( $0.95 \rightarrow 0.62 \mu\text{A cm}^{-2}$ ) and increased by 94 % ( $0.62 \rightarrow 1.22 \mu\text{A cm}^{-2}$ ) upon irradiation. Independent from the initial current, the currents for all applied potentials in Figure 41 drop to the same order of magnitude, which is shown in Figure 42 by the lamp on Asymptote  $A_{on}$  and indicates a degradation over time. This is an interesting result on the stability of PDA and affirm that PDA is not suitable to be used at positive potentials for photocatalytic oxidation, such as oxygen generation.

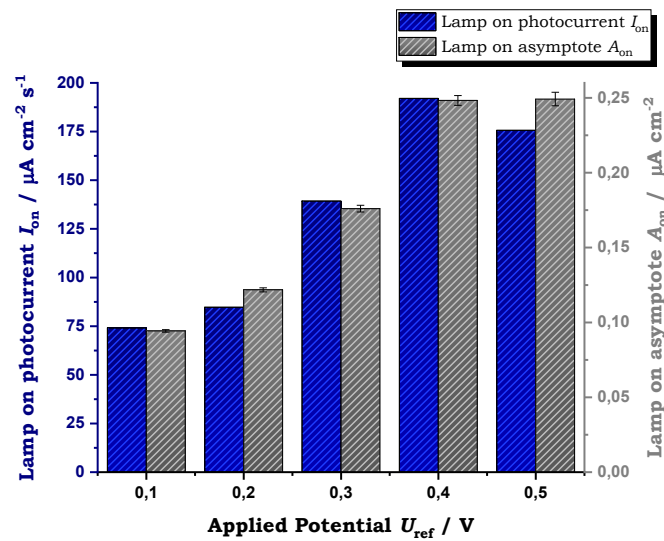


**Figure 42.** Summarized results of the lamp-on photocurrent  $I_{on}$  and the lamp-on asymptote  $A_{on}$  by constant potential  $U$  photocurrent measurements (CPM) at  $+ 0.1 \text{ V} \leq U \leq + 0.5 \text{ V}$  of a 5 cycle PDA film.

### b. Pure PDA at negative potentials

More interesting is of course the negative potential range since hydrogen production is occurring in that range and PDA shows a negative current (favoring reduction reactions such as proton reduction). The applied potential was held constant at  $-0.5 \leq U \leq \text{OCP}$  upon irradiation (see Figure 43).

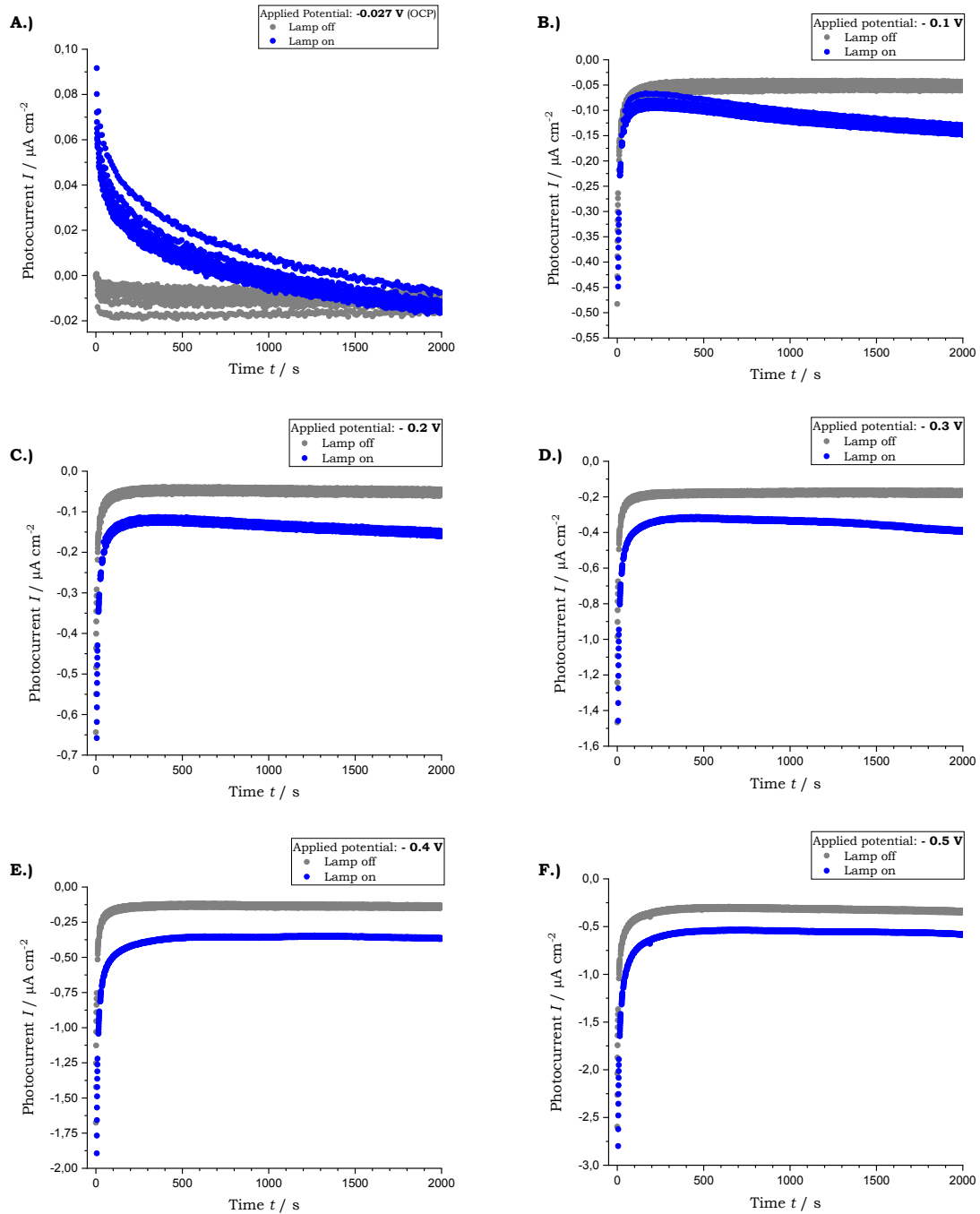


**Figure 43.** Constant potential  $U$  photocurrent measurements (CPM)  $\text{OCP} \leq U \leq -0.5 \text{ V}$  of 5 cycle PDA films for 2000 seconds. Blue curves indicate lamp-on times, while grey curves indicate lamp-off times. **A.)**  $-0.027 \text{ V}$  (OCP) applied potential. **B.)**  $0.1 \text{ V}$  applied potential. **C.)**  $0.2 \text{ V}$  applied potential. **D.)**  $0.3 \text{ V}$  applied potential. **E.)**  $0.4 \text{ V}$  applied potential. **F.)**  $0.5 \text{ V}$  applied potential.

The OCP is the so-called *open circuit potential*. At this potential there should be (theoretically) no current flowing and is very close to 0 V. And indeed, at the OCP only current is measured for the lamp-on times, which is extremely low and positive. This proves again that the potential has a significant influence on the detected currents. Without any applied potential PDA exhibits no significant optoelectronic signal. The CPM curve for the OCP is shown in Figure 43A, but was disregarded for the comparison in Figure 44 since it is not suitable for hydrogen production.

The photocurrents detected at more negative potentials are revealing a promising result (Figure 43B – F). In contrast to the positive potential CPM curves, the current is not only negative but also increasing over time. Instead of degradation, such as at positive potentials, an equilibrium is reached. Especially the curve at  $-0.1$  V (Figure 43B) is showing that the photocurrent is increasing with time. Decreasing the potential even further shows that the system is reaching at some point an equilibrium. This equilibrium is fully adjusted for  $-0.4$  V and  $-0.5$  V (Figure 43E and F) within approximately 1000 seconds. Again, the lamp-off current is, as expected, also decreasing while decreasing the potential further.

Regarding to the calculated lamp-on photocurrent  $I_{on}$  and the lamp-on asymptote  $A_{on}$  in Figure 44,  $-0.5$  V seems to be the optimized potential. Decreasing the potential even beyond  $-0.5$  V would probably decrease the lamp-on asymptote even more, but would not have much impact on the lamp-on current since there is already not a big different between  $-0.4$  V and  $-0.5$  V. Instead, only the asymptotes would decrease further and the lamp-on/lamp-off asymptotes would come even closer as it is already seen for  $-0.4$  V and  $-0.5$  V in Figure 43E and F. Decreasing the potential even further would therefore only predominate the electrochemical over the photochemical driving force, which is not desired for the envisioned system.

If the CPM measurements were performed for longer than 2000 seconds, even higher potentials such as  $-0.3$  V would probably be suitable because the equilibrium would probably establish for longer irradiation times.

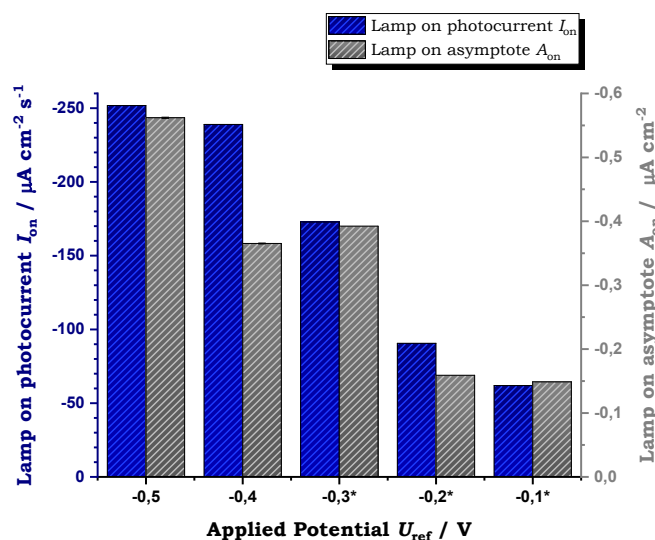


**Figure 44.** Summarized results of the lamp-on photocurrent  $I_{on}$  and the lamp-on asymptote  $A_{on}$  by constant potential  $U$  photocurrent measurements at  $-0.1 \text{ V} \leq U \leq -0.5 \text{ V}$  of a 5 cycle PDA film.

Depending on that, either  $-0.4$  V or  $-0.5$  V can be used for further investigations. The exhibited negative currents for PDA indicate that PDA is consuming electrons from the WE. Adding hole scavenger (electron donor) to the system should hence increase the negative current towards positive currents because the hole scavenger is now delivering electrons to the system instead of the WE. This behavior was investigated for different hole scavengers like ascorbic acid, sodium ascorbate, sodium sulfite and methanol. The measured CPM curves are shown in Figure 45 and the calculated results on the lamp-on photocurrent and lamp-on asymptote are summarized in Figure 46.

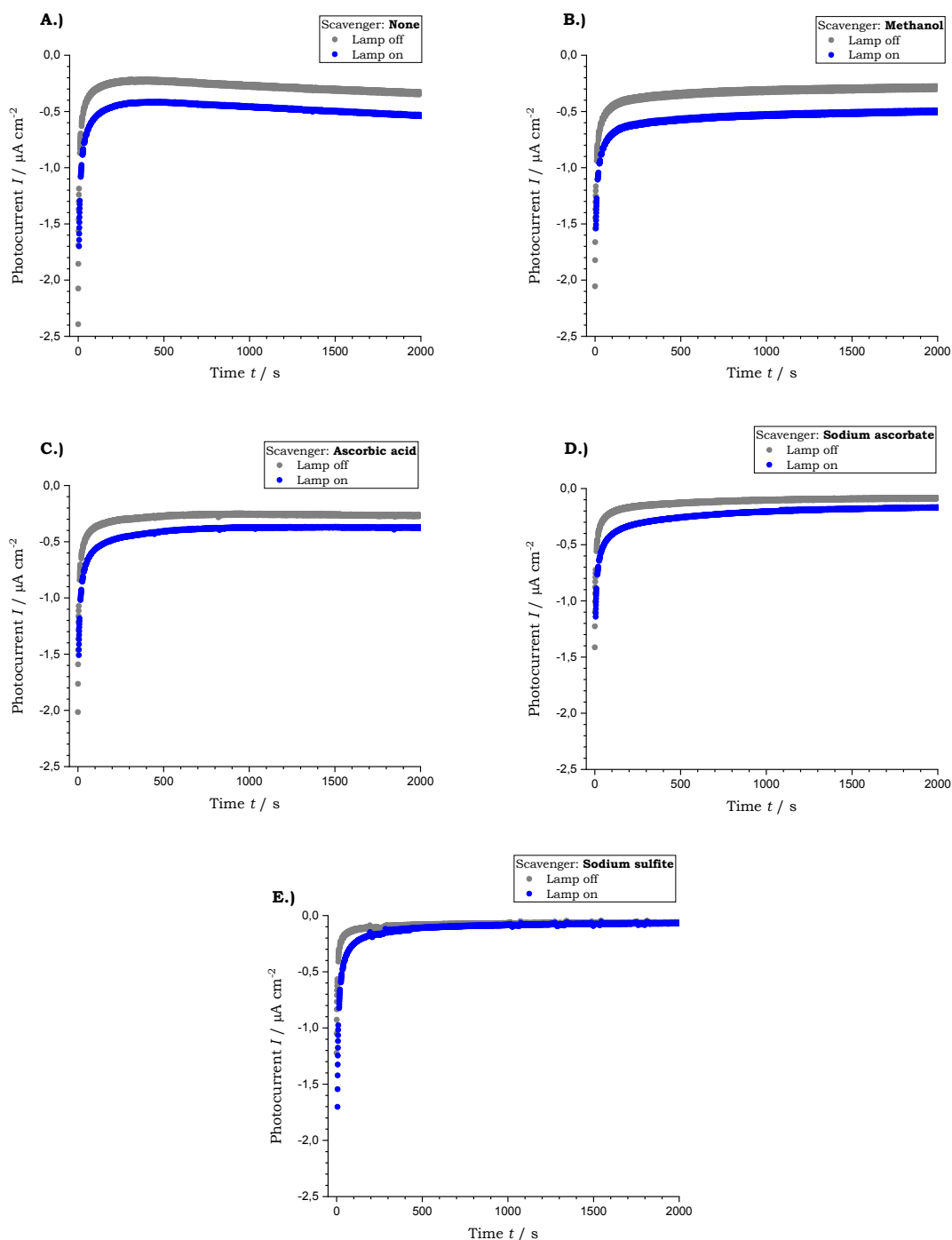


**Figure 45.** Constant potential photocurrent measurements (CPM) at  $-0.5$  V of 5 cycle PDA films for 2000 seconds with a hole scavenger. **A.)** No hole scavenger. **B.)** Methanol. **C.)** Ascorbic acid. **D.)** Sodium ascorbate. **E.)** Sodium sulfite.

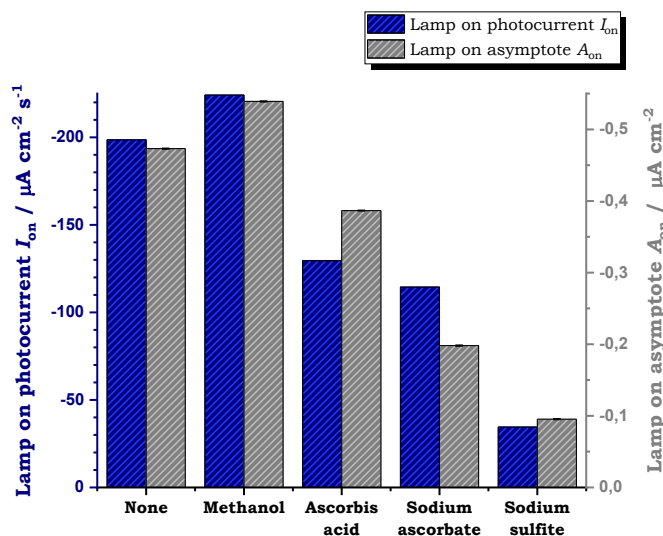


**Figure 46.** Summarized results of the lamp-on photocurrent  $I_{on}$  and the lamp-on asymptote  $A_{on}$  for different hole scavengers (methanol, ascorbic acid, sodium ascorbate, sodium sulfite) collected by constant potential photocurrent measurements at  $-0.5$  V of a 5 cycle PDA film.

Ascorbic acid, sodium ascorbate and sodium sulfite indeed increase, as expected, the current towards positive potentials but methanol as a hole scavenger does not follow this trend. Methanol instead decreases the lamp-on photocurrent and the lamp-on asymptote even further towards negative currents. The WE is delivering now even more electrons to the system, which is a confusing result.

Regarding the response of PDA to hole scavengers (decrease of photocurrent) and the fact, that generally negative currents are produced (at negative potential), is in accordance with characteristics for p-type semiconducting materials.

The opposite behavior for methanol is disregarded for now and will be discussed later on, after the results of pure nanorods and combines films were presented.



### c. Pure nanorods at negative potential

The same CPM series was also performed on the pure CdSe@CdS nanorods. As n-type semiconductors, the nanorods should exhibit a positive photocurrent, which was already observed by the collected SPM data. The CPM curves are shown in Figure 47 and the lamp-on photocurrents and asymptotes are summarized in Figure 48.

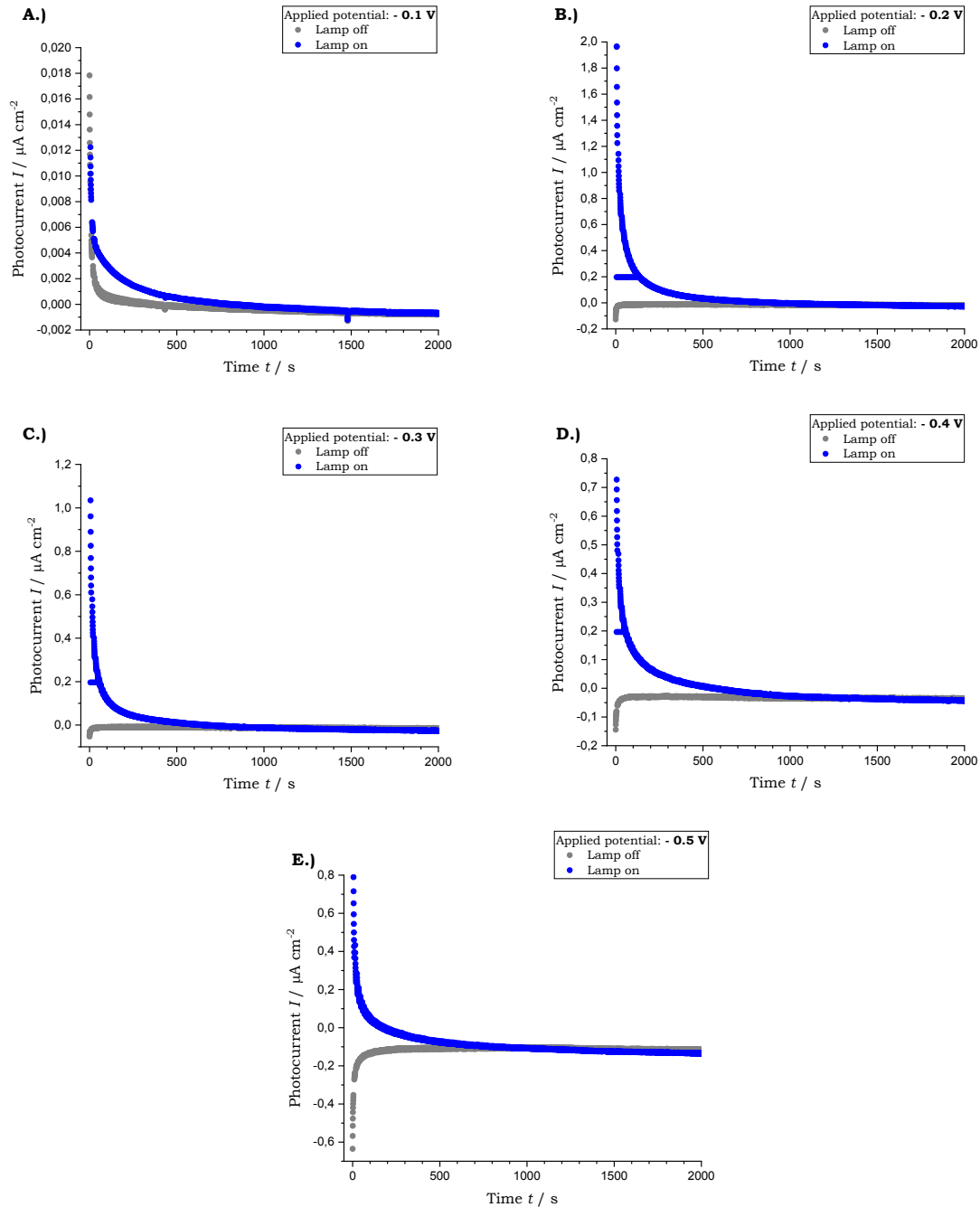


**Figure 47.** Constant potential  $U$  photocurrent measurements (CPM) –  $0.1 \text{ V} \geq U \geq -0.5 \text{ V}$  at spin coated nanorod films (0.8 mg/mL) for 2000 seconds. Blue curves indicate lamp-on times, while grey curves indicate lamp-off times. **A.)** 0.1 V applied potential. **B.)** 0.2 V applied potential. **C.)** 0.3 V applied potential. **D.)** 0.4 V applied potential. **E.)** 0.5 V applied potential.

Interestingly the lamp-on photocurrent does not follow a particular trend while decreasing the potential from  $-0.1$  V to  $-0.5$  V. The lamp-on asymptote on the other hand does decrease with an increasing potential. While the asymptote is positive at the beginning, it is pushed into negative currents approaching  $-0.5$  V, where the highest negative asymptote was detected.

These results, especially the lamp-on photocurrent, should be considered with caution because there is definitely a more complex mechanism related to the recorded data. Generally, positive currents should be observed for n-type semiconductors because they deliver electrons to the WE (into the circuit). But right at the beginning negative currents are also detected when the light is turned off. And while increasing the potential, not only the lamp-on asymptote, but also the lamp-off asymptote is pushed into negative values. Maybe the pure nanorods are just too fragile without any support of any hole scavenger (e.g. PDA). It might be possible that while they are irradiated, they release electrons (typical positive currents) but when the light is turned off, the generated holes might be filled up by the circuit. Hence, electrons are consumed from the WE leading to a negative current. This is supported by the fact that the negative current is higher, the more negative the potential is. The increased negative charge on the electrode surface is more likely to quench the generated holes (see illustration in Figure 16 for negative potentials). To investigate this further, different hole scavengers were added while performing CPM.

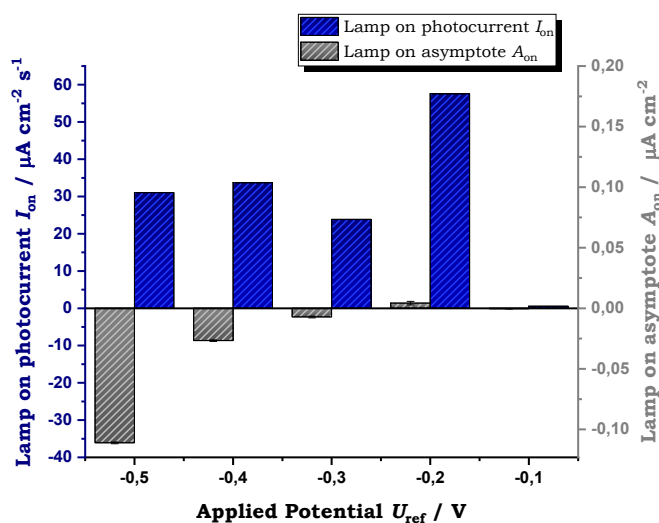


**Figure 48.** Summarized results of the lamp-on photocurrent  $I_{on}$  and the lamp-on asymptote  $A_{on}$  by constant potential  $U$  photocurrent measurements at  $-0.1$  V  $\leq U \leq -0.5$  V of pure nanorods films (0.8 mg/mL spin coated).

Just like in the previous chapter  $-0.5$  V was taken at constant ionic strength of the electrolyte to compare the same hole scavengers as before, namely ascorbic acid, sodium ascorbate, sodium sulfite and methanol. CPM curves are shown in Figure 49.

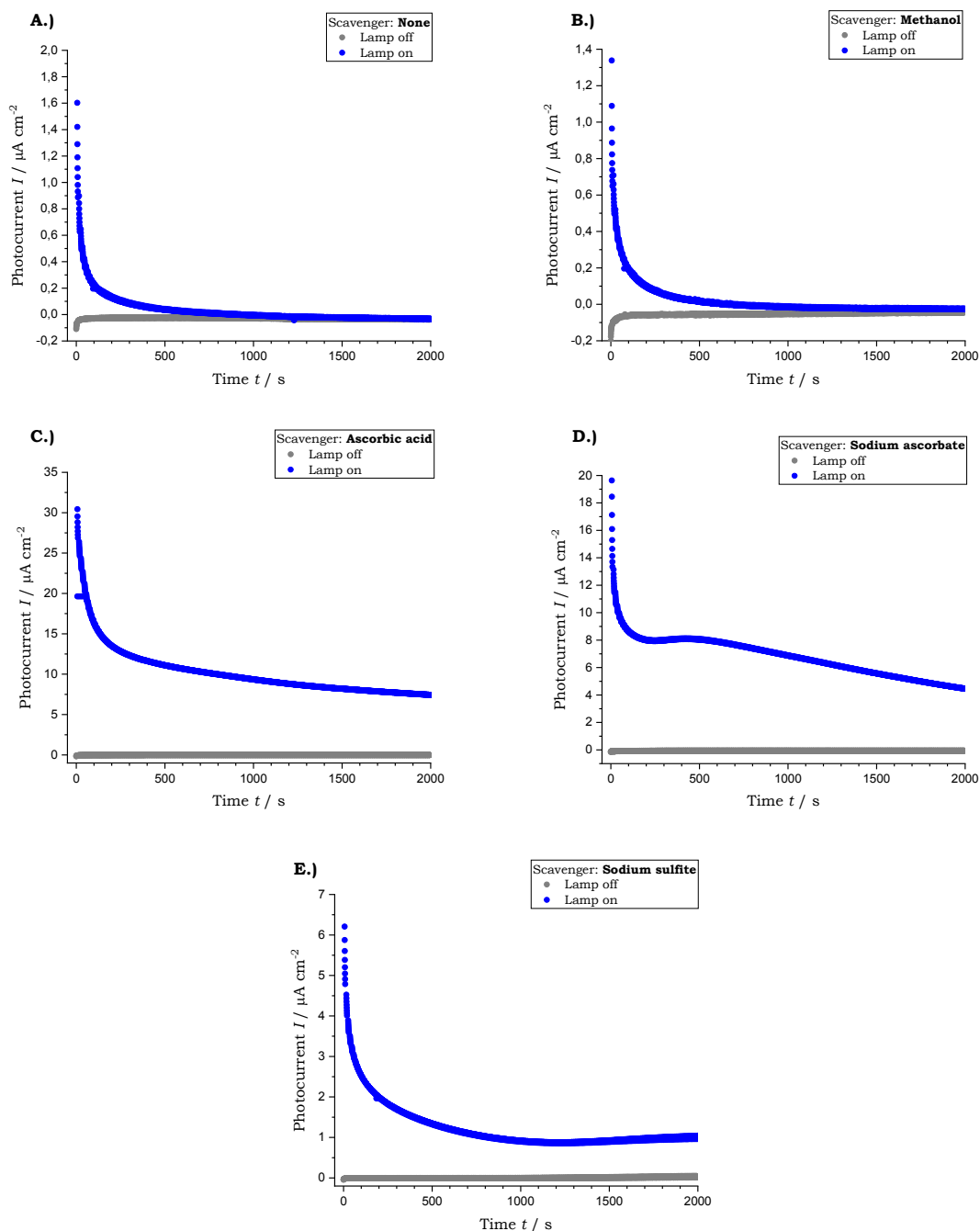


**Figure 49.** Constant potential  $U$  photocurrent measurements (CPM) at  $-0.5$  V of pure nanorod films (0.8 mg/mL spin coated) for 2000 seconds with additional hole scavenger. **A.)** No hole scavenger. **B.)** Methanol. **C.)** Ascorbic acid. **D.)** Sodium ascorbate. **E.)** Sodium sulfite.

As mentioned before, the measured positive photocurrents in Figure 48 mean that electrons are flowing into the WE and leave behind an electron hole in the nanorods. Therefore, these positive currents should increase further while adding hole scavengers because the holes are quenched and the recovered nanorods can release even more electrons. The results are remarkable (see Figure 50).

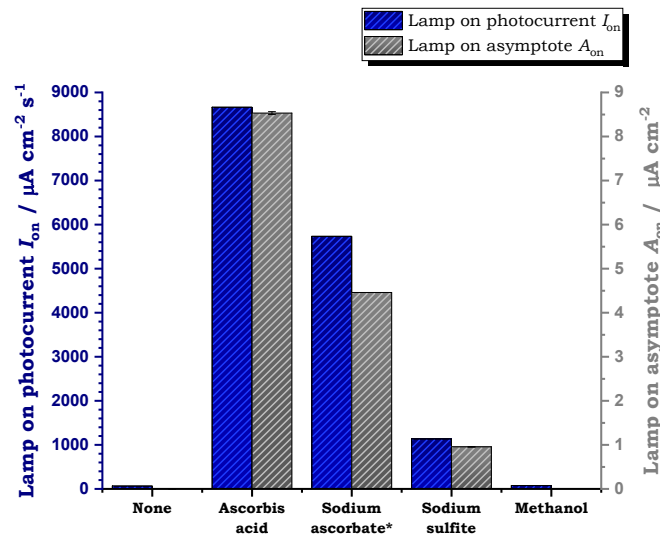


**Figure 50.** Summarized results of the lamp-on photocurrent  $I_{on}$  and the lamp-on asymptote  $A_{on}$  for different hole scavengers (methanol, ascorbic acid, sodium ascorbate, sodium sulfite) collected by constant potential photocurrent measurements at  $-0.5$  V of pure nanorods films ( $0.8$  mg/mL spin coated).

The lamp-on photocurrents as well as the lamp-on asymptotes are increased by two orders of magnitude compared to the bare nanorods without any hole scavenger. Ascorbic acid, sodium ascorbate and sodium sulfite (in decreasing order) increase the photocurrent enormously. This indicates a good response of the nanorods to hole scavengers. Interestingly, methanol as a hole scavenger does not affect the photocurrent significantly and there is almost no difference compared to no additional hole scavenger. This result is surprising because methanol has been used in literature many times as hole scavenger even for supporting proton reduction.

The previous hypothesis that the holes in the nanorods are quenched and produce negative currents is also supported by these results. The initial lamp-off datapoint without a hole scavenger is at  $-0.11 \mu\text{A cm}^{-2}$  and the corresponding initial lamp-on datapoint is at  $1.6 \mu\text{A cm}^{-2}$ . The general assumption is that more negative photocurrent is released, the more holes are generated because the holes need to be quenched by the WE. Therefore, the initial negative current (when the lamp is turned off) must always be considered regarding to the initial positive current (when the lamp is turned on). This reveals that for no hole scavenger the positive-to-negative current ratio lies at  $\frac{1.6}{|-0.11|} = 14.5$ . Accordingly, hole scavengers should exhibit a higher ratio and this is indeed the case. The following table summarizes the initial lamp on/off currents as well as the corresponding ratio and supports the hypothesis that the negative current originates from the hole quenched in the nanorods. The trend in Table 3 reflects the trend in Figure 50. Again, only methanol is not following the expected trend.

**Table 3.** Summary of the initial lamp-on, initial lamp-off and ratio of lamp-on/off currents of the hole scavenger.

| Hole scavenger   | Initial on current / $\mu\text{A cm}^{-2}$ | Initial off current / $\mu\text{A cm}^{-2}$ | On/off current ratio |
|------------------|--------------------------------------------|---------------------------------------------|----------------------|
| None             | -0.11                                      | 1.6                                         | 14.5                 |
| Sodium sulfite   | -0.05                                      | 6.2                                         | 124                  |
| Sodium ascorbate | -0.15                                      | 19.7                                        | 131                  |
| Ascorbic acid    | -0.17                                      | 30.4                                        | 178                  |
| Methanol         | -0.20                                      | 1.45                                        | 7.3                  |

#### d. PDA/nanorods at negative Potential

Finally, the combined PDA/NR films were investigated by CPM. PDA and the NR showed opposite behavior in the previous CPM series. While the NR exhibit a positive current (typical for n-type semiconductors) and is supported by additional hole scavengers (except for methanol), PDA exhibits a negative current (p-type semiconducting behavior) and is weakened by additional hole scavengers (except for methanol). Hence, complex results are expected for the combined film. The CPM curves are shown in Figure 51A-E. The lamp-on currents and asymptotes are summarized in Figure 52.

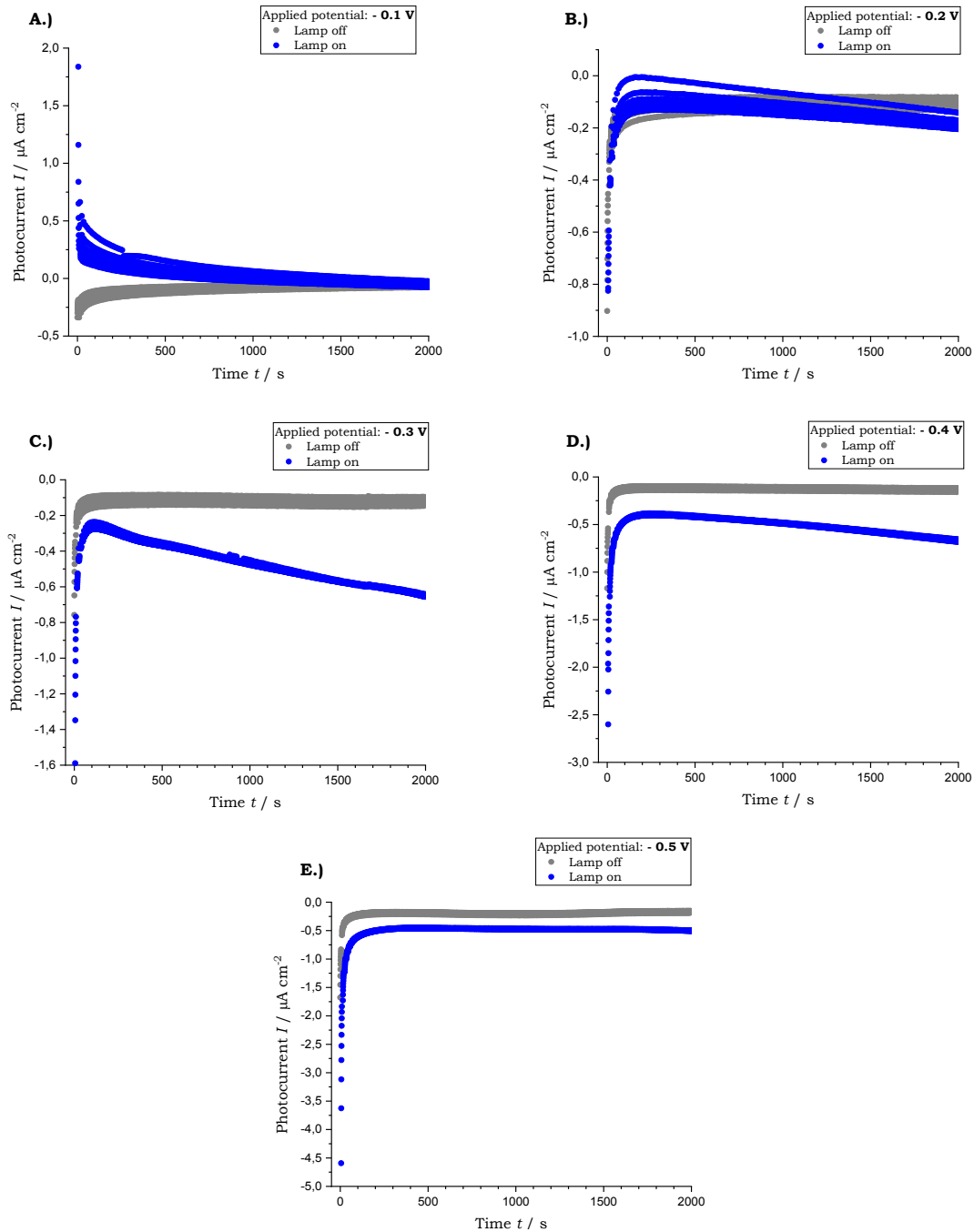


**Figure 51.** Constant potential  $U$  photocurrent measurements (CPM) –  $0.1 \text{ V} \geq U \geq -0.5 \text{ V}$  of combined films (5 cycles PDA + 0.8 mg/mL spin coated nanorods) for 2000 seconds. Blue curve indicated lamp-on times, while grey curve indicated lamp-off times. **A.)** 0.1 V applied potential. **B.)** 0.2 V applied potential. **C.)** 0.3 V applied potential. **D.)** 0.4 V applied potential. **E.)** 0.5 V applied potential.

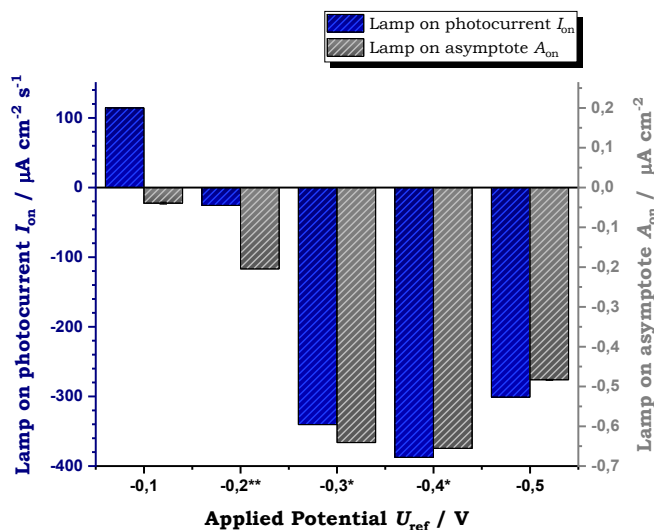


**Figure 52.** Summarized results of the lamp-on photocurrent  $I_{on}$  and the lamp-on asymptote  $A_{on}$  by constant potential  $U$  photocurrent measurements at  $-0.1 \text{ V} \leq U \leq -0.5 \text{ V}$  of combined films (5 cycles PDA + 0.8 mg/mL spin coated nanorods).

The CPM data show an overlay of both, pure PDA and pure nanorods. While the lamp-on photocurrent at  $-0.1 \text{ V}$  in Figure 51A is positive ( $\rightarrow$  nanorods behavior, see Figure 47), the sign flips approaching  $-0.5 \text{ V}$  in Figure 51D ( $\rightarrow$  PDA behavior, see Figure 43). The turnover point is clearly visible in the CPM plot for an applied potential of  $-0.2 \text{ V}$  (Figure 51B). Unlike PDA, an equilibrium is not reached until  $-0.5 \text{ V}$ , probably due to interference of the nanorods. The CPM series with additional hole scavengers in the combined films was therefore also performed at a potential of  $-0.5 \text{ V}$ .

Just like in the previous measurements an overlay of pure PDA and pure nanorod characteristics are observable for the hole scavenger series. The lamp-on/off curves for the different hole scavengers are shown in Figure 53, while the results on the lamp-on photocurrent and lamp-on asymptote are summarized in Figure 54.

\* final lamp-on current value instead of asymptote

\*\* turn over from positive to negative currents

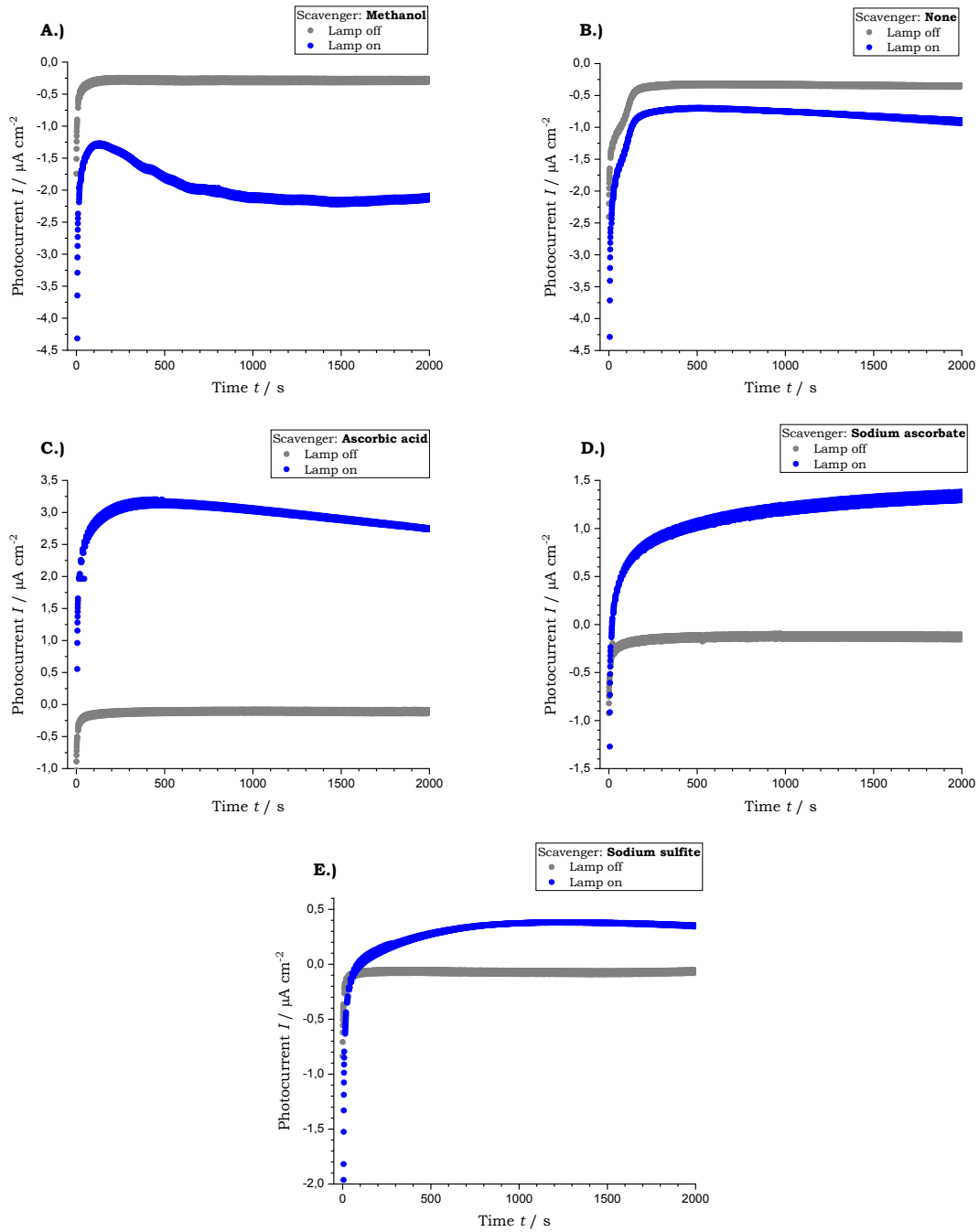


**Figure 53.** Constant potential U photocurrent measurements (CPM) at  $-0.5$  V of combined films (5 cycles PDA +  $0.8$  mg/mL spin coated nanorods) for 2000 seconds with additional hole scavenger. **A.)** No hole scavenger. **B.)** Methanol. **C.)** Ascorbic acid. **D.)** Sodium ascorbate. **E.)** Sodium sulfite.

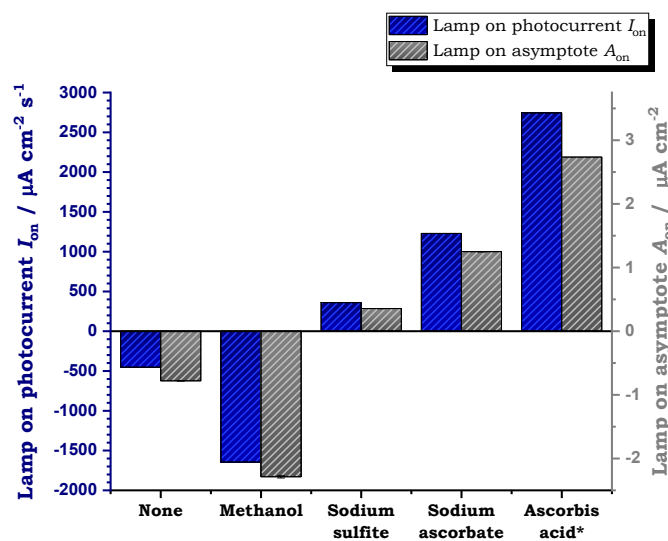


**Figure 54.** Summarized results of the lamp-on photocurrent  $I_{on}$  and the lamp-on asymptote  $A_{on}$  for different hole scavengers (methanol, ascorbic acid, sodium ascorbate, sodium sulfite) collected by constant potential photocurrent measurements at  $-0.5$  V of combined films (5 cycles PDA + 0.8 mg/mL spin coated nanorods).

The combined film with no additional hole scavenger shows to be a significant improvement, compared to the single components. The lamp-on photocurrent is with  $\sim -450 \mu\text{A cm}^{-2}$  more than twice as much as for pure PDA ( $\sim -200 \mu\text{A cm}^{-2}$ ). This means that PDA is constantly removing the electrons from the conduction band of the nanorods (supported by TAS in chapter VII.3.1.c. *Synergy of PDA and CdSe@CdS core-shell nanorods*), while the holes are constantly filled by the electrode, resulting in an additional negative current. The hole quenching in the nanorods by the electrode was already observed for the pure nanorods (negative current when the lamp is turned off, see Figure 47). The more negative current for the combined film (compared to pure PDA) indicates that PDA is rather easily removing the electrons from the nanorods than from the bare electrode without nanorods and suggest a good interaction between nanorods and PDA in the combined films.

The situation is more complex when hole scavengers are introduced to the system. The hole scavengers, which have shown to support the pure nanorods (ascorbic acid, sodium ascorbate and sodium sulfite), as expected, improved the positive currents in the combined films. An additional hole scavenger should increase the capability of the nanorods to produce electrons, which flow into PDA. If PDA is saturated with electrons, the recovered nanorods donate their electrons to the electrode, which causes a positive current that is even higher the more efficient the hole scavenger is. This is be a reasonable explanation for the hole scavengers, which produced extremely high positive currents for the pure nanorods as well as for the combined films. The saturation of PDA with electrons and the photoprotective property of PDA (whereby the involvement of the nanorods in photo-driven processes is decreased) lowers the current from  $\sim 8700 \mu\text{A cm}^{-2}$  (bare nanorods) to  $\sim 2700 \mu\text{A cm}^{-2}$  for ascorbic acid as hole scavenger.

As we have seen before, methanol slightly increased the amount of negative current released in pure PDA. The addition of methanol to a combined film decreases the current even further to  $\sim -1600 \mu\text{A cm}^{-2}$ .

\* final lamp-on current value instead of asymptote



There is obviously a close interaction between PDA and methanol because instead of donating electrons to PDA, methanol is somehow increasing the capability of PDA to consume electrons.

As it was explained before, electron consumption from the nanorods is rather easier than from the electrode, whereby the negative current is even larger for the combined film with methanol compared to pure PDA with methanol.

Further understanding of the electron dynamics in the system is only possible if a suitable catalyst is attached. Ascorbic acid seems to be a very efficient hole scavenger and should therefore enhance proton reduction. If hydrogen production is rather hindered than favored by ascorbic acid, the premise of PDA saturation by electrons will be disproved and the electrons are rather flowing into the electrode than PDA. Methanol on the other hand seems to increase the capability of PDA to consume electrons. This might be also useful for hydrogen production since electrons are more favored to move into PDA than to flow into the electrode.

Nevertheless, adding new components to the system (catalyst attachment) might induce even more complex mechanistic. Therefore, the performed CPM measurements (potential and hole scavenger series) need to be repeated in a combined film composed of nanorods, PDA and catalyst (CAT) to verify the assumed electron mechanistic. Ultimately quantitative hydrogen production assisted by the NR/PDA/CAT film would complete the first impression of the current system towards catalytic efficiency.

## VII.4. Ultra-smooth ITO

### VII.4.1. General procedure and results

The characterization of ultrathin PDA films (few nanometers in thickness) on ITO via AFM is quite difficult because the commercially available ITO has a high surface roughness. A procedure was developed to produce ultra-smooth ITO, which is schematically represented in Figure 55.

Immediate ITO sputtering on ultra-smooth silicon wafer is not possible because the attractive interactions between the hydrophilic silicon wafer and ITO are too strong. Therefore, a silicon wafer is treated with oxygen plasma to generate a  $\text{SiO}_2$  layer, which can be used to functionalize the surface with a hydrophobic layer. This intermediate hydrophobic layer should decrease attractive interactions at the silicon/ITO interface and keep the interface at the same ultra-smooth. Here, we tested as intermediate layer a self-assembled monolayer (SAM) based on different kind of silanes, which are used to functionalize the Si/ $\text{SiO}_2$  surface. The SAM functionalization was performed with an alkylated silane (Trimethoxy(octadecyl)silane, **ODTMS**) and a fluorinated silane (Triethoxy(3,3,4,4,5,5,6,6,7,7,8,8,8-tridecafluorooctyl)silane, **TEFOS**) by just applying them onto the surface for 24 h. A more reactive silazane (1,1,1,3,3,3-Hexamethyldisilazane, **HMDS**) was also attached to the surface by chemical vapor deposition (Figure 56) at 120 °C since activation energy is necessary. The mechanism of SAM formation is shown in Figure 57A for the silanes and in Figure 57B for the silazane.

After SAM functionalization ITO is sputtered on the hydrophobic wafer and a glass slide with a commercially available glue (resin-based) is attached on top. The resin is hardened at 80 °C for 30 min while pressing the layers together. Theoretically, the SAM/ITO interface should be the interface with the weakest attractive interactions and stripping of the silicon wafer from the glass would lead to the desired ultra-smooth ITO surface on glass.

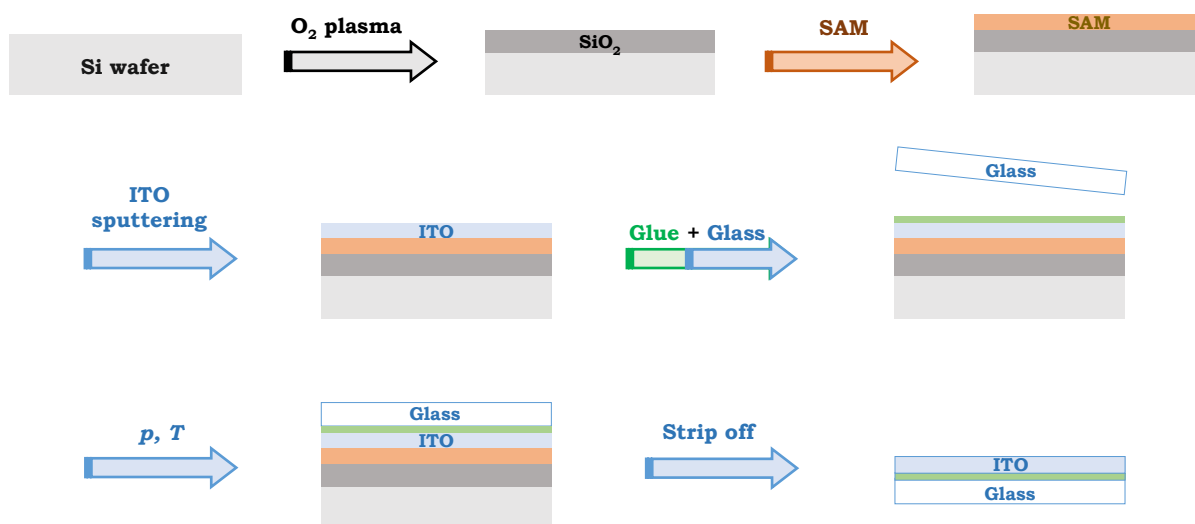


**Figure 55.** General procedure to produce ultra-smooth ITO. First, Si-wafer are oxygen plasma treated, followed by the bonding of the self assembles monolayer (SAM). ITO sputtering on the hydrophobic surface, followed by gluing glass on the surface complete the layers. Removing the wafer should separate the layers at the weakest interface (ITO/SAM) leading to ultra-smooth ITO.

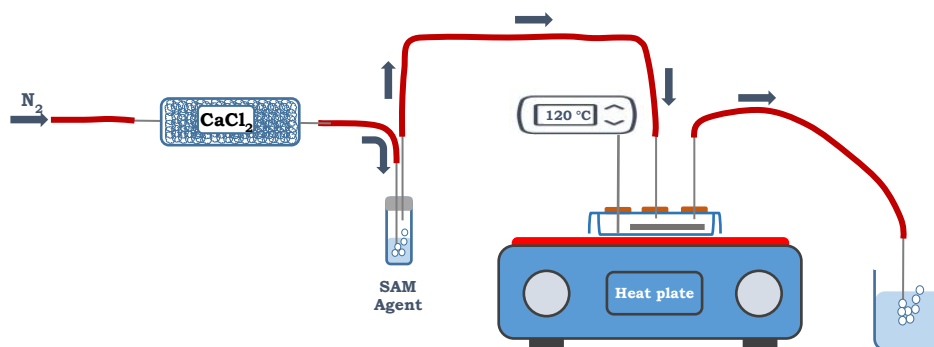


**Figure 56.** General set-up for the chemical vapor deposition of 1,1,1,3,3,3-Hexamethyldisilazane. Nitrogen is dried over a  $\text{CaCl}_2$  column and bubbles into the silazane solution. The vapor flows into a petri dish preprocessed with three holes (inlet, outlet, thermostat sensor) at  $120\text{ }^\circ\text{C}$  in which the Si-wafer is placed.

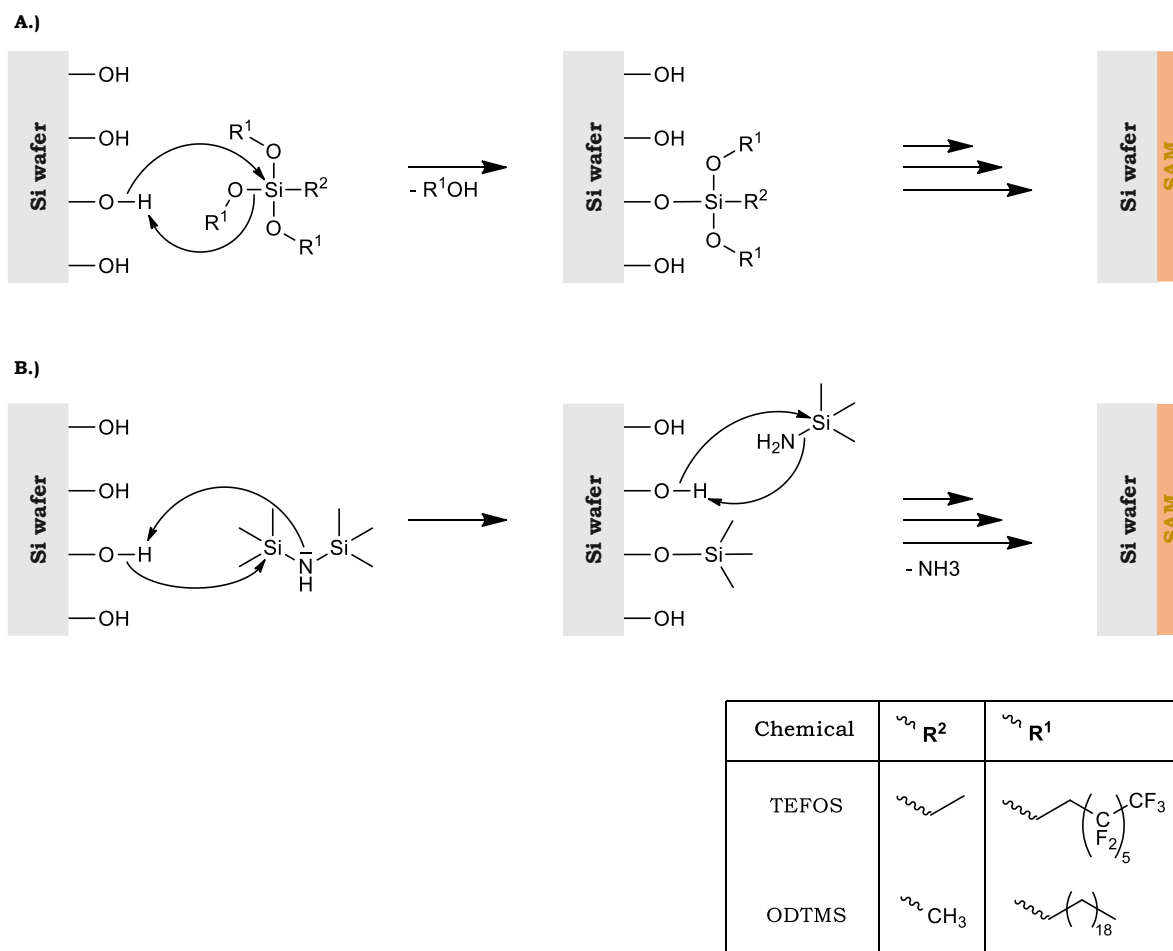


**Figure 57.** Formation of self-assembles monolayer on silicon wafers by **A.)** Trimethoxy(octadecyl)silane (ODTMS), Triethoxy(3,3,4,4,5,5,6,6,7,7,8,8,8-tridecafluorooctyl)silane (TEFOS) and **B.)** 1,1,1,3,3,3-Hexamethyldisilazane (HMDS).

In Table 4 all used silanes/silazanes are listed. The SAM-functionalized and a non-functionalized wafer were characterized via contact angle measurements (to check the hydrophobicity) and via AFM (to check the roughness of the surface). The pure wafer, after oxygen plasma, shows a contact angle of  $\sim 24^\circ$  and is therefore extremely hydrophilic. AFM reveals a roughness of  $\sim 90$  pm (Figure 58A) and is, as expected for silicon wafers, extremely smooth. After SAM functionalization the surface is getting more hydrophobic. ODTMS and TEFOS show contact angles above  $100^\circ$ , while HMDS has a contact angle of  $\sim 88^\circ$ . The surface roughness was increased in all cases but is in the magnitude of picometers and thus still extremely smooth (Figure 58B, C and D). For HMDS the formation of small islands instead of an equal distribution is visible in the AFM pictures. The main advantage of HMDS compared to the other silanes is that it is not able to auto-polymerize, due of the extremely unfavorable methyl leaving group. Therefore, the formed islands originate from some other aggregation process or impurities. But compared to the method to just cover the surface with the silanes, the chemical vapor deposition (for the silazane) has the advantage of a margin for optimization. For example, the nitrogen flow could be reduced or the temperature can be varied in order to optimize the deposition and minimize aggregation/impurities on the surface.

Despite all efforts, the removal of the wafer from the glued glass turned out to be more difficult than expected. The attractive interactions between ITO/SiO<sub>2</sub> were still too strong and the wafer could not be separated properly from the ITO/glass and shattered upon removal attempts. Nevertheless, some bigger shattered ITO pieces could be saved from the removal of the HMDS functionalized wafer. And the surface indeed shows to be extremely smooth (see Figure 58E,  $\sim 260$  pm, masked area  $\sim 210$  pm). Since the smoothness of the HMDS-functionalized masked surface (Figure 58D,  $\sim 280$  pm) and the resulting ITO surface (Figure 58D,  $\sim 210$  pm) are similar, it might be possible that the islands in Figure 58D are impurities, which are removed prior to ITO sputtering (see chapter IX.1. *Methods and Materials*).

**Table 4.** List of all used SAM agents with the contact angle and roughness of the surface.

| SAM                                               | Contact Angle $\vartheta$ | Roughness $R$ <sup>(a)</sup>              |
|---------------------------------------------------|---------------------------|-------------------------------------------|
| Si-Wafer after O <sub>2</sub> plasma (Figure 58A) | $(24 \pm 1)^\circ$        | $\sim 90$ pm                              |
| ODTMS (Figure 58B)                                | $(107 \pm 1)^\circ$       | $\sim 190$ pm                             |
| TEFOS (Figure 58C)                                | $(103.8 \pm 0.4)^\circ$   | $\sim 440$ pm                             |
| HMDS (Figure 58D)                                 | $(88 \pm 2)^\circ$        | $\sim 650$ pm (masked area $\sim 280$ pm) |
| Collected ITO piece (Figure 58E)                  | -                         | $\sim 260$ pm (masked area $\sim 210$ pm) |

(a) determined via atomic force microscopy

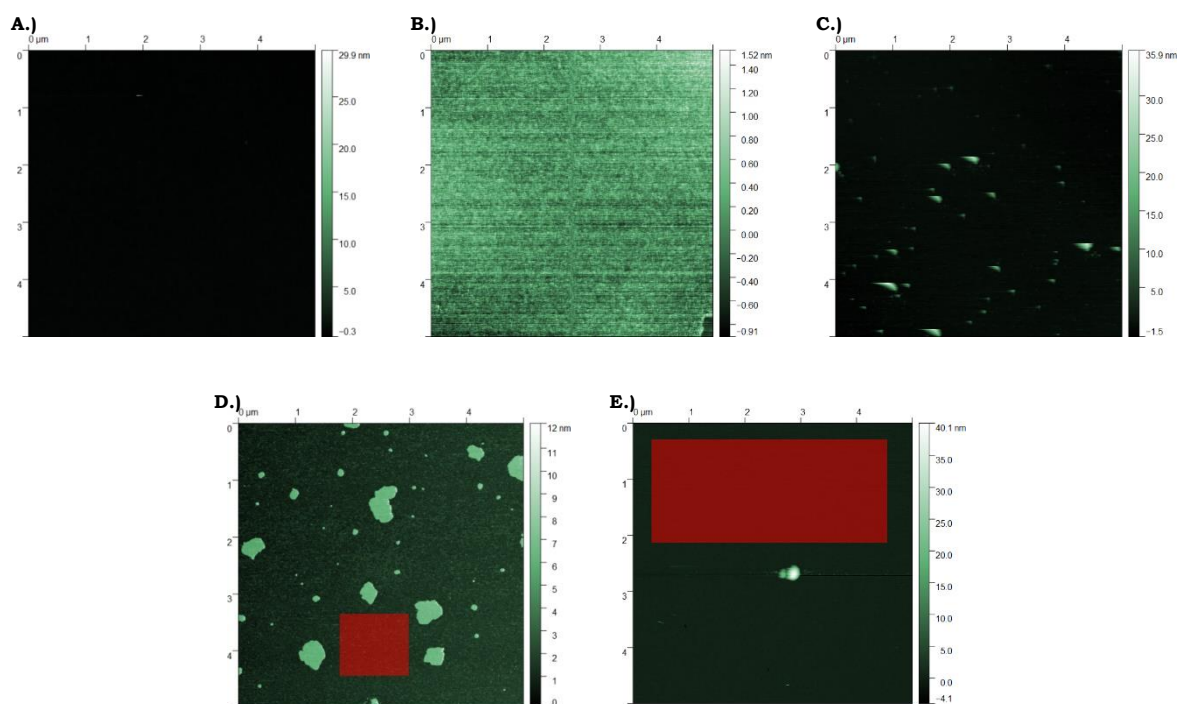


**Figure 58.** AFM picture of **A.)** non-functionalized silicon wafer after oxygen plasma treatment and SAM-functionalized silicon wafer by **B.)** ODTMS, **C.)** TEFOS and **D.)** HMDS. **E.)** ITO surface collected from HMDS functionalized silicon wafer.

#### VII.4.2. Polymerization of PDA

Despite the composition ratio of indium and tin, the thickness of the ITO layer on the glass has also a huge influence on the resistivity of the resulting Glass/ITO substrate and is higher for thin layers.<sup>[85]</sup> Figure 59 shows the PDA polymerized under same conditions for different ITO electrodes. The polymerization on commercial ITO with a resistance of 8 – 12  $\Omega$  is shown in Figure 59A. The cyclic voltammogram of ITO with a higher resistance of  $\sim 300 \Omega$  differs a lot in shape and intensity (Figure 59B). Due to the higher resistance less current flows through the electrode, which means that dopamine is not sufficiently oxidized and less PDA is deposited. Unfortunately, both of these ITO surfaces were too rough to successfully measure thickness/roughness via AFM.

As a comparison, polymerization was also performed on the collected ITO piece from Figure 58E. This electrode has an extremely high resistance of 800 – 1000  $\Omega$ , which probably originates from a thin ITO layer. The polymerization of PDA on it is shown in Figure 59C. As expected, due to the high resistance, the current is extremely low (200 times smaller than the commercial ITO) and is therefore not suitable for PDA polymerization since no significant PDA layer could be detected by AFM. In order to improve the performance of the ITO in Figure 59C, the resistivity needs to be reduced. The most obvious solution to reduce the resistivity is to sputter a thicker ITO layer. Otherwise, thermal treatment by rapid thermal annealing is also a common way to increase the conductivity of ITO surfaces.<sup>[86]</sup>

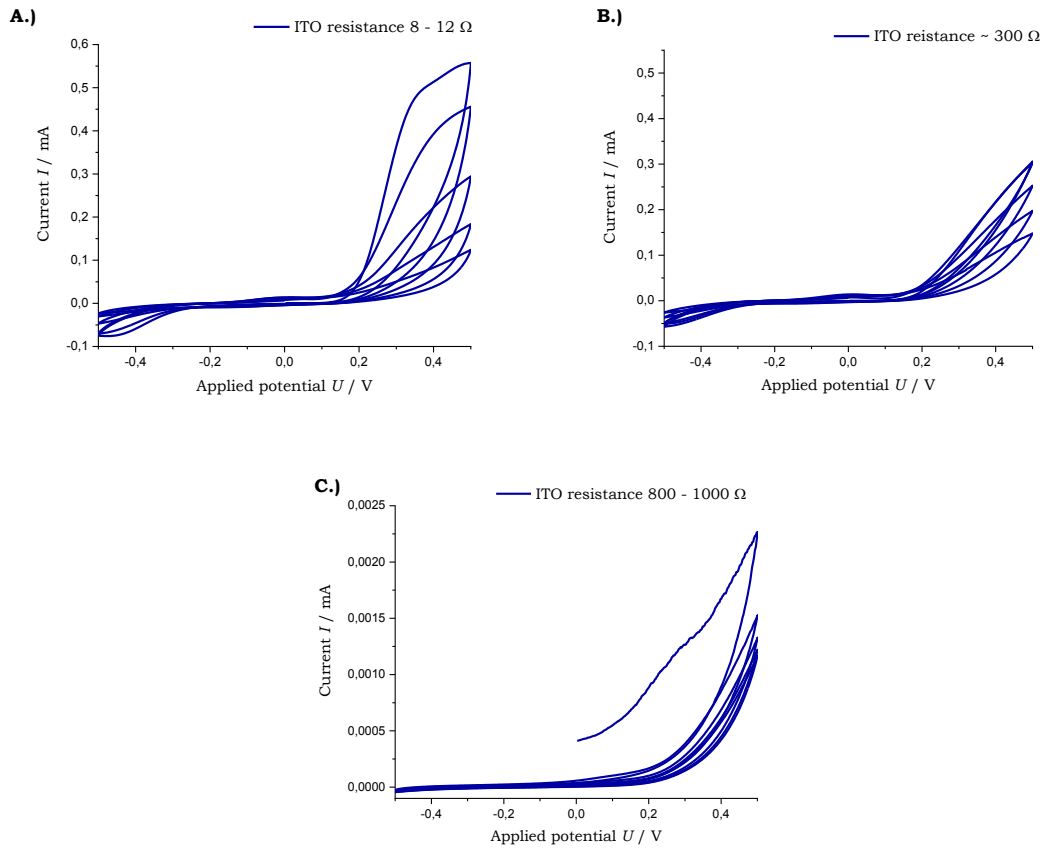


**Figure 59.** Cyclic voltammograms of polydopamine polymerization on ITO with **A.)** 8 – 12  $\Omega$  and **B.)** 300  $\Omega$  resistance. **C.)** Cyclic voltammogram of polydopamine polymerization on self-made ITO electrode with a resistance of 800 – 100  $\Omega$ .

## VIII. Conclusion/Outlook

The premise of modulating hydrogen production and self-recovery of the envisaged system is based on the intrinsic catechol/quinone ratio of PDA. In the first chapter of the discussion PDA was investigated in the response of the catechol/quinone moieties to different pH. Hydrogen production and hole quenching are driven by the chemical driving force acting on the minor catechol groups to be oxidized in basic pH, while in acidic environment catechol formation is favored. The decisive pH switchable redox property of PDA was successfully proven by cyclic voltammetry. Although PDA does not seem to follow an ideal Nernstian behavior, the shift in the redox potential and the nature of the initial current (positive in basic, negative in acidic environment) clearly proves the desired response of PDA to a certain pH. This property can be also useful in order to post-functionalize the PDA surface with a catalyst (or the corresponding ligands) by simple chemistry. Nevertheless, the stability of PDA in different pH solutions could not be examined by cyclic voltammetry (CV) due to chemical change occurring in the positive potential region.

Based on the advanced experimental set-up two new methods were established in order to assess long-term stability and the magnitude as well as the nature of produced photocurrent in the current system. The sweeping potential measurement method (SPM) introduces the half-life  $\tau$  as a new parameter to express the stability of the system, which is clearly increased by embedding the nanorods with PDA. A good compromise between an acceptable photostability and a moderately high photocurrent was achieved for a 0.8 mg/mL spin coated CdSe@CdS core-shell nanorod (NR) solution embedded in 5 CV cycles of PDA. Keeping the PDA-to-NR ratio constant, PDA cycles up to 15 cycles are possible, while maintaining the same optoelectronic properties. Additionally, the half-life is directly correlated to the photocurrent and revealed in combination with transient absorption spectroscopy (TAS) a better understanding of the complex synergy between PDA and NR, i.e. a better understanding of electron dynamics within the conduction band of the NR, the hole quenching ability of PDA and the dominance of long NR compared to short NR in terms of spatial electron/hole charge separation.

Constant potential measurements (CPM), as the second established method, facilitates the investigation of the single and combined composites in their response to an applied potential or to an additional hole scavenger. Negative as well as positive photocurrents, were measured and enabled the possibility to assess a specific system composition towards hydrogen production. Thereby, ascorbic acid at an applied potential of  $-0.5$  V turned out to be an extremely efficient hole scavenger since it increased the photocurrent in pure NR ( $\sim 60 \mu\text{A cm}^{-2} \text{ s} \rightarrow \sim 8700 \mu\text{A cm}^{-2} \text{ s}$ ) as well as in combined PDA/NR films ( $\sim 450 \mu\text{A cm}^{-2} \text{ s} \rightarrow \sim 2700 \mu\text{A cm}^{-2} \text{ s}$ ) exceptionally. Finally, it remains on the catalyst (CAT) whether the chemical driving force predominates the electrostatic driving force to successfully reduce hydrogen and is thus the next step in order to optimize the photoelectrochemical cell as it is now.

The establishment of a procedure to produce ultra-smooth ITO remains challenging. Separation at the ITO/SAM interface is too difficult and requires either new SAM agents to reduce ITO/SiO<sub>2</sub> interactions or a new method to separate the layers. First attempts were made in order to use capillary forces to introduce a water layer between the wafer and glass. Shock freezing followed by thermal expansion of water should provide a well distributed force to separate the slides smoothly.

Additionally, in order to polymerize PDA properly, less resistive ITO is required and might be accessible through thicker ITO layers or by thermal annealing of the produced slides.

Overall, the versatile properties of PDA were exploited and the response of the current system to different changes was examined to enhance the performance of the NR in the desired photoelectrochemical cell towards hydrogen production. Furthermore, the collected results in this work and future results on the NR/PDA/CAT films will allow a deeper understanding of the electron dynamics in the final device, which can lead to the implementation of useful adjustments in order to improve the catalytic efficiency of the system

However, there are some major issues which need further investigation. For example, CPM has shown that under harsh irradiation conditions, PDA is not a sufficient hole scavenger. This might be connected to the insulating property of PDA. Increasing the mobility of charge carriers (conductivity) in PDA might increase the efficiency of the system in different ways. Hole quenching, spatial separation of electron/hole and an enhanced electron transportation network to the attached catalyst could benefit from an increased conductivity within the PDA film and increase the performance of the desired system towards hydrogen production. Therefore, copolymerization of PDA with polyelectrolytes such as polypyrrole (PPY) might be a possibility to achieve this goal. Preliminary studies have already been performed and according to the synthetic cyclic voltammograms of PDA-co-PPY it is obvious that a 5 % content of PPY leads already to a significant improvement in the conductivity of the deposited films.

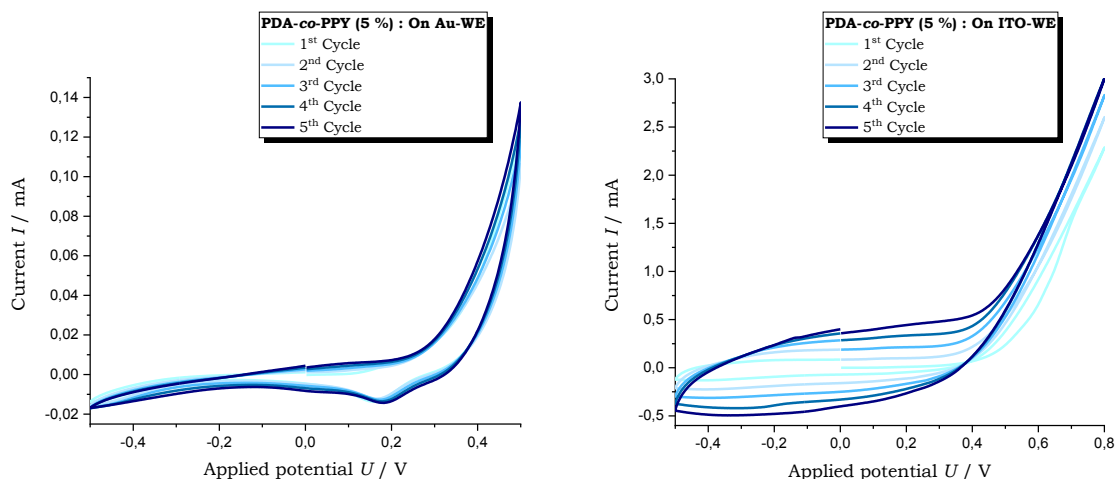


**Figure 60.** Cyclic voltammogram of PDA-co-PPY formation on a gold WE (A) and ITO WE (B) indicate an increase in the conductivity of the resulting film.



## IX. Experimental Part

### IX.1. Methods and Materials

All cyclic voltammograms, SPM and CPM raw data were first processed with *Microsoft Excel 365*. Functional fits, interpolations, integration, plots and diagrams were processed with *Origin 2018*.

**Cyclic Voltammetry** were performed in a three-electrode set-up similar to Figure 13 using a *Metrohm AG Autolab potentiostat (type PGSTAT204)*. The potentiostat has an output voltage of 20 V with a maximum current of 400 mA. The dive comes along with a potential  $U$  and current  $I$  determination accuracy of  $\pm 0.2\%$  for each and is supported by the software *NOVA (V2.1.4)*. Gold and ITO WE were purchased from *SIGMA-ALDRICH* as coated microscope slides and were cut to the preferred shape. Gold and platinum CE were purchased as wires from *Alfa Aesar* (1 mm diameter for gold, 0.7 mm diameter for platinum wire). Ag/AgCl RE was purchased from *Metrohm* (type 6.0724.140) and KCl was purchased from *Honeywell*.

**Photocurrent measurements (SPM and CPM)** were performed according to the set-up in Figure 23. Additional to the potentiostat a shutter from *Thorlabs GmbH (SHM1/M)* with a universal power supply for 100 - 240 volt alternating current and 47 - 63 Hz is used. A *Single-Color Cold Visible Mounted LED + lens tube (M455L4)* is connected to the shutter, controlled by a compatible LED driver (*LEDD1B*) and exhibits light with a wavelength of 455 nm, output power of 1150 mW and a maximum current of 1000 mA. The **power** of the lamp was measured on a *PM100D* sensor from *Thorlabs*. The polymerization and photocurrent measurement parameters set in the *NOVA* were mentioned in chapter IX.2. *Experimental Implementation* for the specific experiments.

**Atomic force microscopy (AFM)** was performed on a *BRUKER Dimension FastScan* with an *OLYMPUS OMCL 240TN cantilever* (frequency 70 kHz, spring constant 2 N/m). The data were processed by the software *Gwiddion (V2.56)*.

The **scanning electron microscopy (SEM)** measurements were carried out on a *Hitachi SU8000* with a cold field emitter gun. Acceleration voltage can be adjusted from 0.5 – 20 kV. The data were processed by the software *ImageJ (V.1.53)*.

A *Tecnai F20* from *FEI company* was used for the **(High-resolution) Transmission electron microscopy (HR-TEM)** measurements with an acceleration voltage of 200 kV.

The used **spin coater** was operated by a rotational speed controller from *Headway Research Inc.*

An **optical contact angle device** from *dataphysics (type OCA 35)* was supported by a video system in order to determine contact angles between 0 – 180 ° with an accuracy of  $\pm 0.1^\circ$ . The video-based measurement is supported by the software *SCA202 (V.4.1.10)*.

**Oxygen plasma** was performed on a *FEMTO BL plasma system* from *Diener Electronic Plasma-Surface-Technology* supported by a *Pfeiffer vacuum pump DUO line 1.6*. The oxygen gas bottle was purchased from *Westfalen AG*.

**Argon Plasma** was performed on a *Harrick expanded plasma cleaner* coupled to a *standard HiScroll 6 vacuum pump* with a pressure sensor. The argon bottle was purchased from *Westfalen AG*.

**ITO was sputtered** on an *Edwards Auto 500 sputtering system*. The target was cleaned and activated at 150 W and  $\sim 1.2 \cdot 10^{-2}$  mbar pressure with a gas flow of 80 sccm argon and 15 sccm oxygen. ITO sputtering is performed at 200 W and  $\sim 3.4 \cdot 10^{-3}$  mbar pressure with a gas flow of 22 sccm argon. ITO deposition can be observed by a connected quartz crystal microbalance.

**Resistance measurements** were performed by a *True RMS Multimeter* from *EXTECH Instruments* (two-point probe).

## IX.2. Experimental Implementation

Polymerization and photocurrent measurements were performed in the new cuvette holder set-up. Therefore, disposable cuvettes (purchased from *Brand*) for polymerizations and quartz cuvettes (purchased from *VWR*) for photocurrent measurements were cut to 30 mm inside length. In order to prevent liquid-loss due to capillary forces, teflon tape was wrapped around the cuvette cap, before capping the cuvettes. The WE electrodes were cleaned prior use. ITO WE (purchased from *SIGMA ALDRICH*) were cleaned by sonication (15 minutes in acetone, 15 minutes in ethanol, 15 minutes in milliQ water). Gold WE (purchased from *SIGMA ALDRICH*) were cleaned by argon-plasma treatment for 10 minutes.

### a. Buffer

A pH 7 phosphate buffer (100 mM) was prepared by 0.0191 M monobasic sodium phosphate (purchased from SIGMA-ALDRICH) and 0.0308 M dibasic sodium phosphate (purchased from SIGMA-ALDRICH) and exhibits a  $pK_s$  of 7.2 and an ionic strength of 0.223 M. pH variations above  $\pm 0.02$  were adjusted by 13 M HCl or NaOH solutions. The buffer was pre-bubbled for at least 15 minutes prior to use.

### b. Polydopamine cuvette electropolymerization

PDA was electropolymerized at a concentration of 1 mg/mL of dopamine hydrochloride (purchased from SIGMA-ALDRICH) in a 100 mM phosphate buffer (1.3 mL) at pH = 7, which was also serving as electrolyte. The electrochemical cell was composed of an ITO or gold WE, gold wire CE and a 3 M Ag/AgCl reference electrode. If not other mentioned, cyclic voltammetry was generally performed in a potential range from  $-0.5$  V to  $0.5$  V at a scan rate of  $0.01$  V/s in  $0.00244$  V steps.

### c. Polydopamine-co-pyrrole cuvette electropolymerization

PDA-co-PPY was electropolymerized at a concentration of 100 mM of dopamine hydrochloride and 5.2 mM pyrrole in  $N_2$  pre-bubbled MilliQ water. Additional 100 mM of sodium p-toluenesulfonate was used as electrolyte and at the same time dopant for the pyrrole polymerization leading to a total solution volume of 1.3 mL. The electrochemical cell setup and the polymerization parameters were analog to *b. Polydopamine cuvette electropolymerization*.

### d. Spin coating

A solution of  $2.22$  L/cm<sup>2</sup> of a CdSe@CdS core-shell nanorod solution stabilized by trioctylphosphine oxide in toluene was spin coated on an ITO WE. Spin coating was performed at 2500 rotations per minute for 60 seconds. The nanorod solution concentration ranged from  $0.05$  mg/mL to  $2$  mg/mL.

### e. Analytical cyclic voltammetry

The electropolymerized films were characterized via cyclic voltammetry in a potential range from  $-0.5$  V to  $0.5$  V at a scan rate of  $0.01$  V/s in  $0.00244$  V steps in a pH 7 phosphate buffer (100 mM).

### f. Sweeping potential photocurrent measurement (SPM)

The potential was set to sweep from  $-0.5$  to  $0.5$  V at a scan rate of  $0.005$  V/s in  $0.00244$  steps. A prepared film was irradiated in a 5 mm light cone diameter with a power of 100 mW.

The shutter controlled the exposure time to light and was turned on/off every 10 seconds for a total time of 200 seconds. This procedure was repeated 30 times in order to receive 30 absolute mean photocurrents for 100 minutes of irradiations. Phosphate buffer (100 mM, 1.5 mL) at pH 7 was used as an electrolyte without any additional hole scavenger. Additionally, a platinum wire (0.7 mm diameter) was used as a CE and a 3 M Ag/AgCl reference system as RE.

#### g. Constant potential photocurrent measurement (CPM)

For CPM, the potential was held constant at a specific value, while irradiating a prepared film (WE) in a 5 mm diameter light cone with a power of 100 mW. The shutter controlled the exposure to light and was turned on/off every 5 seconds for 30 minutes. A platinum wire (0.7 mm diameter) was used as a CE and a 3 M Ag/AgCl reference system as RE. The phosphate buffer had a theoretical ionic strength of  $c_s$  0.22 M. In order to compare different hole scavengers, the ionic strength needed to be constant. Therefore, also the charge of the hole scavenger were considered. Table 5 represents the composition of the hole scavenger (electrolyte) solutions used for CPM.

**Table 5.** Composition of hole scavenger solutions in phosphate buffer (PB) (methanol, ascorbic acid, sodium ascorbate and sodium sulfite) used for constant potential photocurrent measurements.

| Hole Scavenger                                    | Composition                                                                                                                |
|---------------------------------------------------|----------------------------------------------------------------------------------------------------------------------------|
| None                                              | 0.75 mL PB ( $c_{is} = 0.11$ M) + 0.75 mL H <sub>2</sub> O + 4.9 mg NaCl* ( $c_{is} = 0.11$ M)                             |
| Methanol (MeOH)                                   | 0.75 mL PB ( $c_{is} = 0.11$ M) + 0.75 mL MeOH** + 4.9 mg NaCl* ( $c_{is} = 0.11$ M)                                       |
| Ascorbic acid (HAsc)                              | 0.75 mL PB ( $c_{is} = 0.11$ M) + 0.75 mL H <sub>2</sub> O + 16.5 mg HAsc** + 4.9 mg NaCl* ( $c_{is} = 0.11$ M)            |
| Sodium Ascorbate (NaAsc)                          | 0.75 mL PB ( $c_{is} = 0.11$ M) + 0.75 mL H <sub>2</sub> O + 16.5 mg NaAsc* ( $c_{is} = 0.11$ M)                           |
| Sodium sulfite (Na <sub>2</sub> SO <sub>3</sub> ) | 0.75 mL PB ( $c_{is} = 0.11$ M) + 0.75 mL H <sub>2</sub> O + 3.5 mg Na <sub>2</sub> SO <sub>3</sub> * ( $c_{is} = 0.11$ M) |

#### h. Silicon wafer functionalization for ultra-smooth ITO

The silicon wafer (purchased from *Plano*) was cut to the length needed for a cuvette polymerization (~ 4 cm) and a width of ~ 2.5 cm. The wafer was cleaned by sonication (15 minutes in acetone, 15 minutes in ethanol, 15 minutes in milliQ water) and dried under nitrogen flow. The cleaned wafer was activated by oxygen plasma treatment for 10 minutes at 100 % intensity. Three different silicon-based chemicals were used to functionalize the activated wafer. Trimethoxy(octadecyl)silane (purchased from *SIGMA ALDRICH*) and Triethoxy(3,3,4,4,5,5,6,6,7,7,8,8,8-tridecafluorooctyl)silane (purchased from *TCI*) were pipetted on the wafer and let react for 24 hours. Functionalization with 1,1,1,3,3,3-Hexamethyldilizane (HMDS, purchased from *TCI*) was performed via chemical vapor deposition. The activated wafer was placed in the set-up and heated for 1 h at 120 °C while flushing with nitrogen. Then HMDS was introduced as gas vapor for 50 minutes at 120 °C.

After silane/silazane functionalization the wafer was washed with acetone, ethanol and then milliQ water and dried under nitrogen flow. ITO was sputtered on the functionalized silicon surface. A commercially available resin-based glue (*EPO-TEK 353ND* purchased from *Epoxy Technology*) was degassed for 1 h in a desiccator at 10 mbar. The functionalized wafer (ITO surface) was then glued to a cleaned (sonication for 15 minutes in acetone, 15 minutes in ethanol, 15 minutes in milliQ water) microscope slide. The glued slides were mechanically pressed together and placed in the oven for 30 minutes at 80 °C. After cooling to room temperature, the Si-wafer was tried to separate from the microscope slide.

\* complete dissociation assumed

\*\* no contribution to ionic strength assumed



## X. Appendix

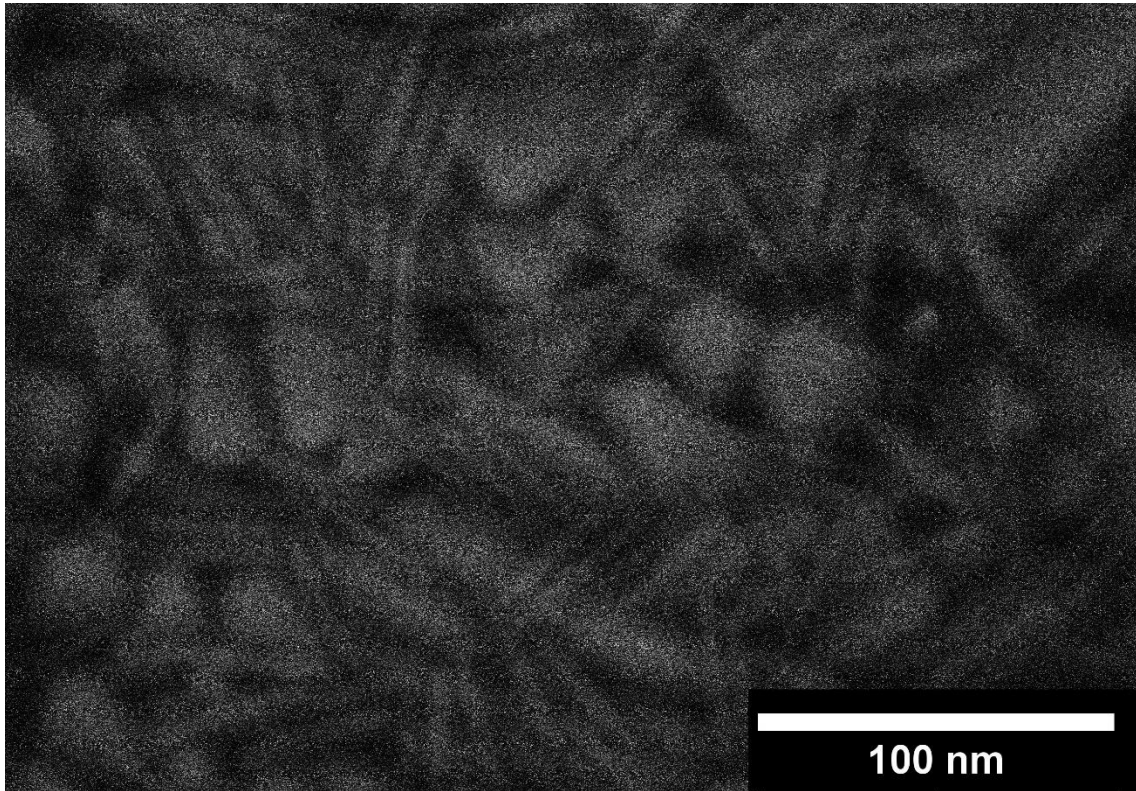


**Figure 61.** SEM picture of embedded CdSe@CdS nanorods (1.2 mg/mL spin coated solution) embedded in 5 cycles PDA on an indium tin oxide electrode. Scale: 100 nm.

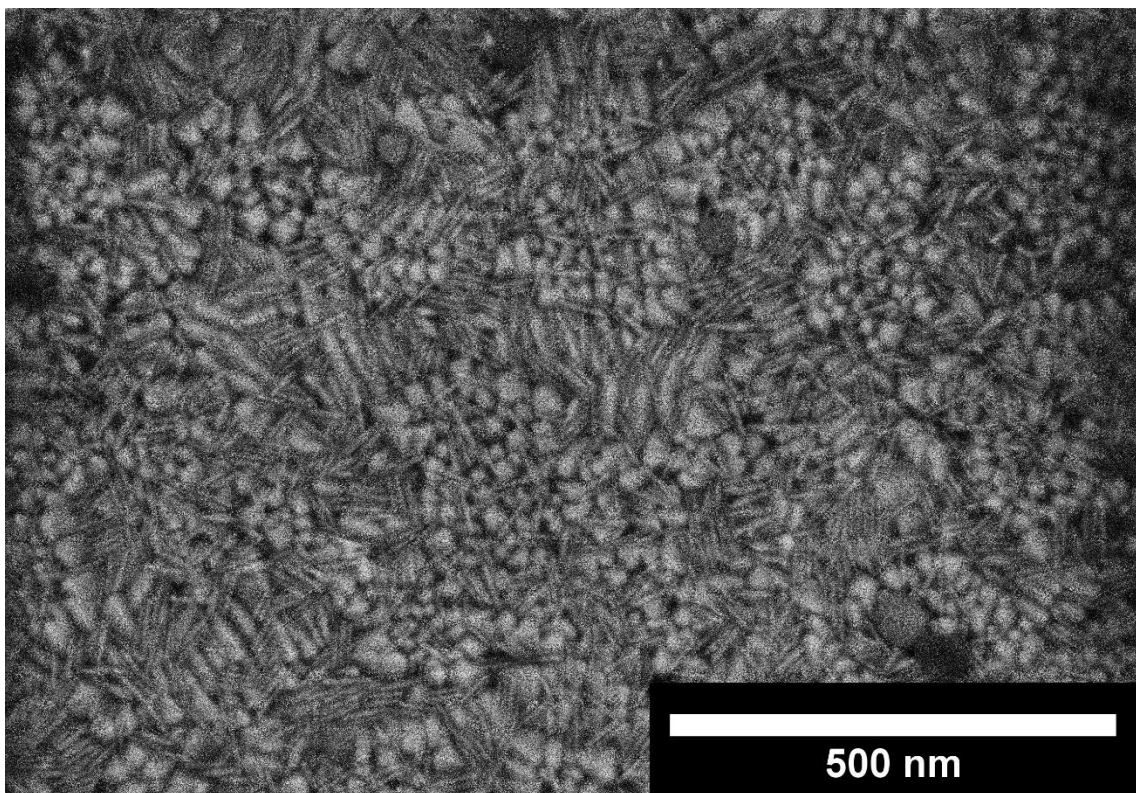


**Figure 62.** SEM picture of embedded CdSe@CdS nanorods (1.2 mg/mL spin coated solution) embedded in 5 cycles PDA on indium tin oxide electrode. Scale: 500 nm.



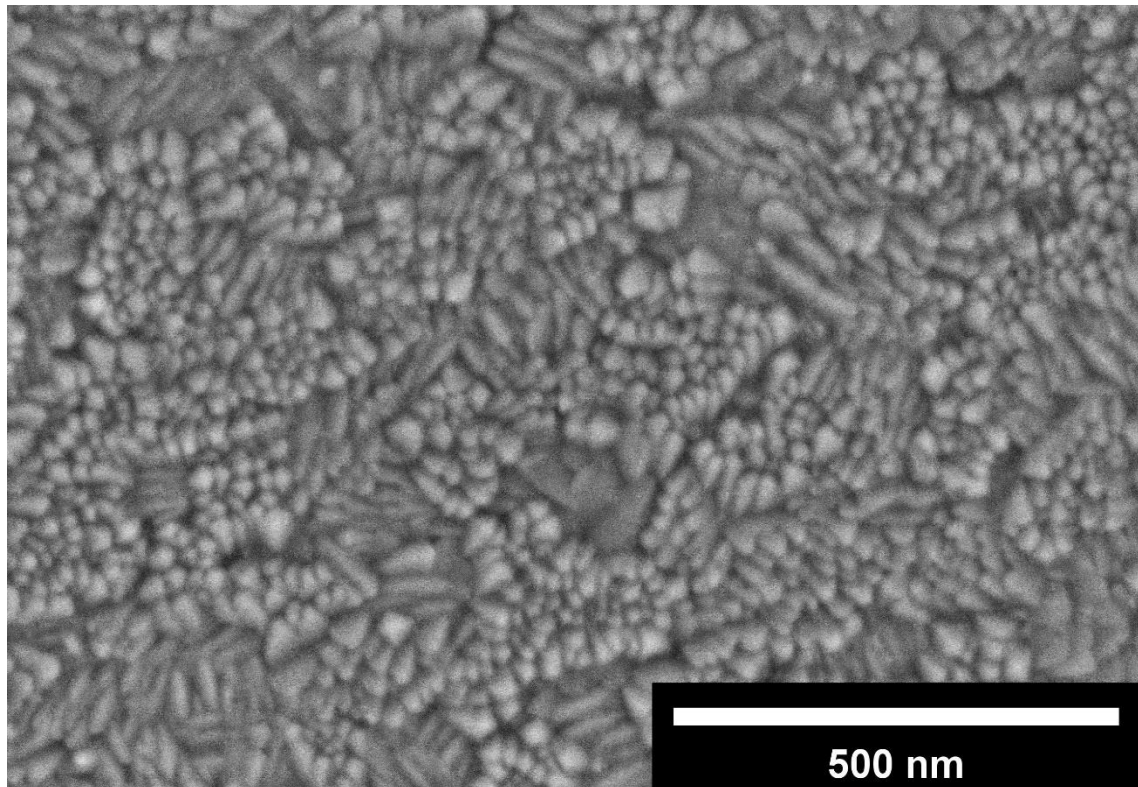


**Figure 63.** SEM picture of embedded CdSe@CdS nanorods (1.2 mg/mL spin coated solution) embedded in 5 cycles PDA on indium tin oxide electrode after irradiation and degradation of the nanorods. Resolution: 500 nm.

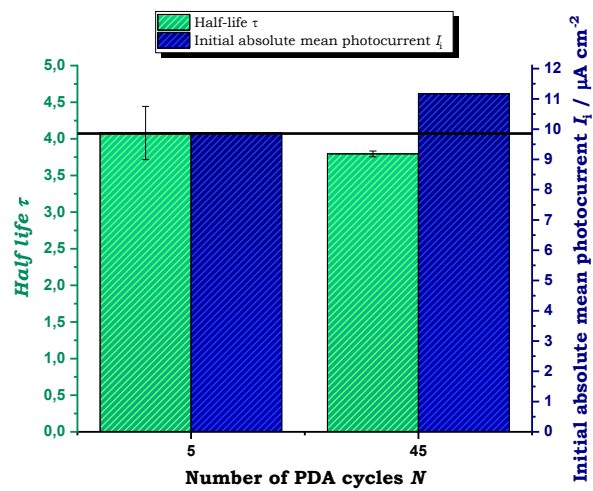


**Figure 64.** Comparison of 5 and 45 cycle PDA film regarding to the half-life and initial mean photocurrent while irradiation. Data were collected with the old set-up similar to Figure 18.

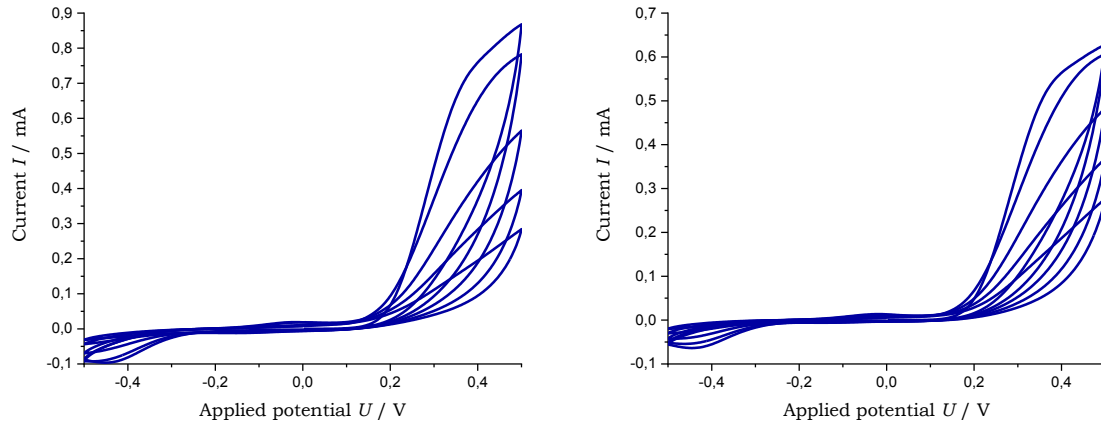


**Figure 65.** Cyclic voltammogram of 5 cycle PDA film used for acidic pH treatment (left) and basic pH treatment (right) in chapter VII.1.2. Redox behavior: Controllability of catechol/quinone ratio.

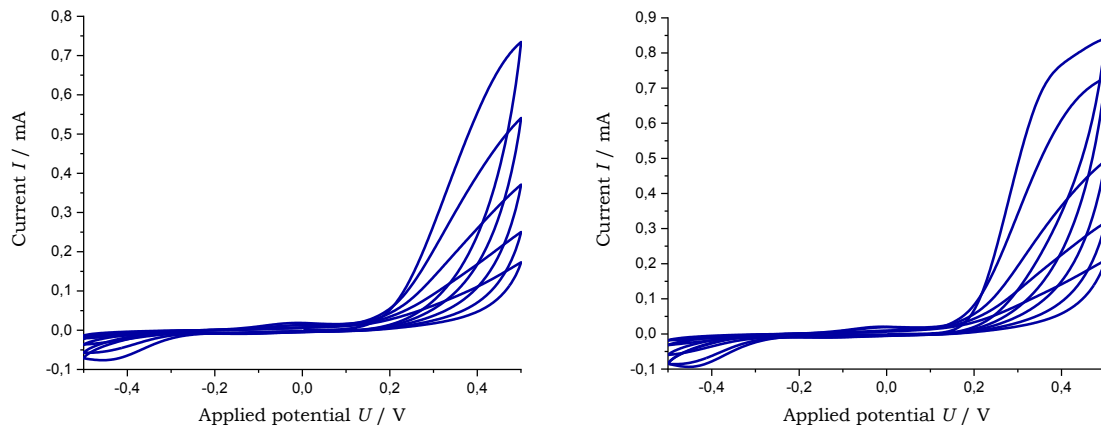


**Figure 66.** Cyclic voltammogram of 5 cycle PDA film used for neutral pH treatment (left) and applied potential treatment (right) in chapter VII.1.2. Redox behavior: Controllability of catechol/quinone ratio.

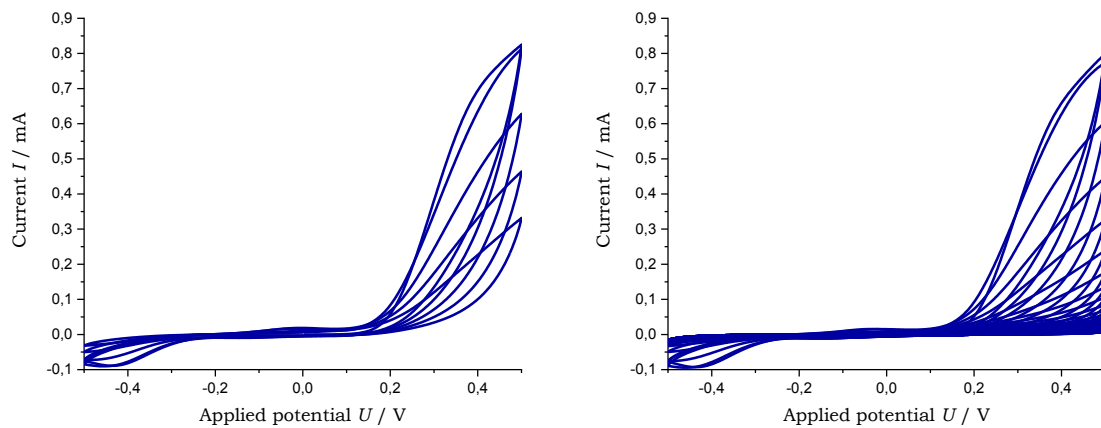


**Figure 67.** Cyclic voltammogram of 5 cycle PDA film (left) and 45 cycle PDA film (right) used for CPM in chapter VII.3.1. Sweeping potential measurement ( $\rightarrow$  Figure 64).

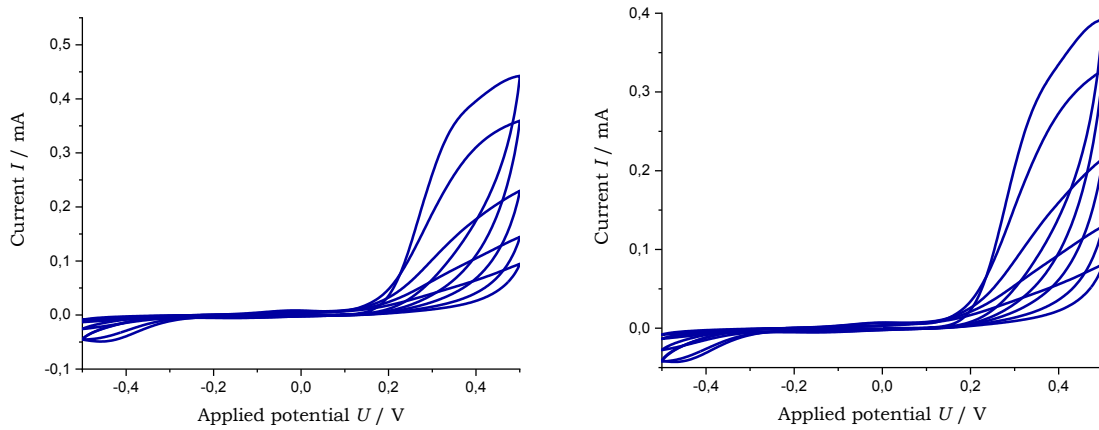


**Figure 68.** Cyclic voltammogram of 5 cycle PDA film on 0.05 mg/mL spin coated CdSe@CdS solution (left) and 0.1 mg/mL spin coated CdSe@CdS solution (right) used for CPM in chapter VII.3.1. Sweeping potential measurement.

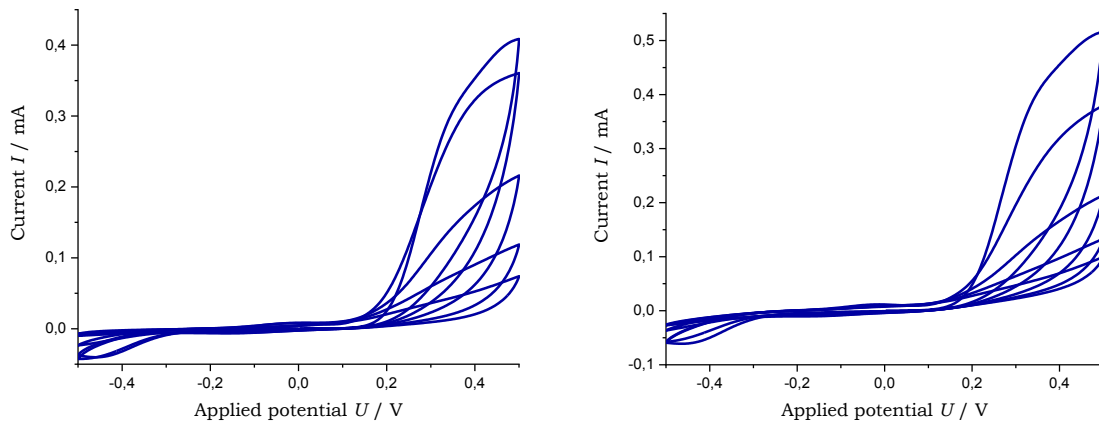


**Figure 69.** Cyclic voltammogram of 5 cycle PDA film on 0.2 mg/mL spin coated CdSe@CdS solution (left) and 0.3 mg/mL spin coated CdSe@CdS solution (right) used for CPM in chapter VII.3.1. Sweeping potential measurement.

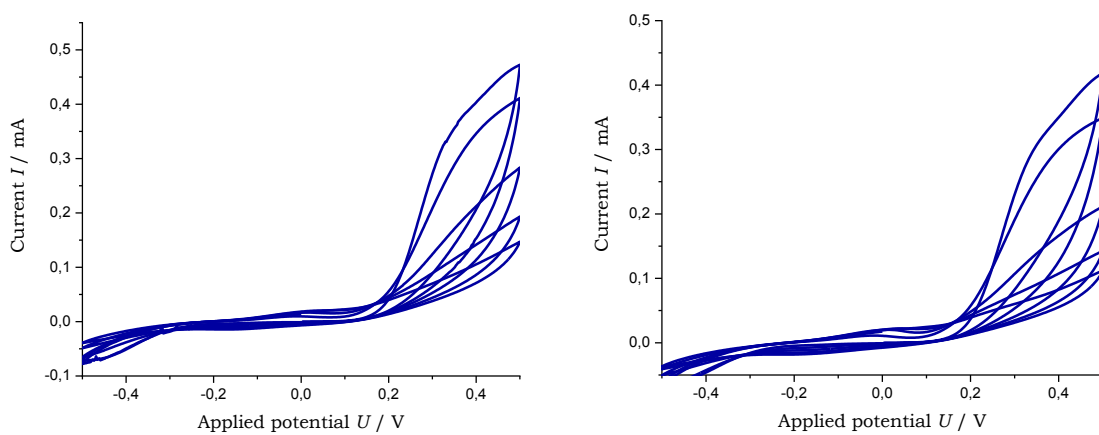


**Figure 70.** Cyclic voltammogram of 5 cycle PDA film on 0.4 mg/mL spin coated CdSe@CdS solution (left) and 0.8 mg/mL spin coated CdSe@CdS solution (right) used for CPM in chapter VII.3.1. Sweeping potential measurement.



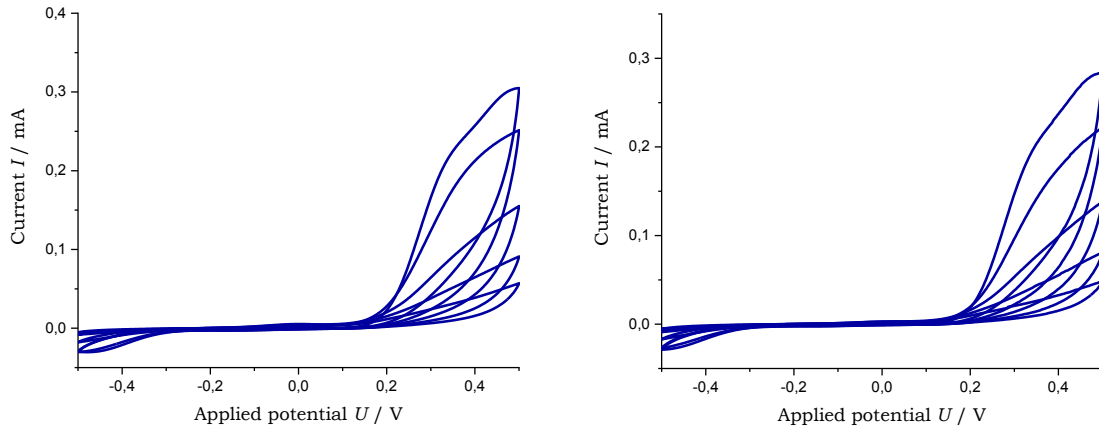


**Figure 71.** Cyclic voltammogram of 5 cycle PDA film on 1.6 mg/mL spin coated CdSe@CdS solution (left) and 2.0 mg/mL spin coated CdSe@CdS solution (right) used for CPM in chapter VII.3.1. Sweeping potential measurement.

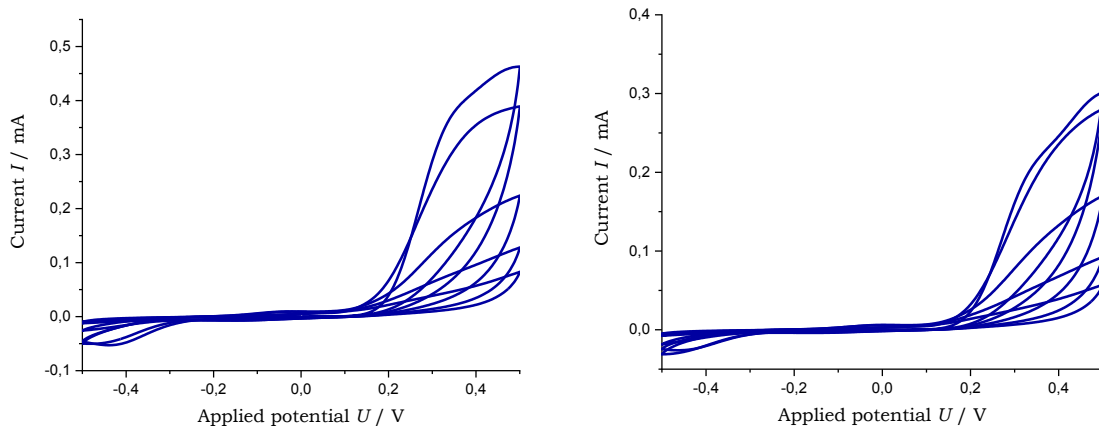


**Figure 72.** Cyclic voltammogram of pure 5 cycle PDA film (left) and with 1.2 mg/mL spin coated CdSe@CdS solution (right) used for CPM in chapter VII.3.1. Sweeping potential measurement.

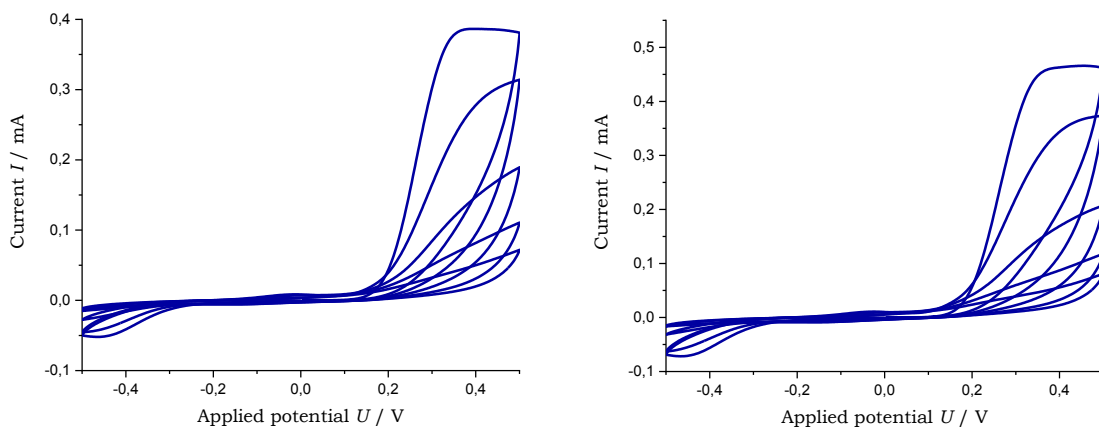


**Figure 73.** Cyclic voltammogram of pure 5 cycle PDA film used for CPM at  $U = 0.3$  V (left) and  $U = 0.4$  V in chapter VII.3.2. Constant potential measurement.

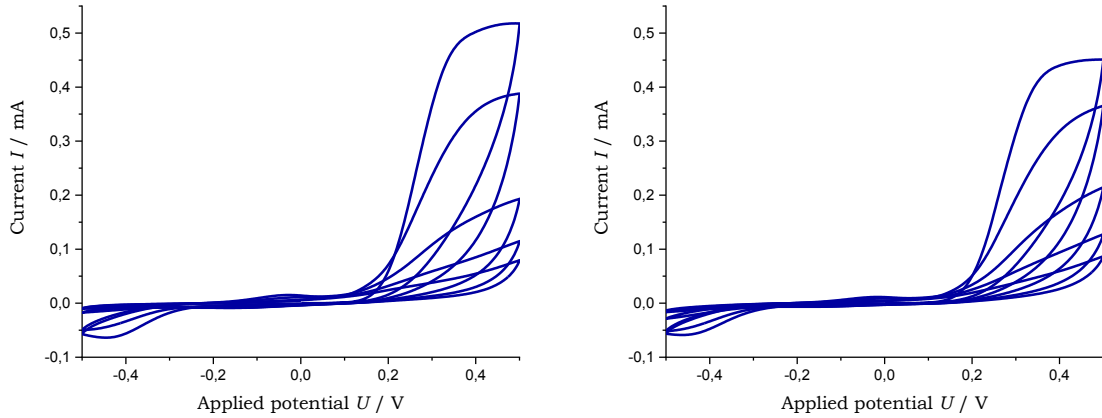


**Figure 74.** Cyclic voltammogram of pure 5 cycle PDA film used for CPM at  $U = 0.5$  V (left) and  $U = 0.2$  V in chapter VII.3.2. Constant potential measurement.

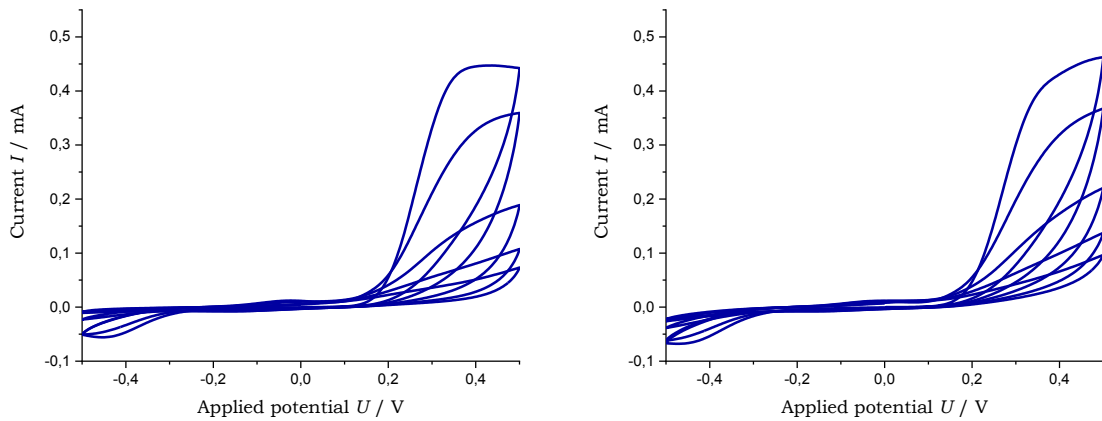


**Figure 75.** Cyclic voltammogram of pure 5 cycle PDA film used for CPM at  $U = 0.1$  V (left) and  $U = -0.1$  V in chapter VII.3.2. Constant potential measurement.

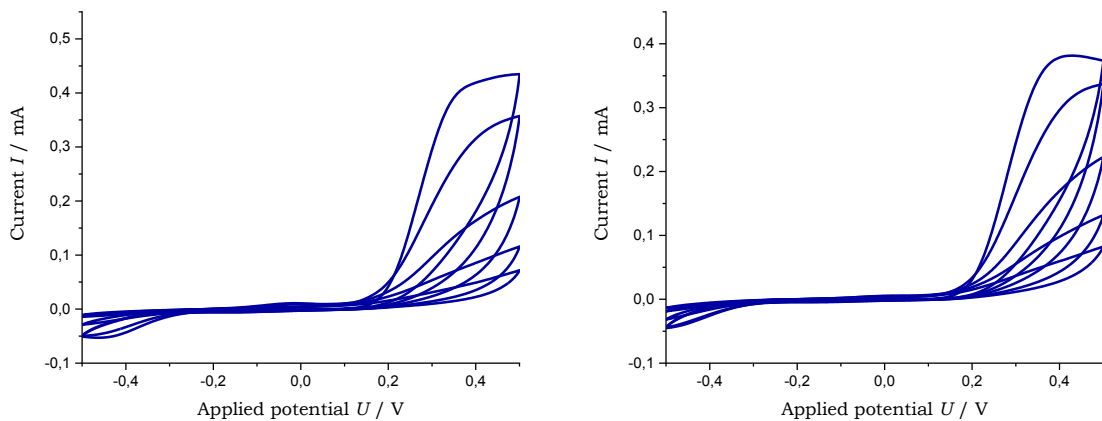


**Figure 76.** Cyclic voltammogram of pure 5 cycle PDA film used for CPM at  $U = -0.4$  V (left) and  $U = -0.2$  V in chapter VII.3.2. Constant potential measurement.

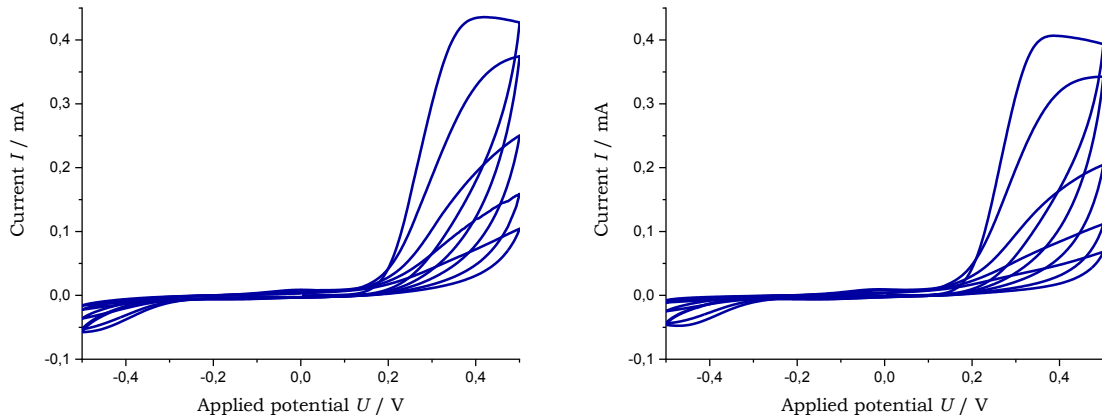


**Figure 77.** Cyclic voltammogram of pure 5 cycle PDA film used for CPM at  $U = -0.3$  V (left) and  $U = -0.5$  V in chapter VII.3.2. *Constant potential measurement.*

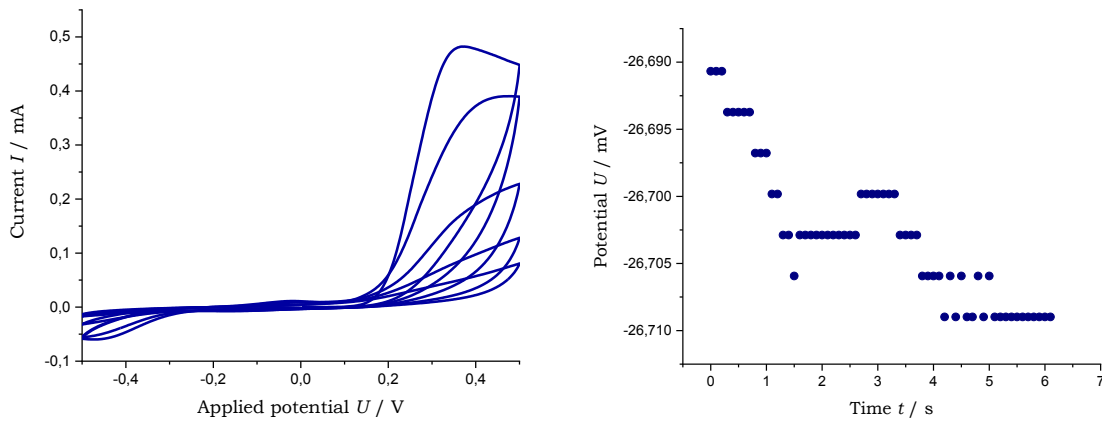


**Figure 78.** Cyclic voltammogram of pure 5 cycle PDA film used for CPM at  $U = OCP = -0.027$  V (left) and OCP determination measurement (right) in chapter VII.3.2. *Constant potential measurement.*

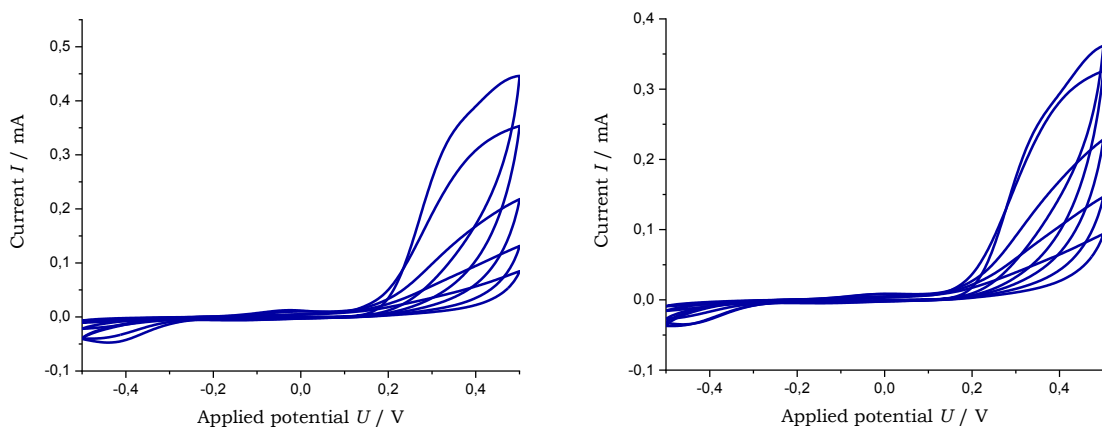


**Figure 79.** Cyclic voltammogram of pure 5 cycle PDA film used for CPM at  $U = -0.5$  V for no (left) and methanol (right) as additional hole scavenger in chapter VII.3.2. *Constant potential measurement.*

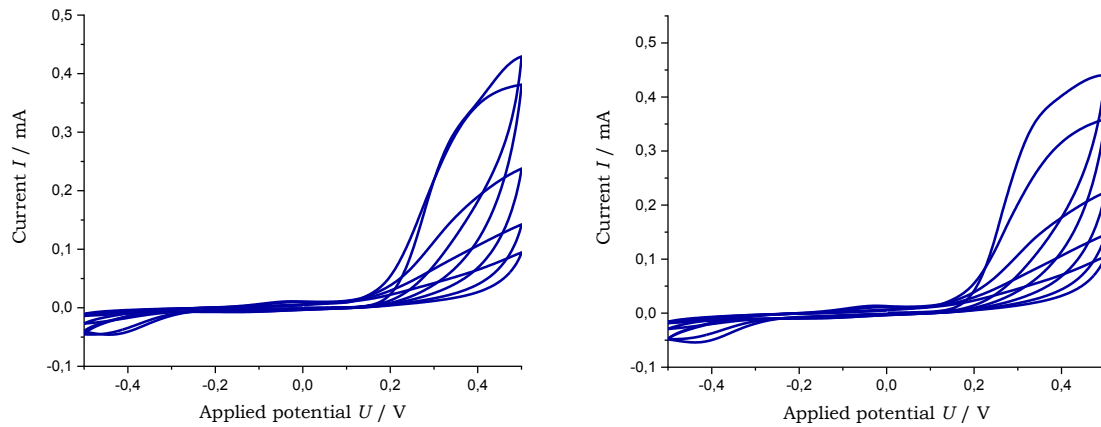


**Figure 80.** Cyclic voltammogram of pure 5 cycle PDA film used for CPM at  $U = -0.5$  V for sodium ascorbate (left) and ascorbic acid (right) as additional hole scavenger in chapter VII.3.2. *Constant potential measurement.*

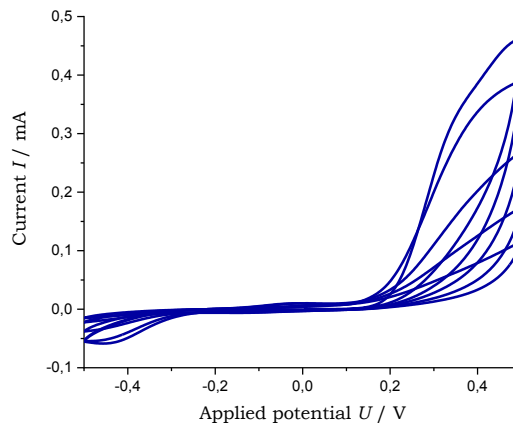


**Figure 81.** Cyclic voltammogram of pure 5 cycle PDA film used for CPM at  $U = -0.5$  V for sodium sulfite as additional hole scavenger in chapter VII.3.2. *Constant potential measurement.*

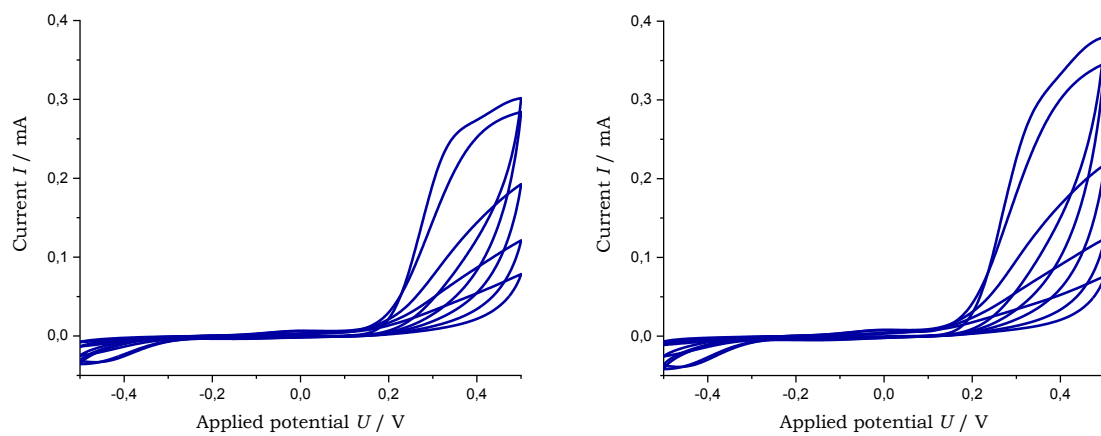


**Figure 82.** Cyclic voltammogram of 5 cycle PDA film on 0.8 mg/mL spin coated CdSe@CdS solution used for CPM at  $U = -0.5$  V (left) and  $U = -0.1$  V (right) in chapter VII.3.2. *Constant potential measurement.*

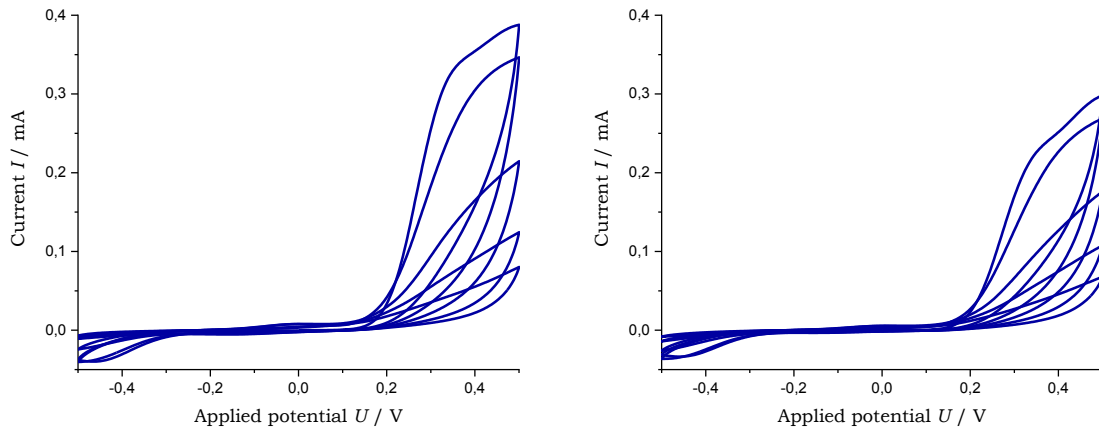


**Figure 83.** Cyclic voltammogram of 5 cycle PDA film on 0.8 mg/mL spin coated CdSe@CdS solution used for CPM at  $U = -0.2$  V (left) and  $U = -0.3$  V (right) in chapter VII.3.2. *Constant potential measurement.*

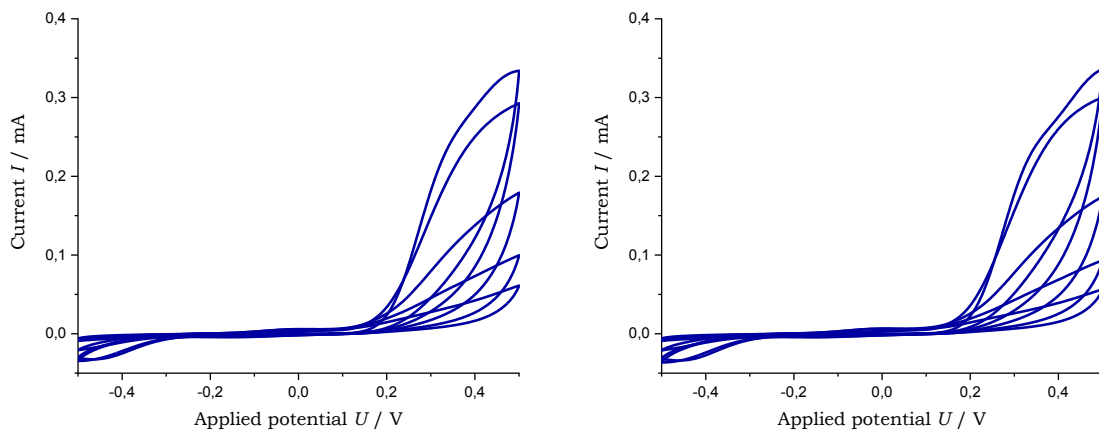


**Figure 84.** Cyclic voltammogram of 5 cycle PDA film on 0.8 mg/mL spin coated CdSe@CdS solution used for CPM at  $U = -0.4$  V and with no additional hole scavenger (right). VII.3.2. *Constant potential measurement.*

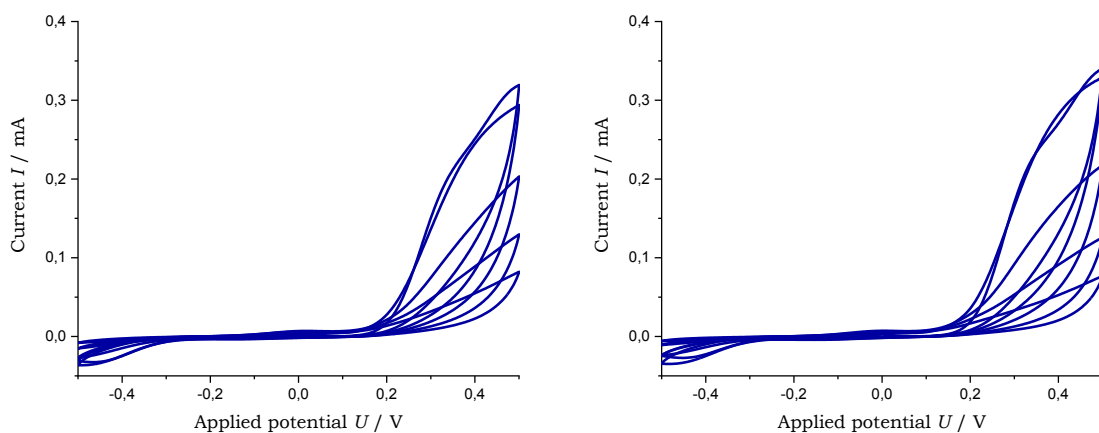


**Figure 85.** Cyclic voltammogram of 5 cycle PDA film on 0.8 mg/mL spin coated CdSe@CdS solution used for CPM at  $U = -0.5$  V for sodium ascorbate (left) and sodium sulfite (right) as additional hole scavenger in chapter VII.3.2. *Constant potential measurement.*

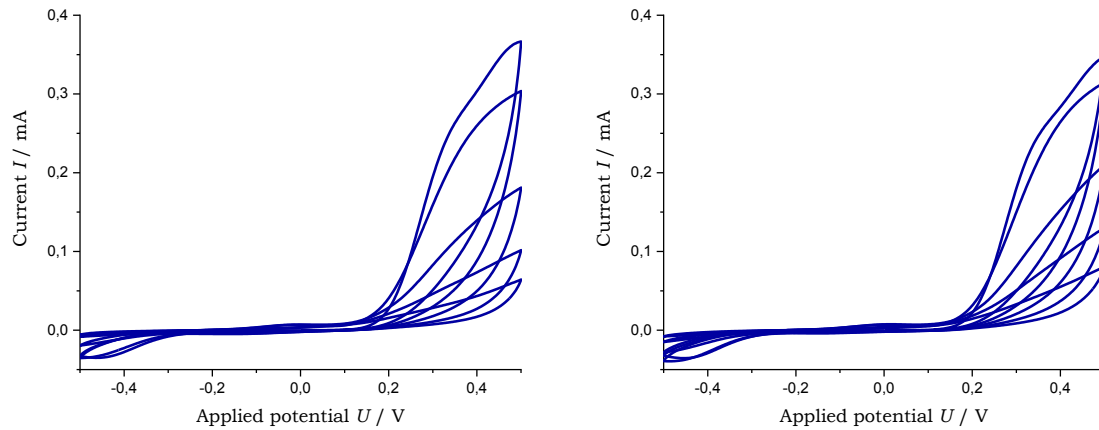


**Figure 86.** Cyclic voltammogram of 5 cycle PDA film on 0.8 mg/mL spin coated CdSe@CdS solution used for CPM at  $U = -0.5$  V for methanol (left) and ascorbic acid (right) as additional hole scavenger in chapter VII.3.2. *Constant potential measurement.*

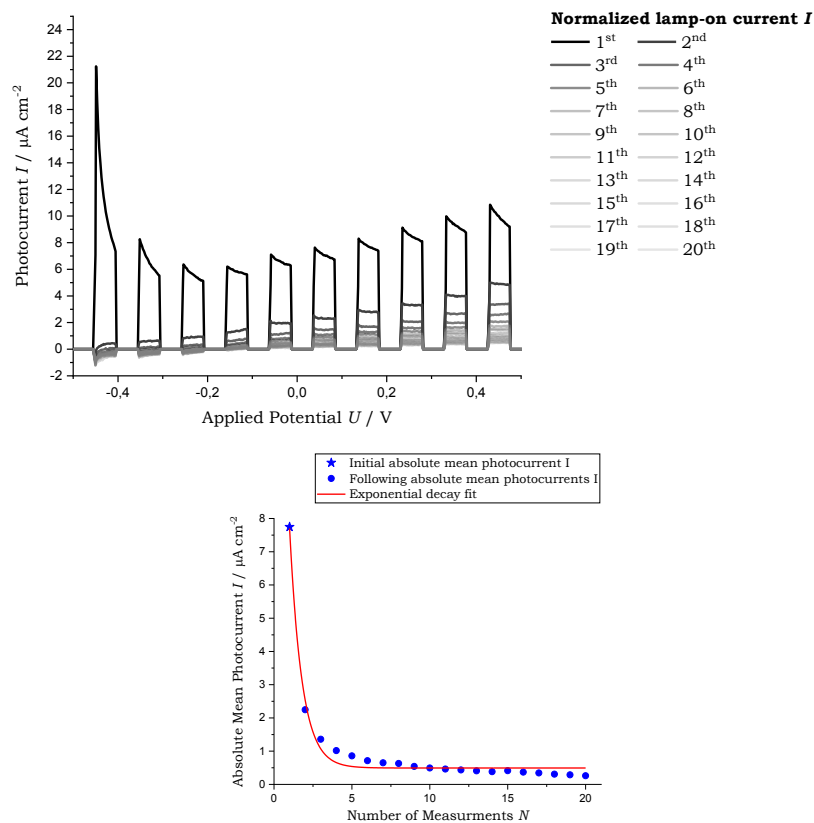


**Figure 87.** 20 times SPM of pure CdSe@CdS film (1.2 mg/mL spin coated solution) (top) and exponential decay fit of collected initial mean photocurrents (bottom) in chapter VII.3.1. *Sweeping potential measurement.*

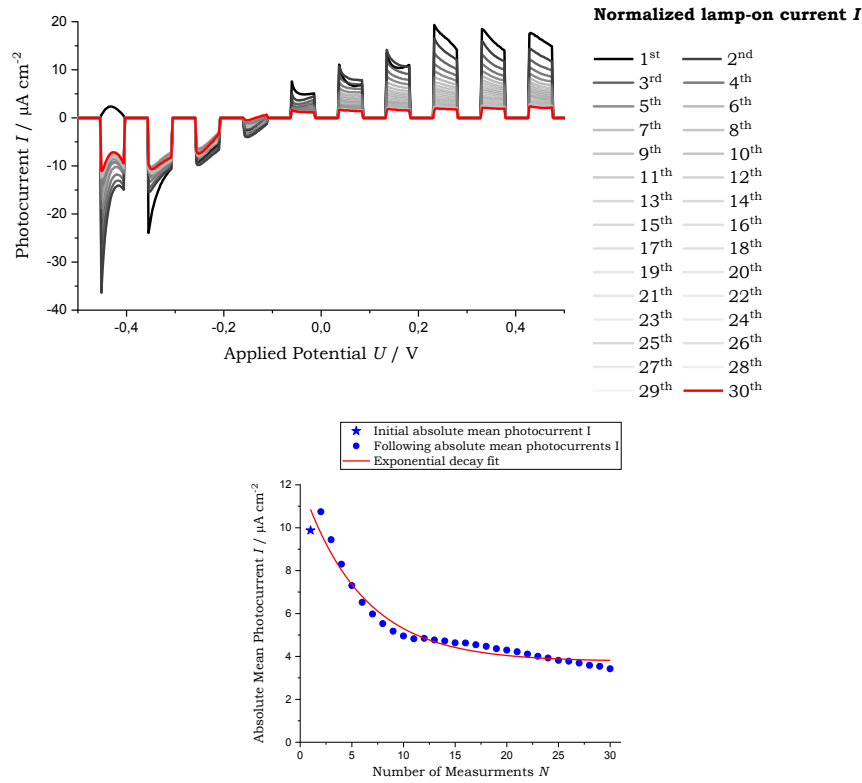


**Figure 88.** 30 times SPM of pure 5 cycle PDA film (top) and exponential decay fit of collected initial mean photocurrents (bottom) in chapter VII.3.1. *Sweeping potential measurement.*

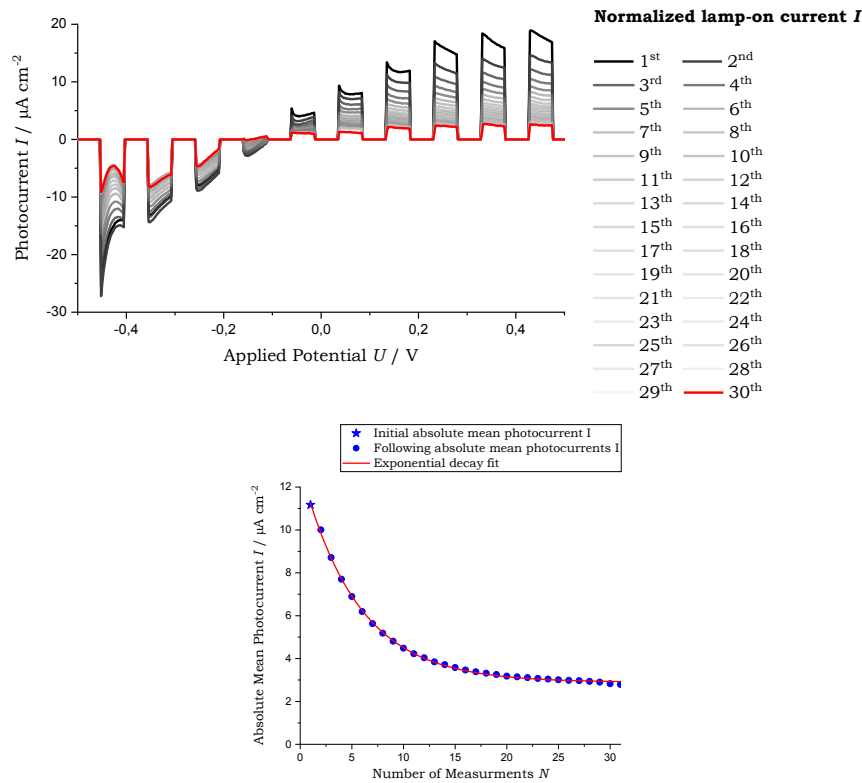


**Figure 89.** 30 times SPM of pure 45 cycle PDA film (top) and exponential decay fit of collected initial mean photocurrents (bottom) in chapter VII.3.1. *Sweeping potential measurement.*

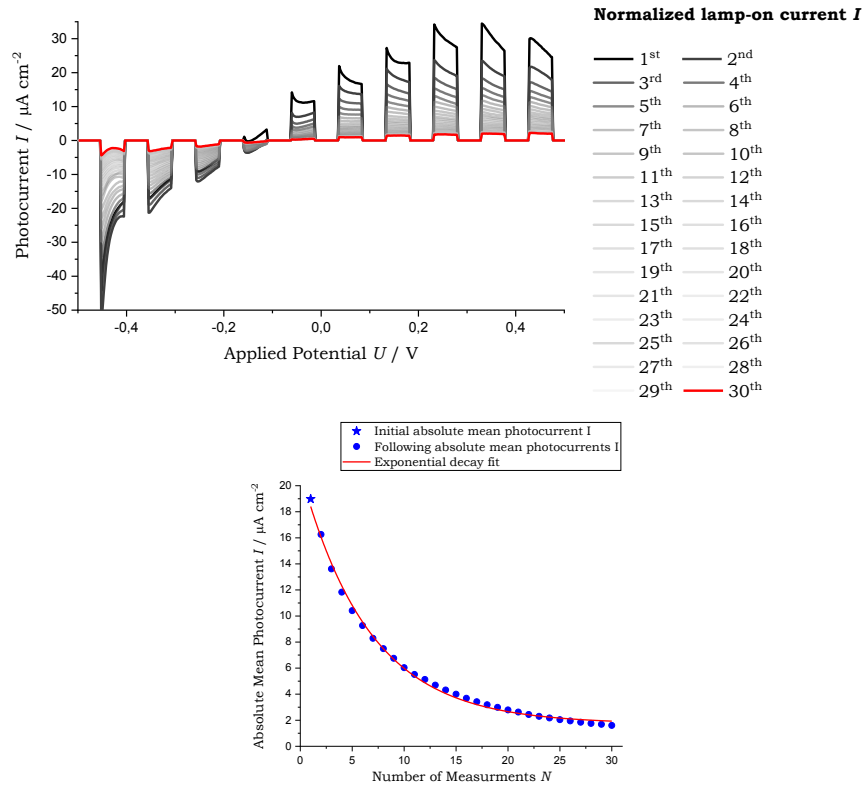


**Figure 90.** 30 times SPM of a 5 cycle PDA on 0.05 mg/mL spin coated CdSe@CdS nanorod solution (top) and exponential decay fit of initial mean photocurrents (bottom) in chapter VII.3.1. *Sweeping potential measurement.*

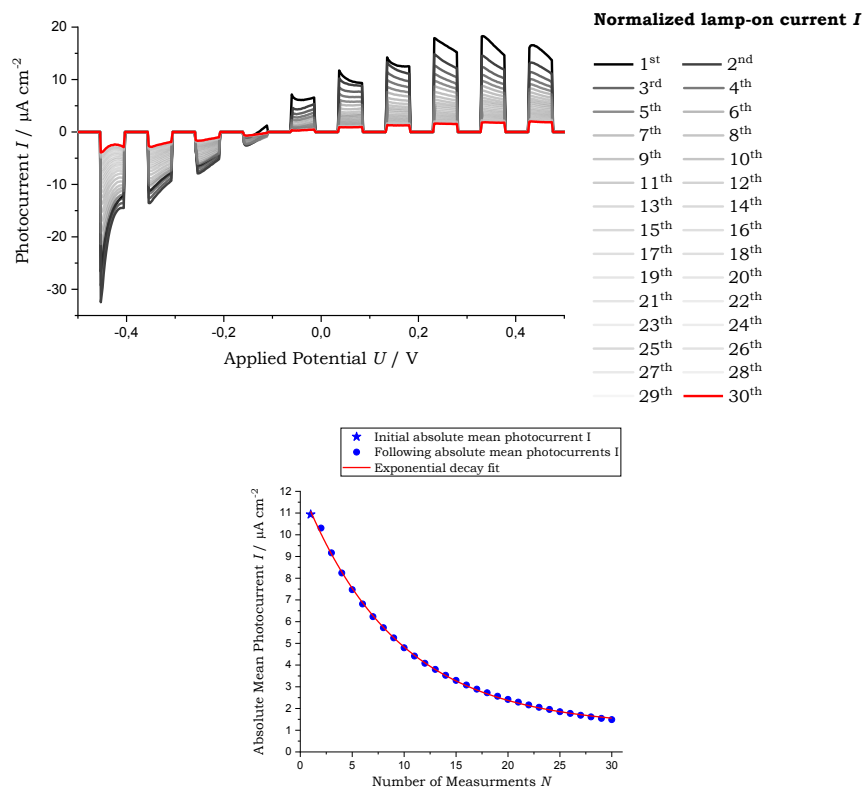


**Figure 91.** 30 times SPM of a 5 cycle PDA on 0.1 mg/mL spin coated CdSe@CdS nanorod solution (top) and exponential decay fit of initial mean photocurrents (bottom) in chapter VII.3.1. *Sweeping potential measurement.*



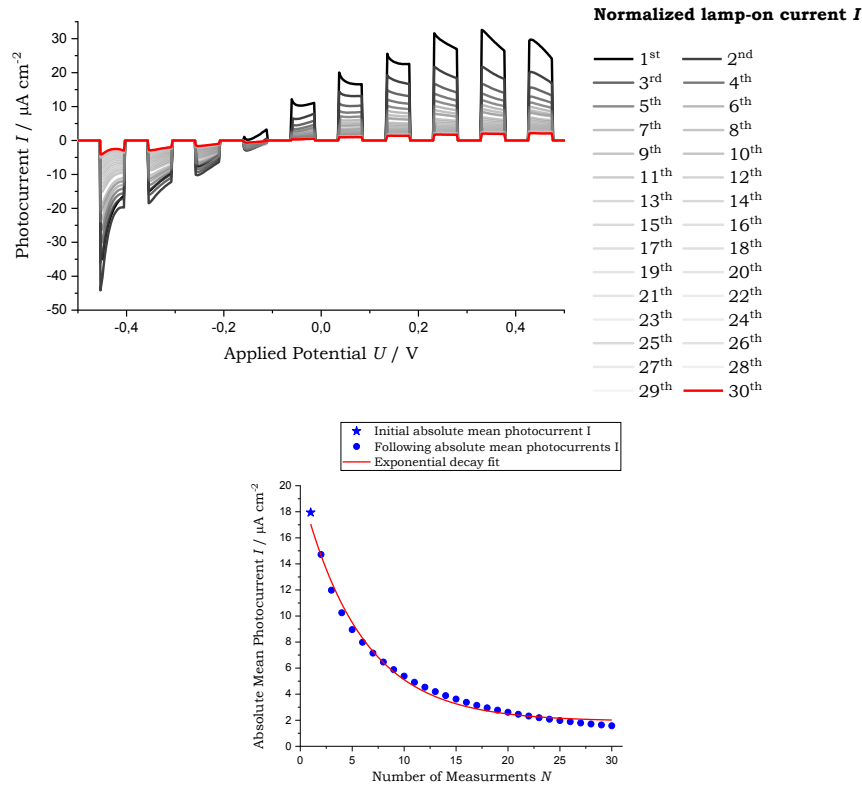


**Figure 92.** 30 times SPM of a 5 cycle PDA on 0.2 mg/mL spin coated CdSe@CdS nanorod solution (top) and exponential decay fit of initial mean photocurrents (bottom) in chapter VII.3.1. *Sweeping potential measurement.*

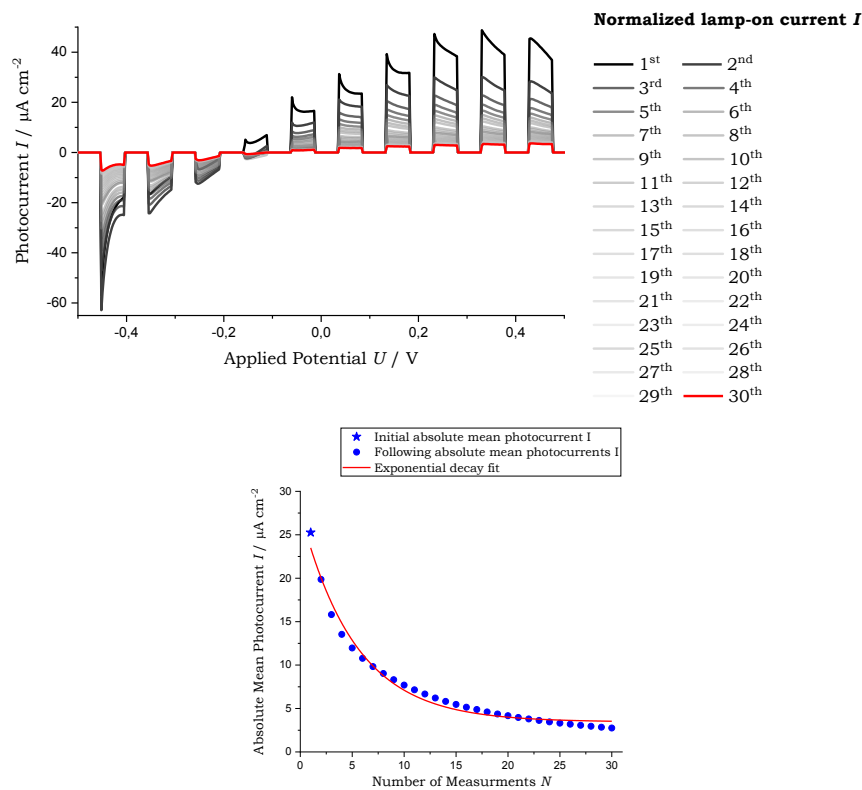


**Figure 93.** 30 times SPM of a 5 cycle PDA on 0.3 mg/mL spin coated CdSe@CdS nanorod solution (top) and exponential decay fit of initial mean photocurrents (bottom) in chapter VII.3.1. *Sweeping potential measurement.*

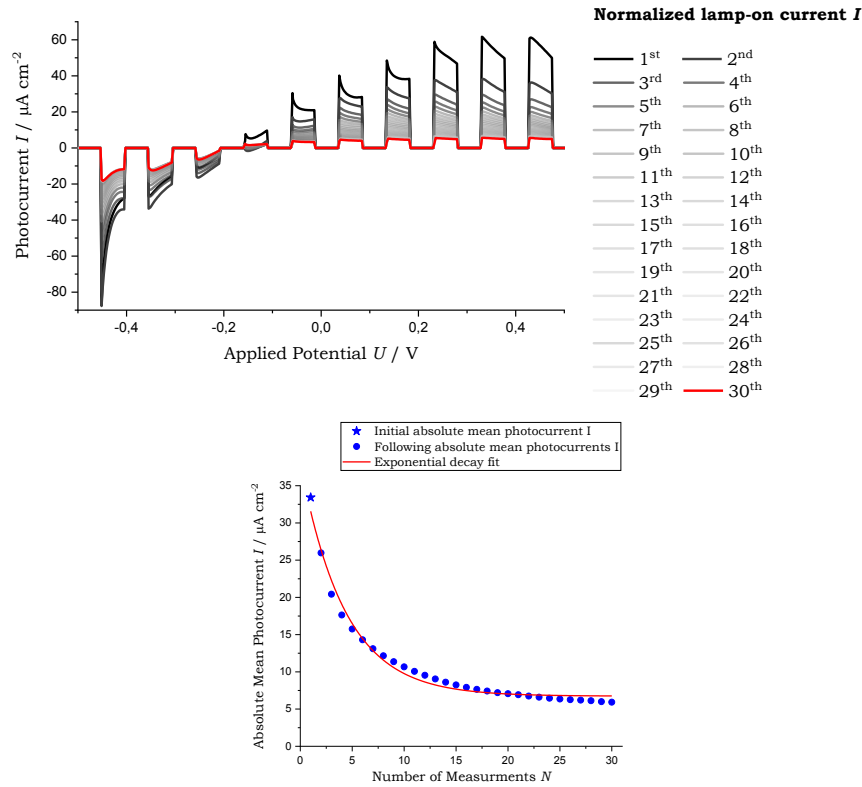


**Figure 94.** 30 times SPM of a 5 cycle PDA on 0.4 mg/mL spin coated CdSe@CdS nanorod solution (top) and exponential decay fit of initial mean photocurrents (bottom) in chapter VII.3.1. Sweeping potential measurement.

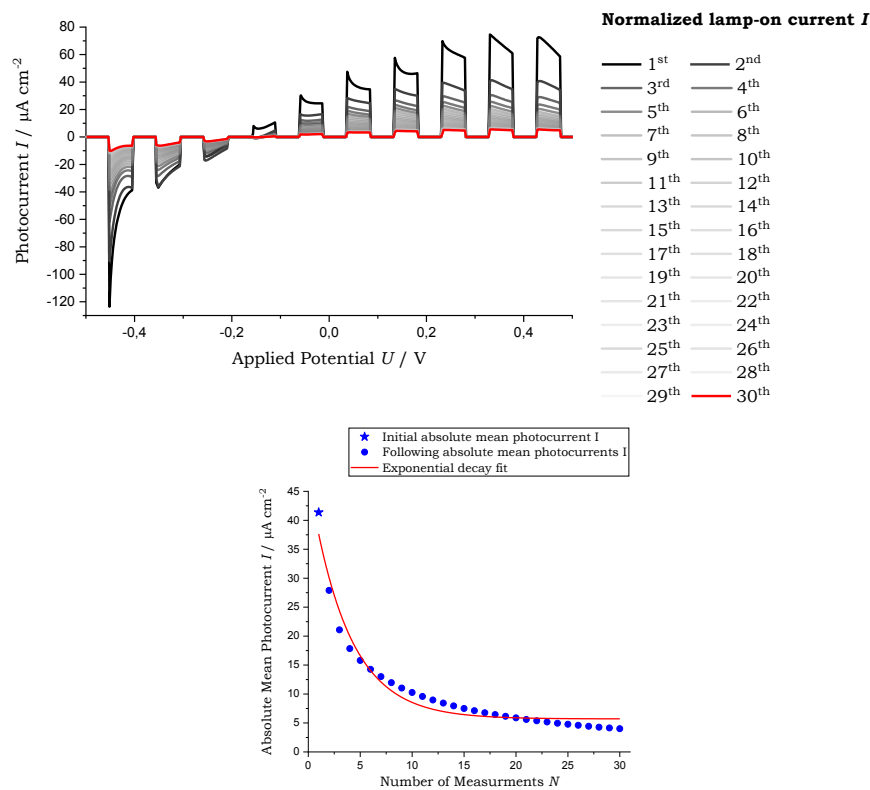


**Figure 95.** 30 times SPM of a 5 cycle PDA on 0.8 mg/mL spin coated CdSe@CdS nanorod solution (top) and exponential decay fit of initial mean photocurrents (bottom) in chapter VII.3.1. Sweeping potential measurement.

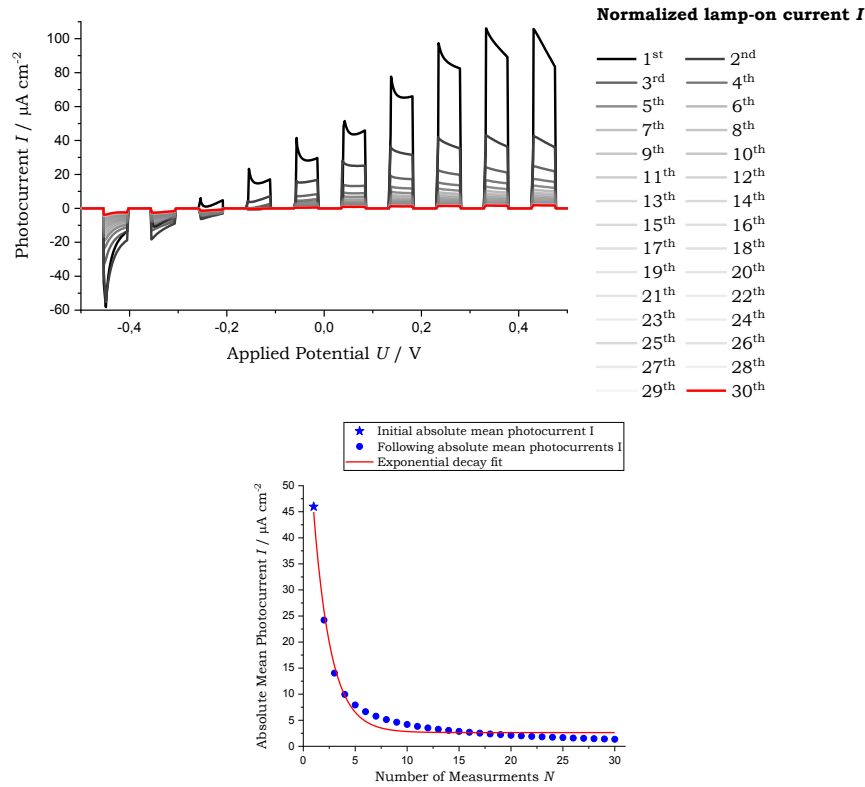


**Figure 96.** 30 times SPM of a 5 cycle PDA on 1.6 mg/mL spin coated CdSe@CdS nanorod solution (top) and exponential decay fit of initial mean photocurrents (bottom) in chapter VII.3.1. Sweeping potential measurement.

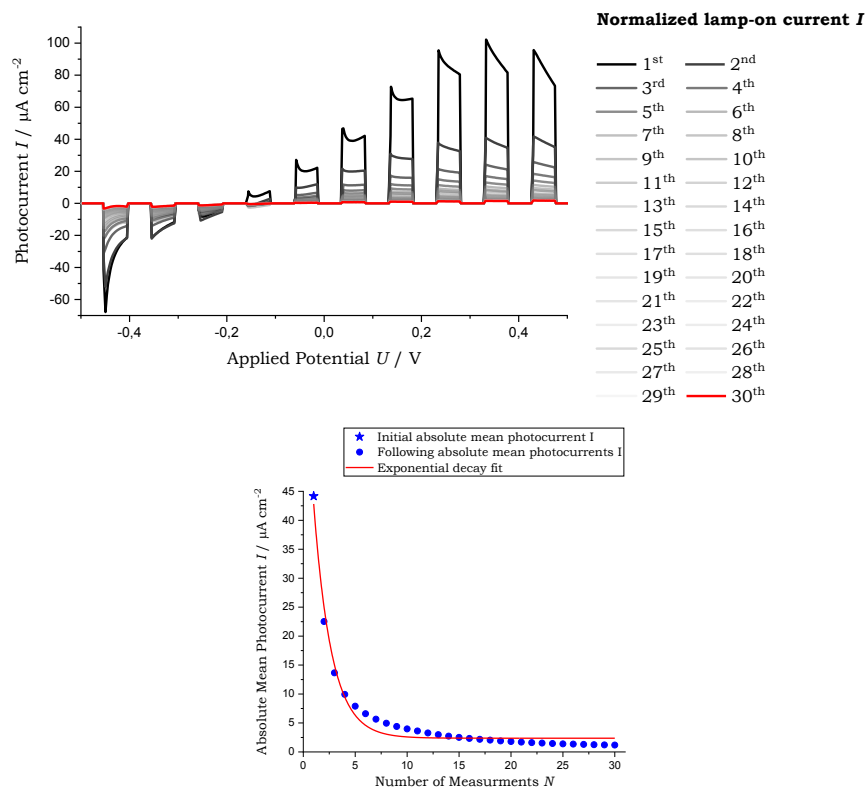


**Figure 97.** 30 times SPM of a 5 cycle PDA on 2.0 mg/mL spin coated CdSe@CdS nanorod solution (top) and exponential decay fit of initial mean photocurrents (bottom) in chapter VII.3.1. Sweeping potential measurement.

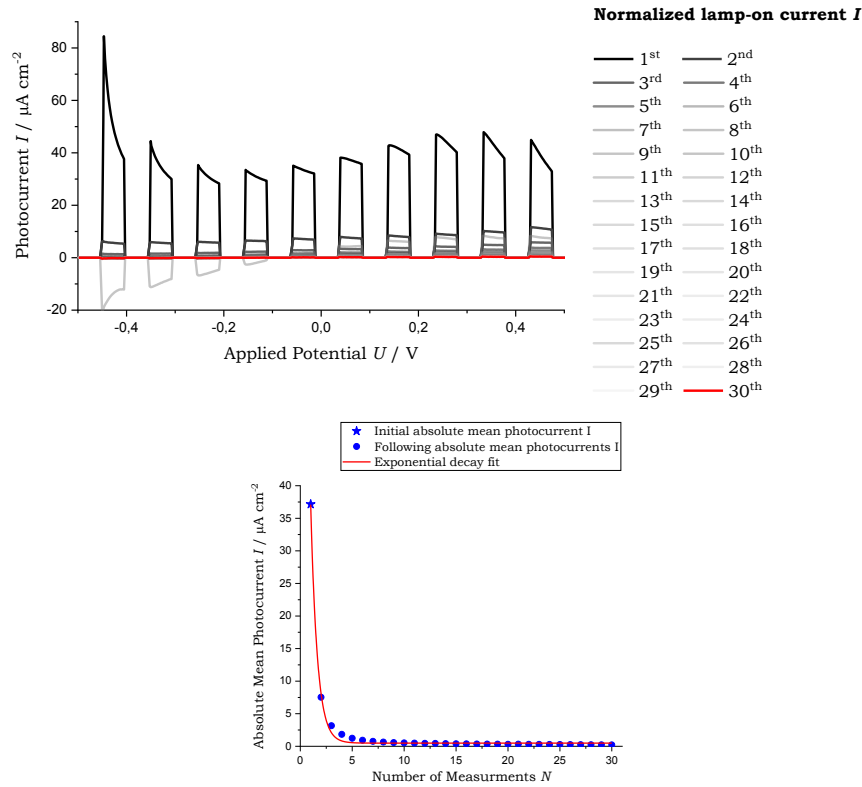


**Figure 98.** 30 times SPM of pure 1.2 mg/mL spin coated CdSe@CdS nanorod solution (top) and exponential decay fit of initial mean photocurrents (bottom) in chapter VII.3.1. *Sweeping potential measurement.*

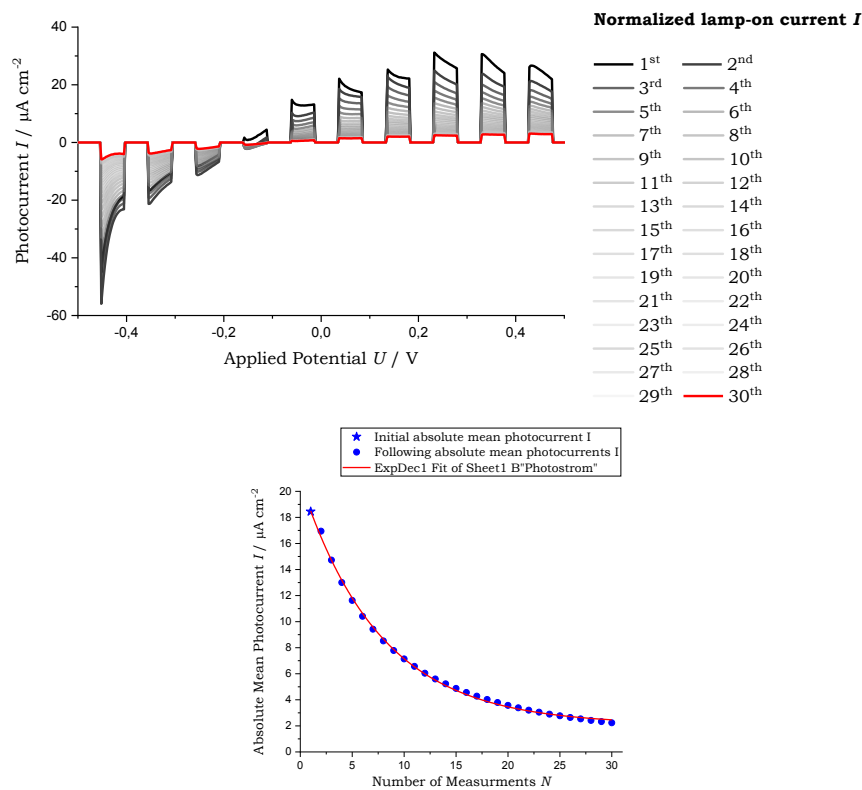


**Figure 99.** 30 times SPM of a pure 5 cycle PDA (top) and exponential decay fit of initial mean photocurrents (bottom) in chapter VII.3.1. *Sweeping potential measurement.*

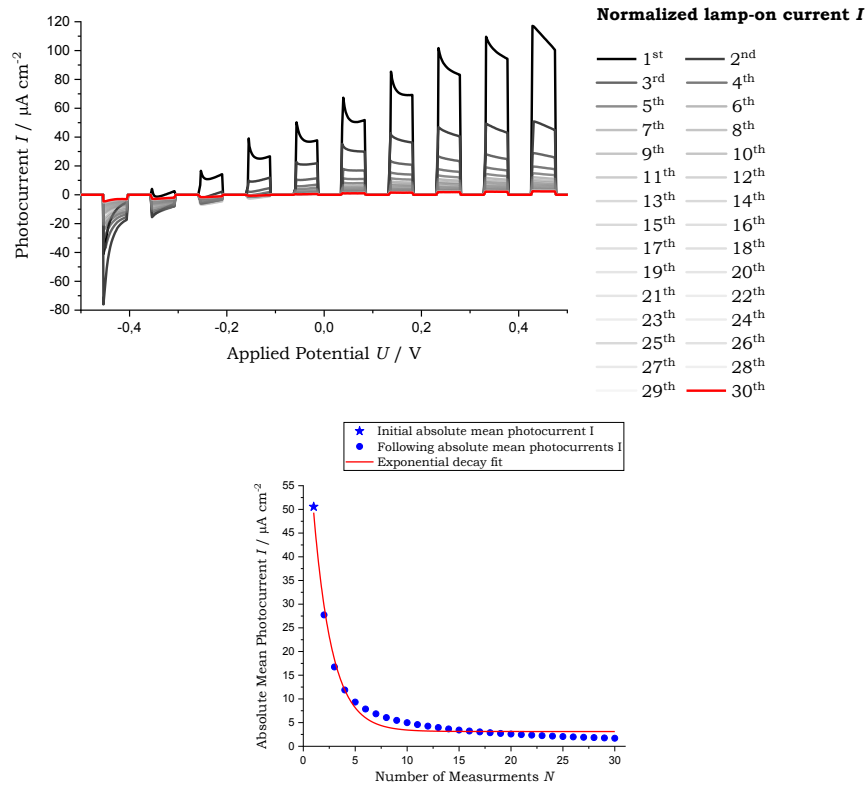


**Figure 100.** 30 times SPM of a 5 cycle PDA on 1.2 mg/mL spin coated CdSe@CdS nanorod solution (top) and exponential decay fit of initial mean photocurrents (bottom) in chapter VII.3.1. Sweeping potential measurement.

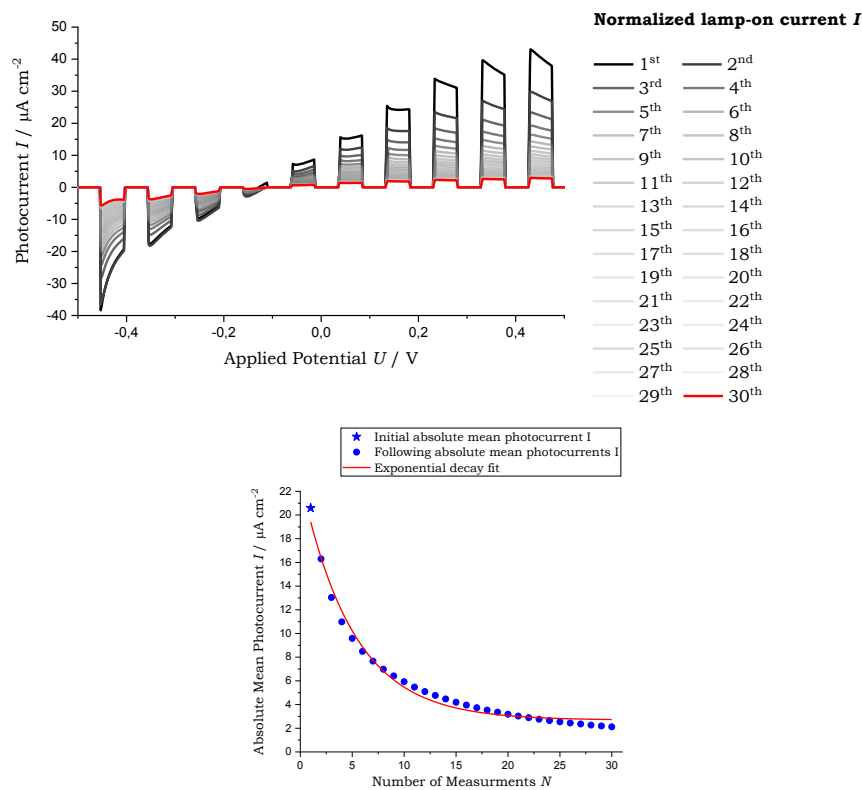


**Figure 101.** 30 times SPM of a 30 cycle PDA on 1.2 mg/mL spin coated CdSe@CdS nanorod solution (top) and exponential decay fit of initial mean photocurrents (bottom) in chapter VII.3.1. Sweeping potential measurement.

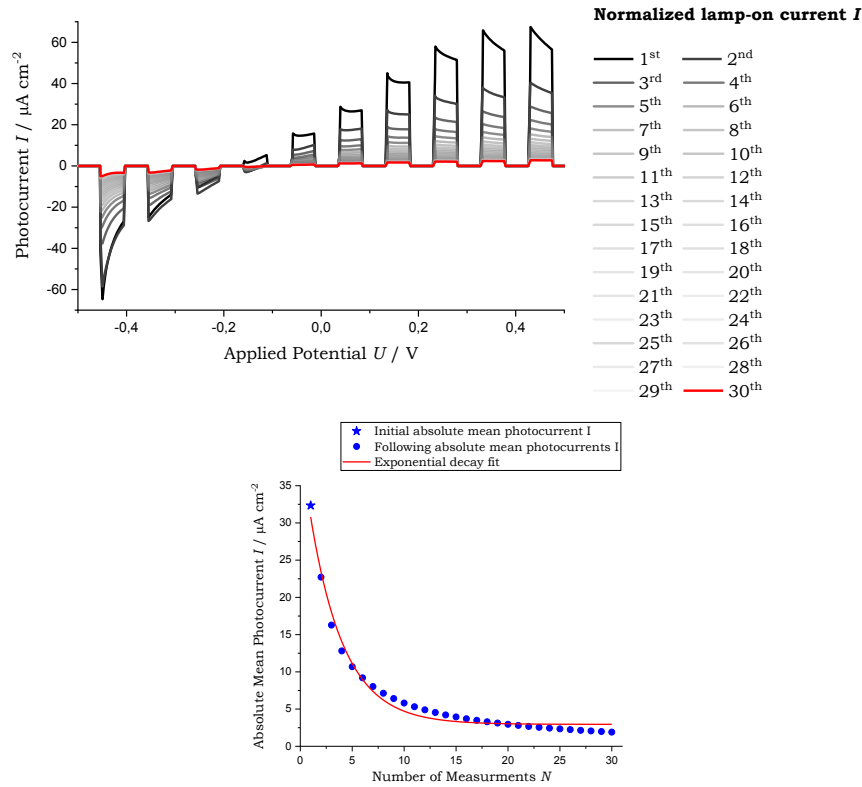


**Figure 102.** 30 times SPM of a 15 cycle PDA on 1.2 mg/mL spin coated CdSe@CdS nanorod solution (top) and exponential decay fit of initial mean photocurrents (bottom) in chapter VII.3.1. *Sweeping potential measurement.*

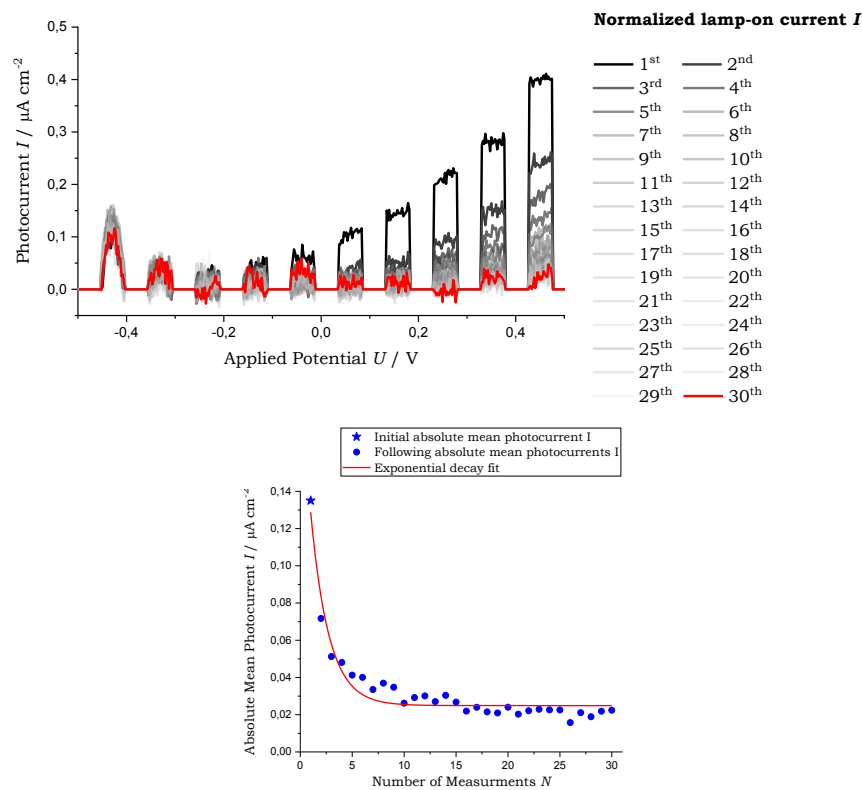


**Figure 103.** 30 times SPM of a pure ITO (top) and exponential decay fit of initial mean photocurrents (bottom) in chapter VII.3.1. *Sweeping potential measurement.*

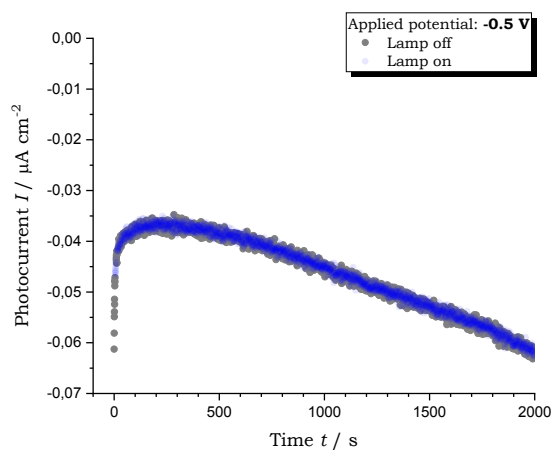


**Figure 104.** CPM of pure ITO at  $U = -0.5 \text{ V}$  in chapter VII.3.2. Constant potential measurement.

## XI. Table of Figures

|                                                                                                                                                                                                                                                                                                                                                                                                                                                                                                                                                                                  |    |
|----------------------------------------------------------------------------------------------------------------------------------------------------------------------------------------------------------------------------------------------------------------------------------------------------------------------------------------------------------------------------------------------------------------------------------------------------------------------------------------------------------------------------------------------------------------------------------|----|
| <b>Figure 1.</b> Schematic representation of <b>A.)</b> the desired system for hydrogen production, consisting of CdSe@CdS core-shell nanorod aligned perpendicular to an indium tin oxide (ITO) electrode supported by a thick glass layer. The nanorods are coated partially in polydopamine (PDA) and a catalyst is attached at the exposed tip. <b>B.)</b> In the current system the spin coated nanorods are distributed randomly and are therefore differently coated with PDA. ....                                                                                       | 5  |
| <b>Figure 2.</b> Schematical representation of the proposed mechanism for hydrogen production in the envisaged device. Spatially separated excitons, induced by light irradiation in the CdSe@CdS core-shell nanorods, can be used for proton reduction. H <sub>2</sub> production can be modulated by the supporting PDA film via pH regulations in order to quench electron holes and favor H <sub>2</sub> production (basic environment) or to self-recover and turn of H <sub>2</sub> production (acidic environment). ....                                                  | 5  |
| <b>Figure 3.</b> Overview of the most common hydrogen production methods by either thermochemical conversion from non-renewable fuels (94 % of worldwide hydrogen production) or by the electrolysis of water (4 % of worldwide hydrogen production). ....                                                                                                                                                                                                                                                                                                                       | 6  |
| <b>Figure 4.</b> Schematic representation of nanostructured hematite based tandem design of a photoelectrochemical water splitting cell coupled to a perovskite solar cell (PSC). <sup>[23]</sup> .....                                                                                                                                                                                                                                                                                                                                                                          | 7  |
| <b>Figure 5.</b> Schematic representation of a dual doped BiVO <sub>4</sub> based tandem structure of a photoelectrochemical water splitting cell coupled to a perovskite solar cell. <sup>[21]</sup> .....                                                                                                                                                                                                                                                                                                                                                                      | 8  |
| <b>Figure 6. A.)</b> Schematic representation of nanostructured Cu <sub>2</sub> O based tandem design of a photoelectrochemical water splitting cell. <b>B.)</b> Nanostructure of uncoated Cu <sub>2</sub> O resolved by scanning electron microscopy (cross section). ....                                                                                                                                                                                                                                                                                                      | 8  |
| <b>Figure 7. A.)</b> Self-assembly of carboxy-functionalized perylene monoimide chromophore amphiphile into ribbon-like structures. <b>B.)</b> Scanning electron microscopy image of the hydro gel formed after the incorporation of poly(diallyldimethylammonium) chloride as polyelectrolyte. ....                                                                                                                                                                                                                                                                             | 9  |
| <b>Figure 8. A.)</b> Simplified representation of photosystem II (PS II) in photosynthesis. Chlorophyll as a photosensitizer provides electrons to plastochinon. The reduced plastochinol transports the electrons through cytochrome b <sub>6</sub> f and plastocyanin into the photosystem I, where NADH <sup>+</sup> is reduced. <b>B.)</b> General compounds for a PS II inspired photocatalytic cell. Electrons are generated by a photosensitizer, transported to a redox mediator and transmitted through a complex electron transportation network to the catalyst. .... | 10 |
| <b>Figure 9. A.)</b> Simplified model of the envisaged photoelectrochemical cell. CdSe@CdS core-shell nanorods as photosensitizers provide electrons, which are transported to the tip of the NR and reduce hydrogen. <b>B.)</b> Simplified model of current device. Polydopamine (PDA) coated nanorods provide electrons, which travel through PDA to an attached catalyst for hydrogen production. Electron holes in the nanorods are quenched in both devices by redox mediative PDA. ....                                                                                    | 11 |
| <b>Figure 10.</b> Schematical representation of orbital/band energy levels for different types of materials. The band gap E <sub>g</sub> decreases with an increasing number of atoms N. ....                                                                                                                                                                                                                                                                                                                                                                                    | 14 |
| <b>Figure 11.</b> Band gap scheme of CdS and CdSe referring to the water splitting potentials against a normal hydrogen electrode (NHE). A quasi type-II electron-hole confinement is present due to different valence band and conduction band offset energies, $\Delta E_1 \gg \Delta E_2$ . ....                                                                                                                                                                                                                                                                              | 15 |
| <b>Figure 12.</b> Proposed formation mechanism <sup>[54][55]</sup> and structure <sup>[56][57]</sup> of polydopamine (for clarity the corresponding covalently bonded quinone products were disregarded). ....                                                                                                                                                                                                                                                                                                                                                                   | 17 |
| <b>Figure 13.</b> Cyclic voltammogram of a 30 Cycles PDA film, indicating a ECE mechanism. ....                                                                                                                                                                                                                                                                                                                                                                                                                                                                                  | 18 |



|                                                                                                                                                                                                                                                                                                                                                                                                                                                                                                       |    |
|-------------------------------------------------------------------------------------------------------------------------------------------------------------------------------------------------------------------------------------------------------------------------------------------------------------------------------------------------------------------------------------------------------------------------------------------------------------------------------------------------------|----|
| <b>Figure 14.</b> Dependency of the PDA film thickness $d$ and the number of CV cycles $N$ .....                                                                                                                                                                                                                                                                                                                                                                                                      | 18 |
| <b>Figure 15.</b> Dividing an electrical/galvanic cell into two theoretical half-cells, connected via a salt bridge.....                                                                                                                                                                                                                                                                                                                                                                              | 19 |
| <b>Figure 16.</b> Schematic representation of the electron transfer (ET) between an agent and the electrode, where the electron energy at the electrode can be adjusted by an applied potential $U$ . Increasing the potential $U$ at an electrode favors an electron uptake, while decreasing $U$ favors an electron donation. ....                                                                                                                                                                  | 19 |
| <b>Figure 17.</b> Formation of an electrical double at an electrode. ....                                                                                                                                                                                                                                                                                                                                                                                                                             | 20 |
| <b>Figure 18.</b> General set up of cyclic voltammetry. ....                                                                                                                                                                                                                                                                                                                                                                                                                                          | 22 |
| <b>Figure 19.</b> Representation of the electron transfer (ET) process controlled by an applied potential $U$ . The CV curve is showing the oxidation/reduction of 12 mM $K_4[Fe^{II}_2(CN)_6]$ / $K_3[Fe^{III}_3(CN)_6]$ in phosphate buffer (pH = 7). ....                                                                                                                                                                                                                                          | 23 |
| <b>Figure 20.</b> CV curve of $N_2$ saturated (blue), air saturated (red), $[CoCp(dppe)(CH_3CN)][PF_6]_2$ with $N_2$ saturated (green) and air saturated (orange) electrolyte (0.25 M $[NBu_4][PF_6]$ , $CH_3CN$ solution, 100 mV/s scan rate, 3 mm glassy carbon WE, 3 mm glassy carbon CE, silver wire pseudo-RE). <sup>[64]</sup> .....                                                                                                                                                            | 23 |
| <b>Figure 21.</b> Cyclic voltammograms of 30 CV cycle PDA films. <b>A.)</b> In regular atmosphere (RA film). <b>B.)</b> Under Nitrogen atmosphere ( $N_2$ film).....                                                                                                                                                                                                                                                                                                                                  | 25 |
| <b>Figure 22.</b> Schematical representation of the higher oxygen concentration at the water/air interface due to the meniscus. ....                                                                                                                                                                                                                                                                                                                                                                  | 26 |
| <b>Figure 23. A.)</b> Overlay of initial CV curve for PDA films placed in different pH buffers. Red: 0.1 M acetyl buffer pH = 3.99 (Film A), green: 0.1 M phosphate buffer pH = 7.01 (Film B) and blue: 0.1 M ammonium buffer pH = 10.32 (Film C). <b>B.)</b> CV of a PDA film in neutral buffer. Potential sweeps from $-0.5$ V to $+1.5$ V and reveals two anodic peaks ( $p_{a,1}$ , $p_{a,2}$ ) for the 1 <sup>st</sup> cycle.....                                                                | 27 |
| <b>Figure 24.</b> CV curve of three different 5 Cycle PDA film in <b>A.)</b> acidic pH (phosphate buffer), <b>B.)</b> neutral pH (ammonium buffer), <b>C.)</b> basic pH (acetyl buffer). The first row shows all cycles, while the second row highlights the first and fifth cycle to the corresponding film. ....                                                                                                                                                                                    | 28 |
| <b>Figure 25.</b> Overlay of CV curves for pretreated PDA Films via an applied potential (green: none, red: $-0.4$ V for 5 minutes, blue: $+0.4$ V for 5 minutes).....                                                                                                                                                                                                                                                                                                                                | 29 |
| <b>Figure 26.</b> Masked areas (grey) of a cyclic voltammogram for the peaks of a 5 cycle PDA film after applying a potential of $+0.4$ V for 5 minutes. Areas were calculated according to a baseline at 0 A (red). <b>A.)</b> The reduction peak area was calculated by subtraction of masked areas in <b>A1</b> und <b>A2</b> . <b>B.)</b> The oxidation peak area was calculated by subtraction of the masked areas in <b>B1</b> und <b>B2</b> . Charge current was disregarded. ....             | 30 |
| <b>Figure 27.</b> Masked areas (grey) of a cyclic voltammogram for the peaks of a 5 cycle PDA film after applying a potential of $-0.4$ V for 5 minutes. Areas were calculated according to a baseline at 0 A (red). <b>A.)</b> The reduction peak area was calculated by the subtraction of the masked areas in <b>A1</b> und <b>A2</b> . <b>B.)</b> The oxidation peak area was calculated by the subtraction of the masked areas in <b>B1</b> und <b>B2</b> . Charge current was disregarded. .... | 30 |
| <b>Figure 28.</b> Illustration of the electrochemical double layer at <b>A.)</b> $U = +0.4$ V with an electron transfer at the ITO/PDA interface and <b>B.)</b> $U = -0.4$ V without an electron transfer at the ITO/PDA interface. ....                                                                                                                                                                                                                                                              | 32 |
| <b>Figure 29.</b> New 3D design of the cuvette holder (left) and the cuvette cap (right). Designed via OnShape CAD.....                                                                                                                                                                                                                                                                                                                                                                               | 34 |
| <b>Figure 30.</b> Final experimental set up for the photocurrent measurements, containing the power supply (PS) for the lamp and for the shutter as well as the UV lamp for irradiation, a lens to                                                                                                                                                                                                                                                                                                    |    |

|                                                                                                                                                                                                                                                                                                                                                                                                                                                                                                                                             |           |
|---------------------------------------------------------------------------------------------------------------------------------------------------------------------------------------------------------------------------------------------------------------------------------------------------------------------------------------------------------------------------------------------------------------------------------------------------------------------------------------------------------------------------------------------|-----------|
| <i>focus a 5 mm diameter light cone and a shutter to enable/disable irradiation. Highlighted is the designed cuvette holder and the corresponding cuvette (cap) showing the minimized distance between CE/RE and WE. ....</i>                                                                                                                                                                                                                                                                                                               | <i>34</i> |
| <b>Figure 32.</b> TEM image of CdSe@CdS nanorods. Length $l = (46 \pm 4)$ nm, width $w = (5.2 \pm 0.6)$ nm. ....                                                                                                                                                                                                                                                                                                                                                                                                                            | <i>35</i> |
| <b>Figure 31.</b> HR-TEM (left) and TEM (right) images of CdSe@CdS nanorods. Length $l = (13 \pm 1)$ nm, width $w = (3 \pm 0.4)$ nm. ....                                                                                                                                                                                                                                                                                                                                                                                                   | <i>35</i> |
| <b>Figure 33.</b> Data processing for the sweeping potential measurement (SPM). <b>A.)</b> Raw Data. Current curves for the lamp on/off times. <b>B.)</b> Interpolated lamp-off curve (Baseline). <b>C.)</b> Subtracted Baseline leads to the absolute mean photocurrent $I$ . <b>D.)</b> Exponential decay fit of the absolute mean photocurrents $I$ . Highlighted is the initial absolute mean photocurrent $I_i$ . ....                                                                                                                 | <i>36</i> |
| <b>Figure 34.</b> On WE (ITO) spin coated nanorod concentration series for 5 CV cycle PDA films. The nanorod concentration $c$ is plotted against the calculated initial absolute mean photocurrent $I_i$ and the half-life $\tau$ . ....                                                                                                                                                                                                                                                                                                   | <i>37</i> |
| <b>Figure 35.</b> A comparison of a spin coated nanorod concentration of 1.2 mg/mL for different numbers of PDA cycles relative to pure ITO, pure nanorods (1.2 mg/mL) and pure PDA (5 cycles). ....                                                                                                                                                                                                                                                                                                                                        | <i>38</i> |
| <b>Figure 36. A.)</b> Comparison of photoelectric properties (photocurrent and half-life) between pure ITO, pure nanorods (1.2 mg/mL), pure 5 cycle PDA film and a combined film. <b>B.)</b> Comparison of photoelectric properties between long $[(46 \pm 4) \times (5.2 \pm 0.6)$ nm] and short nanorods: $[(13 \pm 1) \times (3 \pm 0.4)$ nm]. ....                                                                                                                                                                                      | <i>39</i> |
| <b>Figure 37.</b> Photoluminescence of pure CdSe@CdS core-shell nanorods (quantum yield: 30.7 %) compared to PDA coated nanorod particles (quantum yield: 0.1 %). The measurements was performed by the Wächtler group (Dr. Mathias Micheel) at Leibniz-IPHT for PDA coated nanorod particles. ....                                                                                                                                                                                                                                         | <i>40</i> |
| <b>Figure 38.</b> Transient absorption spectroscopy (TAS) data. <b>A.)</b> Differential Absorbance $\Delta A$ of PDA coated CdSe@CdS nanorods in the wavelength range of 380 – 600 nm for different delay times (10 ps: light blue, 100 ps: blue, 1000 ps: dark blue). <b>B.)</b> Normalized $\Delta A$ for single CdS (at 460 nm) and CdSe (at 560 nm) peaks of PDA coated and pure nanorods plotted against the delay time (approaching 1000 ps). TAS was performed by the Wächtler group (Dr. Mathias Micheel) at the Leibniz-IPHT. .... | <i>41</i> |
| <b>Figure 39.</b> Data processing for the constant potential measurement (CPM). <b>A.)</b> Raw Data. Current curves for the lamp on/off times. <b>B.)</b> Interpolated lamp-off curve (Baseline). <b>C.)</b> Subtracted Baseline leads to the actual lamp on photocurrent curve $I$ . <b>D.)</b> Integration finally leads to the actual photocurrent as $\mu A \cdot cm - 2 \cdot s$ . Grey highlighted is the corresponding area. ....                                                                                                    | <i>42</i> |
| <b>Figure 40.</b> Applied asymptote fit equation (6) on the lamp on curve. ....                                                                                                                                                                                                                                                                                                                                                                                                                                                             | <i>42</i> |
| <b>Figure 41.</b> Constant potential $U$ photocurrent measurements (CPM) $+ 0.1 V \leq U \leq + 0.5 V$ at 5 cycle PDA films for 2000 seconds. Blue curves indicate lamp-on times, while grey curves indicate lamp-off times. <b>A.)</b> 0.1 V applied potential. <b>B.)</b> 0.2 V applied potential. <b>C.)</b> 0.3 V applied potential. <b>D.)</b> 0.4 V applied potential. <b>E.)</b> 0.5 V applied potential. ....                                                                                                                       | <i>43</i> |
| <b>Figure 42.</b> Summarized results of the lamp-on photocurrent $I_{on}$ and the lamp-on asymptote $A_{on}$ by constant potential $U$ photocurrent measurements (CPM) at $+ 0.1 V \leq U \leq + 0.5 V$ of a 5 cycle PDA film. ....                                                                                                                                                                                                                                                                                                         | <i>44</i> |
| <b>Figure 43.</b> Constant potential $U$ photocurrent measurements (CPM) $OCP \leq U \leq - 0.5 V$ of 5 cycle PDA films for 2000 seconds. Blue curves indicate lamp-on times, while grey curves indicate lamp-off times. <b>A.)</b> $- 0.027 V$ (OCP) applied potential. <b>B.)</b> 0.1 V applied potential. <b>C.)</b> 0.2 V applied potential. <b>D.)</b> 0.3 V applied potential. <b>E.)</b> 0.4 V applied potential. <b>F.)</b> 0.5 V applied potential. ....                                                                           | <i>45</i> |

|                                                                                                                                                                                                                                                                                                                                                                                                                                                                  |    |
|------------------------------------------------------------------------------------------------------------------------------------------------------------------------------------------------------------------------------------------------------------------------------------------------------------------------------------------------------------------------------------------------------------------------------------------------------------------|----|
| <b>Figure 44.</b> Summarized results of the lamp-on photocurrent $I_{on}$ and the lamp-on asymptote $A_{on}$ by constant potential $U$ photocurrent measurements at $-0.1 V \leq U \leq -0.5 V$ of a 5 cycle PDA film. ....                                                                                                                                                                                                                                      | 46 |
| <b>Figure 45.</b> Constant potential photocurrent measurements (CPM) at $-0.5 V$ of 5 cycle PDA films for 2000 seconds with a hole scavenger. <b>A.)</b> No hole scavenger. <b>B.)</b> Methanol. <b>C.)</b> Ascorbic acid. <b>D.)</b> Sodium ascorbate. <b>E.)</b> Sodium sulfite. ....                                                                                                                                                                          | 47 |
| <b>Figure 46.</b> Summarized results of the lamp-on photocurrent $I_{on}$ and the lamp-on asymptote $A_{on}$ for different hole scavengers (methanol, ascorbic acid, sodium ascorbate, sodium sulfite) collected by constant potential photocurrent measurements at $-0.5 V$ of a 5 cycle PDA film. ....                                                                                                                                                         | 48 |
| <b>Figure 47.</b> Constant potential $U$ photocurrent measurements (CPM) $-0.1 V \geq U \geq -0.5 V$ at spin coated nanorod films (0.8 mg/mL) for 2000 seconds. Blue curves indicate lamp-on times, while grey curves indicate lamp-off times. <b>A.)</b> 0.1 V applied potential. <b>B.)</b> 0.2 V applied potential. <b>C.)</b> 0.3 V applied potential. <b>D.)</b> 0.4 V applied potential. <b>E.)</b> 0.5 V applied potential. ....                          | 49 |
| <b>Figure 48.</b> Summarized results of the lamp-on photocurrent $I_{on}$ and the lamp-on asymptote $A_{on}$ by constant potential $U$ photocurrent measurements at $-0.1 V \leq U \leq -0.5 V$ of pure nanorods films (0.8 mg/mL spin coated). ....                                                                                                                                                                                                             | 50 |
| <b>Figure 49.</b> Constant potential $U$ photocurrent measurements (CPM) at $-0.5 V$ of pure nanorod films (0.8 mg/mL spin coated) for 2000 seconds with additional hole scavenger. <b>A.)</b> No hole scavenger. <b>B.)</b> Methanol. <b>C.)</b> Ascorbic acid. <b>D.)</b> Sodium ascorbate. <b>E.)</b> Sodium sulfite. ....                                                                                                                                    | 51 |
| <b>Figure 50.</b> Summarized results of the lamp-on photocurrent $I_{on}$ and the lamp-on asymptote $A_{on}$ for different hole scavengers (methanol, ascorbic acid, sodium ascorbate, sodium sulfite) collected by constant potential photocurrent measurements at $-0.5 V$ of pure nanorods films (0.8 mg/mL spin coated). ....                                                                                                                                | 52 |
| <b>Figure 51.</b> Constant potential $U$ photocurrent measurements (CPM) $-0.1 V \geq U \geq -0.5 V$ of combined films (5 cycles PDA + 0.8 mg/mL spin coated nanorods) for 2000 seconds. Blue curve indicated lamp-on times, while grey curve indicated lamp-off times. <b>A.)</b> 0.1 V applied potential. <b>B.)</b> 0.2 V applied potential. <b>C.)</b> 0.3 V applied potential. <b>D.)</b> 0.4 V applied potential. <b>E.)</b> 0.5 V applied potential. .... | 53 |
| <b>Figure 52.</b> Summarized results of the lamp-on photocurrent $I_{on}$ and the lamp-on asymptote $A_{on}$ by constant potential $U$ photocurrent measurements at $-0.1 V \leq U \leq -0.5 V$ of combined films (5 cycles PDA + 0.8 mg/mL spin coated nanorods). ....                                                                                                                                                                                          | 54 |
| <b>Figure 53.</b> Constant potential $U$ photocurrent measurements (CPM) at $-0.5 V$ of combined films (5 cycles PDA + 0.8 mg/mL spin coated nanorods) for 2000 seconds with additional hole scavenger. <b>A.)</b> No hole scavenger. <b>B.)</b> Methanol. <b>C.)</b> Ascorbic acid. <b>D.)</b> Sodium ascorbate. <b>E.)</b> Sodium sulfite. ....                                                                                                                | 55 |
| <b>Figure 54.</b> Summarized results of the lamp-on photocurrent $I_{on}$ and the lamp-on asymptote $A_{on}$ for different hole scavengers (methanol, ascorbic acid, sodium ascorbate, sodium sulfite) collected by constant potential photocurrent measurements at $-0.5 V$ of combined films (5 cycles PDA + 0.8 mg/mL spin coated nanorods). ....                                                                                                             | 56 |
| <b>Figure 55.</b> General procedure to produce ultra-smooth ITO. First, Si-wafer are oxygen plasma treated, followed by the bonding of the self assembles monolayer (SAM). ITO sputtering on the hydrophobic surface, followed by gluing glass on the surface complete the layers. Removing the wafer should separate the layers at the weakest interface (ITO/SAM) leading to ultra-smooth ITO. ....                                                            | 58 |
| <b>Figure 56.</b> General set-up for the chemical vapor deposition of 1,1,1,3,3,3-Hexamethyldisilazane. Nitrogen is dried over a $CaCl_2$ column and bubbles into the silizane solution. The vapor flows into a petri dish preprocessed with three holes (inlet, outlet, thermostat sensor) at $120^\circ C$ in which the Si-wafer is placed. ....                                                                                                               | 59 |

|                                                                                                                                                                                                                                                                                              |    |
|----------------------------------------------------------------------------------------------------------------------------------------------------------------------------------------------------------------------------------------------------------------------------------------------|----|
| <b>Figure 57.</b> Formation of self-assembles monolayer on silicon wafers by <b>A.)</b> Trimethoxy(octadecyl)silane (ODTMS), Triethoxy(3,3,4,4,5,5,6,6,7,7,8,8,8-tridecafluorooctyl)silane (TEFOS) and <b>B.)</b> 1,1,1,3,3,3-Hexamethyldisilazane (HMDS). .....                             | 59 |
| <b>Figure 58.</b> AFM picture of <b>A.)</b> non-functionalized silicon wafer after oxygen plasma treatment and SAM-functionalized silicon wafer by <b>B.)</b> ODTMS, <b>C.)</b> TEFOS and <b>D.)</b> HMDS. <b>E.)</b> ITO surface collected from HMDS functionalized silicon wafer. ....     | 61 |
| <b>Figure 59.</b> Cyclic voltammograms of polydopamine polymerization on ITO with <b>A.)</b> 8 – 12 $\Omega$ and <b>B.)</b> 300 $\Omega$ resistance. <b>C.)</b> Cyclic voltammogram of polydopamine polymerization on self-made ITO electrode with a resistance of 800 – 100 $\Omega$ . .... | 62 |
| <b>Figure 60.</b> Cyclic voltammetric cycles of PDA-co-PPY formation on a gold WE ( <b>A</b> ) and ITO WE ( <b>B</b> ) indicate an increase in the conductivity of the resulting film. ....                                                                                                  | 64 |
| <b>Figure 61.</b> SEM picture of embedded CdSe@CdS nanorods (1.2 mg/mL spin coated solution) embedded in 5 cycles PDA on an indium tin oxide electrode. Scale: 100 nm. ....                                                                                                                  | 69 |
| <b>Figure 62.</b> SEM picture of embedded CdSe@CdS nanorods (1.2 mg/mL spin coated solution) embedded in 5 cycles PDA on indium tin oxide electrode. Scale: 500 nm. ....                                                                                                                     | 69 |
| <b>Figure 63.</b> SEM picture of embedded CdSe@CdS nanorods (1.2 mg/mL spin coated solution) embedded in 5 cycles PDA on indium tin oxide electrode after irradiation and degradation of the nanorods. Resolution: 500 nm. ....                                                              | 70 |
| <b>Figure 64.</b> Comparison of 5 and 45 cycle PDA film regarding to the half-life and initial mean photocurrent while irradiation. Data were collected with the old set-up similar to Figure 18. ....                                                                                       | 70 |
| <b>Figure 65.</b> Cyclic voltammogram of 5 cycle PDA film used for acidic pH treatment (left) and basic pH treatment (right) in chapter VII.1.2. Redox behavior: Controllability of catechol/quinone ratio. ....                                                                             | 71 |
| <b>Figure 66.</b> Cyclic voltammogram of 5 cycle PDA film used for neutral pH treatment (left) and applied potential treatment (right) in chapter VII.1.2. Redox behavior: Controllability of catechol/quinone ratio. ....                                                                   | 71 |
| <b>Figure 67.</b> Cyclic voltammogram of 5 cycle PDA film (left) and 45 cycle PDA film (right) used for CPM in chapter VII.3.1. Sweeping potential measurement ( $\rightarrow$ Figure 64). ....                                                                                              | 71 |
| <b>Figure 68.</b> Cyclic voltammogram of 5 cycle PDA film on 0.05 mg/mL spin coated CdSe@CdS solution (left) and 0.1 mg/mL spin coated CdSe@CdS solution (right) used for CPM in chapter VII.3.1. Sweeping potential measurement. ....                                                       | 72 |
| <b>Figure 69.</b> Cyclic voltammogram of 5 cycle PDA film on 0.2 mg/mL spin coated CdSe@CdS solution (left) and 0.3 mg/mL spin coated CdSe@CdS solution (right) used for CPM in chapter VII.3.1. Sweeping potential measurement. ....                                                        | 72 |
| <b>Figure 70.</b> Cyclic voltammogram of 5 cycle PDA film on 0.4 mg/mL spin coated CdSe@CdS solution (left) and 0.8 mg/mL spin coated CdSe@CdS solution (right) used for CPM in chapter VII.3.1. Sweeping potential measurement. ....                                                        | 72 |
| <b>Figure 71.</b> Cyclic voltammogram of 5 cycle PDA film on 1.6 mg/mL spin coated CdSe@CdS solution (left) and 2.0 mg/mL spin coated CdSe@CdS solution (right) used for CPM in chapter VII.3.1. Sweeping potential measurement. ....                                                        | 73 |
| <b>Figure 72.</b> Cyclic voltammogram of pure 5 cycle PDA film (left) and with 1.2 mg/mL spin coated CdSe@CdS solution (right) used for CPM in chapter VII.3.1. Sweeping potential measurement. ....                                                                                         | 73 |
| <b>Figure 73.</b> Cyclic voltammogram of pure 5 cycle PDA film used for CPM at $U = 0.3$ V (left) and $U = 0.4$ V in chapter VII.3.2. Constant potential measurement. ....                                                                                                                   | 73 |

|                                                                                                                                                                                                                                                                                |    |
|--------------------------------------------------------------------------------------------------------------------------------------------------------------------------------------------------------------------------------------------------------------------------------|----|
| <b>Figure 74.</b> Cyclic voltammogram of pure 5 cycle PDA film used for CPM at $U = 0.5$ V (left) and $U = 0.2$ V in chapter VII.3.2. Constant potential measurement. ....                                                                                                     | 74 |
| <b>Figure 75.</b> Cyclic voltammogram of pure 5 cycle PDA film used for CPM at $U = 0.1$ V (left) and $U = -0.1$ V in chapter VII.3.2. Constant potential measurement. ....                                                                                                    | 74 |
| <b>Figure 76.</b> Cyclic voltammogram of pure 5 cycle PDA film used for CPM at $U = -0.4$ V (left) and $U = -0.2$ V in chapter VII.3.2. Constant potential measurement. ....                                                                                                   | 74 |
| <b>Figure 77.</b> Cyclic voltammogram of pure 5 cycle PDA film used for CPM at $U = -0.3$ V (left) and $U = -0.5$ V in chapter VII.3.2. Constant potential measurement. ....                                                                                                   | 75 |
| <b>Figure 78.</b> Cyclic voltammogram of pure 5 cycle PDA film used for CPM at $U = OCP = -0.027$ V (left) and OCP determination measurement (right) in chapter VII.3.2. Constant potential measurement. ...                                                                   | 75 |
| <b>Figure 79.</b> Cyclic voltammogram of pure 5 cycle PDA film used for CPM at $U = -0.5$ V for no (left) and methanol (right) as additional hole scavenger in chapter VII.3.2. Constant potential measurement. ...                                                            | 75 |
| <b>Figure 80.</b> Cyclic voltammogram of pure 5 cycle PDA film used for CPM at $U = -0.5$ V for sodium ascorbate (left) and ascorbic acid (right) as additional hole scavenger in chapter VII.3.2. Constant potential measurement. ....                                        | 76 |
| <b>Figure 81.</b> Cyclic voltammogram of pure 5 cycle PDA film used for CPM at $U = -0.5$ V for sodium sulfite as additional hole scavenger in chapter VII.3.2. Constant potential measurement. ....                                                                           | 76 |
| <b>Figure 82.</b> Cyclic voltammogram of 5 cycle PDA film on 0.8 mg/mL spin coated CdSe@CdS solution used for CPM at $U = -0.5$ V (left) and $U = -0.1$ V (right) in chapter VII.3.2. Constant potential measurement. ....                                                     | 76 |
| <b>Figure 83.</b> Cyclic voltammogram of 5 cycle PDA film on 0.8 mg/mL spin coated CdSe@CdS solution used for CPM at $U = -0.2$ V (left) and $U = -0.3$ V (right) in chapter VII.3.2. Constant potential measurement. ....                                                     | 77 |
| <b>Figure 84.</b> Cyclic voltammogram of 5 cycle PDA film on 0.8 mg/mL spin coated CdSe@CdS solution used for CPM at $U = -0.4$ V and with no additional hole scavenger (right). VII.3.2. Constant potential measurement. ....                                                 | 77 |
| <b>Figure 85.</b> Cyclic voltammogram of 5 cycle PDA film on 0.8 mg/mL spin coated CdSe@CdS solution used for CPM at $U = -0.5$ V for sodium ascorbate (left) and sodium sulfite (right) as additional hole scavenger in chapter VII.3.2. Constant potential measurement. .... | 77 |
| <b>Figure 86.</b> Cyclic voltammogram of 5 cycle PDA film on 0.8 mg/mL spin coated CdSe@CdS solution used for CPM at $U = -0.5$ V for methanol (left) and ascorbic acid (right) as additional hole scavenger in chapter VII.3.2. Constant potential measurement. ....          | 78 |
| <b>Figure 87.</b> 20 times SPM of pure CdSe@CdS film (1.2 mg/mL spin coated solution) (top) and exponential decay fit of collected initial mean photocurrents (bottom) in chapter VII.3.1. Sweeping potential measurement. ....                                                | 78 |
| <b>Figure 88.</b> 30 times SPM of pure 5 cycle PDA film (top) and exponential decay fit of collected initial mean photocurrents (bottom) in chapter VII.3.1. Sweeping potential measurement. ....                                                                              | 79 |
| <b>Figure 89.</b> 30 times SPM of pure 45 cycle PDA film (top) and exponential decay fit of collected initial mean photocurrents (bottom) in chapter VII.3.1. Sweeping potential measurement. ....                                                                             | 79 |
| <b>Figure 90.</b> 30 times SPM of a 5 cycle PDA on 0.05 mg/mL spin coated CdSe@CdS nanorod solution (top) and exponential decay fit of initial mean photocurrents (bottom) in chapter VII.3.1. Sweeping potential measurement. ....                                            | 80 |

|                                                                                                                                                                                                                                      |    |
|--------------------------------------------------------------------------------------------------------------------------------------------------------------------------------------------------------------------------------------|----|
| <b>Figure 91.</b> 30 times SPM of a 5 cycle PDA on 0.1 mg/mL spin coated CdSe@CdS nanorod solution (top) and exponential decay fit of initial mean photocurrents (bottom) in chapter VII.3.1. Sweeping potential measurement. ....   | 80 |
| <b>Figure 92.</b> 30 times SPM of a 5 cycle PDA on 0.2 mg/mL spin coated CdSe@CdS nanorod solution (top) and exponential decay fit of initial mean photocurrents (bottom) in chapter VII.3.1. Sweeping potential measurement. ....   | 81 |
| <b>Figure 93.</b> 30 times SPM of a 5 cycle PDA on 0.3 mg/mL spin coated CdSe@CdS nanorod solution (top) and exponential decay fit of initial mean photocurrents (bottom) in chapter VII.3.1. Sweeping potential measurement. ....   | 81 |
| <b>Figure 94.</b> 30 times SPM of a 5 cycle PDA on 0.4 mg/mL spin coated CdSe@CdS nanorod solution (top) and exponential decay fit of initial mean photocurrents (bottom) in chapter VII.3.1. Sweeping potential measurement. ....   | 82 |
| <b>Figure 95.</b> 30 times SPM of a 5 cycle PDA on 0.8 mg/mL spin coated CdSe@CdS nanorod solution (top) and exponential decay fit of initial mean photocurrents (bottom) in chapter VII.3.1. Sweeping potential measurement. ....   | 82 |
| <b>Figure 96.</b> 30 times SPM of a 5 cycle PDA on 1.6 mg/mL spin coated CdSe@CdS nanorod solution (top) and exponential decay fit of initial mean photocurrents (bottom) in chapter VII.3.1. Sweeping potential measurement. ....   | 83 |
| <b>Figure 97.</b> 30 times SPM of a 5 cycle PDA on 2.0 mg/mL spin coated CdSe@CdS nanorod solution (top) and exponential decay fit of initial mean photocurrents (bottom) in chapter VII.3.1. Sweeping potential measurement. ....   | 83 |
| <b>Figure 98.</b> 30 times SPM of pure 1.2 mg/mL spin coated CdSe@CdS nanorod solution (top) and exponential decay fit of initial mean photocurrents (bottom) in chapter VII.3.1. Sweeping potential measurement. ....               | 84 |
| <b>Figure 99.</b> 30 times SPM of a pure 5 cycle PDA (top) and exponential decay fit of initial mean photocurrents (bottom) in chapter VII.3.1. Sweeping potential measurement. ....                                                 | 84 |
| <b>Figure 100.</b> 30 times SPM of a 5 cycle PDA on 1.2 mg/mL spin coated CdSe@CdS nanorod solution (top) and exponential decay fit of initial mean photocurrents (bottom) in chapter VII.3.1. Sweeping potential measurement. ....  | 85 |
| <b>Figure 101.</b> 30 times SPM of a 30 cycle PDA on 1.2 mg/mL spin coated CdSe@CdS nanorod solution (top) and exponential decay fit of initial mean photocurrents (bottom) in chapter VII.3.1. Sweeping potential measurement. .... | 85 |
| <b>Figure 102.</b> 30 times SPM of a 15 cycle PDA on 1.2 mg/mL spin coated CdSe@CdS nanorod solution (top) and exponential decay fit of initial mean photocurrents (bottom) in chapter VII.3.1. Sweeping potential measurement. .... | 86 |
| <b>Figure 103.</b> 30 times SPM of a pure ITO (top) and exponential decay fit of initial mean photocurrents (bottom) in chapter VII.3.1. Sweeping potential measurement. ....                                                        | 86 |
| <b>Figure 104.</b> CPM of pure ITO at $U = -0.5$ V in chapter VII.3.2. Constant potential measurement. ....                                                                                                                          | 87 |

## XII. Table of Tables

|                                                                                                                                                                                                                                                                                                              |    |
|--------------------------------------------------------------------------------------------------------------------------------------------------------------------------------------------------------------------------------------------------------------------------------------------------------------|----|
| <b>Table 1.</b> Overpotentials $U_o$ for oxygen and hydrogen evolution at different electrode materials. <sup>[69]</sup> ...                                                                                                                                                                                 | 21 |
| <b>Table 2.</b> Oxidation and reduction peaks of catechol, methylcatechol and dopamine for acidic (pH 0.65), neutral (pH 7.2) and basic (pH 10.8) pH solutions (potential sweep: - 1 V to 1.5 V, scan rate: 0.05 V/s, RE: Ag/AgCl with 0.197 V vs. SHE, CE: Pt wire, WE: tetrahedral amorphous carbon). .... | 28 |
| <b>Table 3.</b> Summary of the initial lamp-on, initial lamp-off and ratio of lamp-on/off currents of the hole scavenger. ....                                                                                                                                                                               | 52 |
| <b>Table 4.</b> List of all used SAM agents with the contact angle and roughness of the surface. ....                                                                                                                                                                                                        | 60 |
| <b>Table 5.</b> Composition of hole scavenger solutions in phosphate buffer (PB) (methanol, ascorbic acid, sodium ascorbate and sodium sulfite) used for constant potential photocurrent measurements. ....                                                                                                  | 68 |

### XIII. References

- [1] P. Kalisman, Y. Nakibli, L. Amirav, *Nano Lett.* **2016**, *16*, 1776–1781.
- [2] C. Wang, D. Wang, T. Dai, P. Xu, P. Wu, Y. Zou, P. Yang, J. Hu, Y. Li, Y. Cheng, *Adv. Funct. Mater.* **2018**, *28*, 1802127.
- [3] J. Davis, D. H. Vaughan, M. F. Cardosi, *Electrochim. Acta* **1998**, *43*, 291–300.
- [4] J. H. Kim, M. Lee, C. B. Park, *Angew. Chemie* **2014**, *126*, 6482–6486.
- [5] Y. Jeong, D. G. Jwa, A. You, S. Park, J. G. Kim, S. M. Kang, M. Kim, *Asian J. Org. Chem.* **2019**, *8*, 1610–1612.
- [6] J. H. Ryu, P. B. Messersmith, H. Lee, *ACS Appl. Mater. Interfaces* **2018**, *10*, 7523–7540.
- [7] R. M. Navarro Yerga, M. C. Álvarez Galván, F. Del Valle, J. A. Villoria de la Mano, J. L. G. Fierro, *ChemSusChem Chem. Sustain. Energy Mater.* **2009**, *2*, 471–485.
- [8] L. Amirav, A. P. Alivisatos, *J. Phys. Chem. Lett.* **2010**, *1*, 1051–1054.
- [9] L. Xu, X. Huang, J. Zhu, H. Chen, K. Chen, *J. Mater. Sci.* **2000**, *35*, 1375–1378.
- [10] R. Y. Kannah, S. Kavitha, O. P. Karthikeyan, G. Kumar, N. V. Dai-Viet, J. R. Banu, *Bioresour. Technol.* **2020**, 124175.
- [11] X. Li, L. Zhao, J. Yu, X. Liu, X. Zhang, H. Liu, W. Zhou, *Nano-Micro Lett.* **2020**, *12*, 1–29.
- [12] A. Fujishima, K. Honda, *Nature* **1972**, *238*, 37–38.
- [13] C. Haeßner, K. Köhler, K. Wussow, *Chemie unserer Zeit* **2014**, *48*, 246–259.
- [14] U. Eberle, B. Müller, R. Von Helmolt, *Energy Environ. Sci.* **2012**, *5*, 8780–8798.
- [15] H.-X. Jing, L.-X. Li, J. Huang, N. Li, W.-J. Pei, X.-F. Yang, *Funct. Mater. Lett.* **2020**, *13*, 2051027.
- [16] H. B. Gray, *Nat. Chem.* **2009**, *1*, 7.
- [17] M. Z. Iqbal, S. R. Ali, S. Khan, *Sol. Energy* **2019**, *181*, 490–509.
- [18] S. Mastroianni, I. Asghar, K. Miettunen, J. Halme, A. Lanuti, T. M. Brown, P. Lund, *Phys. Chem. Chem. Phys.* **2014**, *16*, 6092–6100.
- [19] L. Wobbe, R. Bassi, O. Kruse, *Trends Plant Sci.* **2016**, *21*, 55–68.
- [20] Y. Chen, X. Feng, Y. Liu, X. Guan, C. Burda, L. Guo, *ACS Energy Lett.* **2020**, *5*, 844–866.
- [21] J. H. Kim, Y. Jo, J. H. Kim, J. W. Jang, H. J. Kang, Y. H. Lee, D. S. Kim, Y. Jun, J. S. Lee, *ACS Nano* **2015**, *9*, 11820–11829.
- [22] I. R. Hamdani, A. N. Bhaskarwar, *Renew. Sustain. Energy Rev.* **2020**, 110503.
- [23] D. Sabba, M. H. Kumar, L. H. Wong, J. Barber, M. Grätzel, N. Mathews, *Nano Lett.* **2015**, *15*, 3833–3839.
- [24] Z. Jin, Z. Hu, C. Y. Jimmy, J. Wang, *J. Mater. Chem. A* **2016**, *4*, 13736–13741.
- [25] L. Pan, J. H. Kim, M. T. Mayer, M.-K. Son, A. Ummadisingu, J. S. Lee, A. Hagfeldt, J. Luo, M. Grätzel, *Nat. Catal.* **2018**, *1*, 412–420.
- [26] L. Qiu, L. K. Ono, Y. Qi, *Mater. today energy* **2018**, *7*, 169–189.
- [27] V. L. Bridewell, R. Alam, C. J. Karwacki, P. V. Kamat, *Chem. Mater.* **2015**, *27*, 5064–5071.
- [28] A. S. Weingarten, R. V. Kazantsev, L. C. Palmer, M. McClendon, A. R. Koltonow, A. P. S. Samuel, D. J. Kiebal, M. R. Wasielewski, S. I. Stupp, *Nat. Chem.* **2014**, *6*, 964–970.
- [29] H. Sai, A. Erbas, A. Dannenhoffer, D. Huang, A. Weingarten, E. Siismets, K. Jang, K. Qu, L. C. Palmer, M. O. De La Cruz, *J. Mater. Chem. A* **2020**, *8*, 158–168.
- [30] B. P. Lee, P. B. Messersmith, J. N. Israelachvili, J. H. Waite, *Annu. Rev. Mater. Res.* **2011**, *41*, 99–132.



- [31] D. Merki, S. Fierro, H. Vrubel, X. Hu, *Chem. Sci.* **2011**, *2*, 1262–1267.
- [32] J. B. Allen, R. F. Larry, in *Electrochem. Methods Fundam. Appl.*, Wiley New York, **2001**, p. 736ff.
- [33] R. J. D. Tilley, R. J. D. Tilley, in *Underst. Solids Sci. Mater.*, Wiley Online Library, **2013**, p. 396ff.
- [34] I. D. Raistrick, J. McHardy, F. Ludwig, in *Electrochem. Semicond. Electron. Process. Devices*, **1992**, p. 16f.
- [35] A. I. Onyia, H. I. Ikeri, A. N. Nwobodo, *J. Ovonic Res.* **2018**, *14*, 49–54.
- [36] T. Kippeny, L. A. Swafford, S. J. Rosenthal, *J. Chem. Educ.* **2002**, *79*, 1094.
- [37] G. Hodes, A. Albu-Yaron, F. Decker, P. Motisuke, *Phys. Rev. B* **1987**, *36*, 4215.
- [38] M. G. Lupo, F. Della Sala, L. Carbone, M. Zavelani-Rossi, A. Fiore, L. Lüer, D. Polli, R. Cingolani, L. Manna, G. Lanzani, *Nano Lett.* **2008**, *8*, 4582–4587.
- [39] E. A. Dias, S. L. Sewall, P. Kambhampati, *J. Phys. Chem. C* **2007**, *111*, 708–713.
- [40] Z. Pan, H. Zhang, K. Cheng, Y. Hou, J. Hua, X. Zhong, *ACS Nano* **2012**, *6*, 3982–3991.
- [41] D. V Talapin, E. V Shevchenko, C. B. Murray, A. Kornowski, S. Foerster, H. Weller, *J. Am. Chem. Soc.* **2004**, *126*, 12984–12988.
- [42] Y. Tian, T. Newton, N. A. Kotov, D. M. Guldi, J. H. Fendler, *J. Phys. Chem.* **1996**, *100*, 8927–8939.
- [43] H. Eshet, M. Grünwald, E. Rabani, *Nano Lett.* **2013**, *13*, 5880–5885.
- [44] K. Wu, Z. Chen, H. Lv, H. Zhu, C. L. Hill, T. Lian, *J. Am. Chem. Soc.* **2014**, *136*, 7708–7716.
- [45] P. Wang, T. Wu, C. Wang, J. Hou, J. Qian, Y. Ao, *ACS Sustain. Chem. Eng.* **2017**, *5*, 7670–7677.
- [46] H. Yamamoto, Y. Sakai, K. Ohkawa, *Biomacromolecules* **2000**, *1*, 543–551.
- [47] J. H. Waite, M. L. Tanzer, *Science (80- )*. **1981**, *212*, 1038–1040.
- [48] H. Lee, S. M. Dellatore, W. M. Miller, P. B. Messersmith, *Science (80- )*. **2007**, *318*, 426–430.
- [49] H. G. Silverman, F. F. Roberto, *Mar. Biotechnol.* **2007**, *9*, 661–681.
- [50] Y. Liu, K. Ai, L. Lu, *Chem. Rev.* **2014**, *114*, 5057–5115.
- [51] G. D. Storrer, K. Takada, H. D. Abruña, *Inorg. Chem.* **1999**, *38*, 559–565.
- [52] C. Ruan, W. Shi, H. Jiang, Y. Sun, X. Liu, X. Zhang, Z. Sun, L. Dai, D. Ge, *Sensors Actuators B Chem.* **2013**, *177*, 826–832.
- [53] J. D. Simon, D. N. Peles, *Acc. Chem. Res.* **2010**, *43*, 1452–1460.
- [54] J. Wang, B. Li, Z. Li, K. Ren, L. Jin, S. Zhang, H. Chang, Y. Sun, J. Ji, *Biomaterials* **2014**, *35*, 7679–7689.
- [55] Y. Li, M. Liu, C. Xiang, Q. Xie, S. Yao, *Thin Solid Films* **2006**, *497*, 270–278.
- [56] D. R. Dreyer, D. J. Miller, B. D. Freeman, D. R. Paul, C. W. Bielawski, *Chem. Sci.* **2013**, *4*, 3796–3802.
- [57] S. Hong, Y. S. Na, S. Choi, I. T. Song, W. Y. Kim, H. Lee, *Adv. Funct. Mater.* **2012**, *22*, 4711–4717.
- [58] B. Stöckle, D. Y. W. Ng, C. Meier, T. Paust, F. Bischoff, T. Diemant, R. J. Behm, K. E. Gottschalk, U. Ziener, T. Weil, *Macromol. Symp.* **2014**, *346*, 73–81.
- [59] J. L. Szelwicka, Herstellung Und Charakterisierung von Polydopamin-Hybrid-Filmen Für Photokatalyse, Johannes-Gutenberg University Mainz: Max-Planck-Institute for Polymer Research, **2018**.
- [60] R. D. Little, K. D. Moeller, **2018**.

- [61] S. J. Hendel, E. R. Young, *J. Chem. Educ.* **2016**, 93, 1951–1956.
- [62] J. S. Jayson, *Am. J. Phys.* **2014**, 82, 60–65.
- [63] G. F. Martins, *J. Chem. Educ.* **1990**, 67, 482.
- [64] N. Elgrishi, K. J. Rountree, B. D. McCarthy, E. S. Rountree, T. T. Eisenhart, J. L. Dempsey, *J. Chem. Educ.* **2018**, 95, 197–206.
- [65] J. B. Allen, R. F. Larry, in *Electrochem. Methods Fundam. Appl.*, Wiley New York, **2001**, p. 44ff.
- [66] S. Singh Gho, Deborah, “Connection between  $(E_{\text{cell}})$ ,  $\Delta G$ , and  $K$ ,” can be found under [https://chem.libretexts.org/Bookshelves/Analytical\\_Chemistry/Supplemental\\_Modules\\_\(Analytical\\_Chemistry\)/Electrochemistry/Electrochemistry\\_and\\_Thermodynamics](https://chem.libretexts.org/Bookshelves/Analytical_Chemistry/Supplemental_Modules_(Analytical_Chemistry)/Electrochemistry/Electrochemistry_and_Thermodynamics), **2013**. (accessed 11/15/20)
- [67] “2: Electrical Double Layer and Charging Current - Chemistry LibreTexts,” can be found under [https://chem.libretexts.org/Bookshelves/Analytical\\_Chemistry/Supplemental\\_Modules\\_\(Analytical\\_Chemistry\)/Analytical\\_Sciences\\_Digital\\_Library/JASDL/Courseware/Analytical\\_Electrochemistry%3A\\_The\\_Basic\\_Concepts/03\\_Fundamentals\\_of\\_Electrochemistry/A.\\_Electrochem](https://chem.libretexts.org/Bookshelves/Analytical_Chemistry/Supplemental_Modules_(Analytical_Chemistry)/Analytical_Sciences_Digital_Library/JASDL/Courseware/Analytical_Electrochemistry%3A_The_Basic_Concepts/03_Fundamentals_of_Electrochemistry/A._Electrochem), **2020**. (accessed 11/15/20)
- [68] M. M. Walczak, D. A. Dryer, D. D. Jacobson, M. G. Foss, N. T. Flynn, *J. Chem. Educ. Downloaded via MPI Polym.* **1997**, 74, 31.
- [69] D. M. Heard, A. J. J. Lennox, *Angew. Chemie Int. Ed.* **2020**, 59, 18866–18884.
- [70] F. Marken, A. Neudeck, A. M. Bond, in *Electroanal. Methods*, Springer-Verlag Berlin Heidelberg 2005, **2005**, p. 58ff.
- [71] C. Brett, A. M. Oliveira Brett, in *Electrochem. Princ. Methods, Appl.*, Oxford University Press, Oxford, **1993**, p. 146f.
- [72] P. T. Kissinger, W. R. Heineman, *J. Chem. Educ.* **1983**, 60, 702.
- [73] C. G. Zoski, in *Handb. Electrochem.*, Elsevier, **2006**, p. 22ff.
- [74] G. Mei-Zhen, J. R. X. De-Sheng, F. W. R., *Chinese Phys. Lett.* **2008**, 25, 1380–1383.
- [75] C. G. Zoski, in *Handb. Electrochem.*, Elsevier, **2006**, p. 849f.
- [76] C. Brett, A. M. Oliveira Brett, in *Electrochem. Princ. Methods, Appl.*, Oxford University Press, Oxford, **1993**, p. 32f.
- [77] T. P. DeAngelis, W. R. Heineman, *J. Chem. Educ.* **1976**, 53, 594.
- [78] A. Sevcik, *Commun* **1948**, 13, 349.
- [79] J. E. B. Randles, *Trans. Faraday Soc.* **1948**, 44, 327–338.
- [80] A. Turnbull, J. G. N. Thomas, *J. Electrochem. Soc.* **1982**, 129, 1412.
- [81] J. Divišek, B. Kastening, *J. Electroanal. Chem. Interfacial Electrochem.* **1975**, 65, 603–621.
- [82] J. C. Myland, K. B. Oldham, *Anal. Chem.* **2000**, 72, 3972–3980.
- [83] K. B. Oldham, N. P. C. Stevens, *Anal. Chem.* **2000**, 72, 3981–3988.
- [84] T. Palomäki, S. Chumillas, S. Sainio, V. Protopopova, M. Kauppila, J. Koskinen, V. Climent, J. M. Feliu, T. Laurila, *Diam. Relat. Mater.* **2015**, 59, 30–39.
- [85] Y. Shigesato, D. C. Paine, *Thin Solid Films* **1994**, 238, 44–50.
- [86] S. Song, T. Yang, J. Liu, Y. Xin, Y. Li, S. Han, *Appl. Surf. Sci.* **2011**, 257, 7061–7064.